

Université de Lille

Doctoral School **Sciences de la Matière, du Rayonnement et de l'Environnement**

University Department **Laboratoire de Physique des Lasers, Atomes et Molécules (PhLAM)**

Thesis defended by **Eve-Line Bancel**

Defended on **December 18, 2023**

In order to become Doctor from Université de Lille

Academic Field **Physics**

Speciality **Diluted media and fundamental optics**

Generation of triple frequency combs in multi-core fibres for multidimensional spectroscopy

Thesis supervised by	Arnaud Mussot	Supervisor	
	Rosa Santagata	Co-Supervisor	

Committee members

Referees	François Léo	Associate Professor at Université Libre de Bruxelles	
	Thibaut Sylvestre	Senior Researcher at Université de Franche Comté	
Examiners	Hervé Rigneault	Senior Researcher at Université Aix-Marseille	Committee President
	Anne Durecu	ONERA	
	Benjamin Wetzel	Junior Researcher at Université de Limoges	
Supervisors	Arnaud Mussot	Professor at Université de Lille	
	Rosa Santagata	ONERA	

Université de Lille

École doctorale **Sciences de la Matière, du Rayonnement et de l'Environnement**

Unité de recherche **Laboratoire de Physique des Lasers, Atomes et Molécules (PhLAM)**

Thèse présentée par **Eve-Line Bancel**

Soutenue le **18 décembre 2023**

En vue de l'obtention du grade de docteur de l'Université de Lille

Discipline **Physique**

Spécialité **Milieux dilués et optique fondamentale**

Génération de triple peignes de fréquences dans les fibres multi-coeurs pour la spectroscopie multidimensionnelle

Thèse dirigée par

Arnaud Mussot	directeur
Rosa Santagata	co-directeur

Composition du jury

Rapporteurs	François Léo	mcf à l'Université Libre de Bruxelles	
	Thibaut Sylvestre	directeur de recherche à l'Université de Franche Comté	
Examinateurs	Hervé Rigneault	directeur de recherche à l'Université Aix-Marseille	président du jury
	Anne Durecu	ONERA	
	Benjamin Wetzel	chargé de recherche à l'Université de Limoges	
Directeurs de thèse	Arnaud Mussot	professeur à l'Université de Lille	
	Rosa Santagata	ONERA	

This thesis has been prepared at the following research units.

Laboratoire de Physique des Lasers, Atomes et Molécules (PhLAM)

Campus Cité Scientifique
2 Avenue Jean Perrin
59655 Villeneuve d'Asq Cedex
France

Institut de Recherche en Composants logiciels et matériels pour l'Information et la Communication Avancée (IRCICA)

Parc Scientifique de la Haute Borne
50 avenue Halley
59658 Villeneuve d'Asq Cedex
France

Office national d'études et de recherches aérospatiales (ONERA)

6 Chemin de la Vauve aux Granges
91120 Palaiseau
France

A Simon et à Zlip,
A la recherche en fanfare.

Generation of triple frequency combs in multi-core fibres for multidimensional spectroscopy

Abstract

This thesis work explores the development, characterization, and practical application of a novel, fully fibered, and freely-tunable tri-frequency-comb laser source for advanced multidimensional spectroscopy. Tricomb spectroscopy unveils a new dimension to standard linear and non-linear spectroscopic analysis, offering the possibility to reveal the almost real-time evolution of complex systems with unprecedented accuracy. Current tri-comb configurations are based on the use of mode-locked lasers, which impose constraints on the comb parameters, and require complex electronic synchronization, thus limiting potential applications. In this thesis, we present the experimental demonstration of the spatial multiplexing in a multi-core non-linear fiber of three electro-optic combs from a common laser source. This architecture aims to ensure intrinsic mutual coherence between the three combs. The manuscript provides a comprehensive study of the development and characterization of the three combs. We validated their pairwise coherence through dual-comb experiments. We exploited the tri-comb coherence to experimentally investigate intra-envelope four-wave mixing phenomenon in optical fibers. Using the third comb as a multi-line local oscillator enabled us to extract and analyze the intermingled components resulting from the non-linear interaction between the two first combs. We then revealed the high mutual coherence between the three broadened combs by applying this approach through the demonstration of a 2-D FWM spectroscopy experiment.

Keywords: non-linear fiber optics, multi-core fiber, spatial multiplexing, frequency comb, multi-dimensional coherent spectroscopy, four wave mixing, electro-optic modulation, self phase modulation

Génération de triple peignes de fréquences dans les fibres multi-coeurs pour la spectroscopie multidimensionnelle

Résumé

Ces travaux de thèse explorent le développement, la caractérisation et l'application pratique d'une nouvelle source de tri-peigne de fréquences entièrement fibrée, et accordable, pour la spectroscopie multidimensionnelle. La spectroscopie à trois peignes apporte une nouvelle dimension à l'analyse spectroscopique linéaire et non linéaire classique, offrant la possibilité de mesurer l'évolution presque en temps réel de systèmes complexes avec une précision inégalée. Les configurations actuelles de tri-peignes sont fondées sur l'utilisation de lasers à verrouillage de modes, ce qui impose des contraintes sur les paramètres du système et nécessite une synchronisation électronique complexe, limitant ainsi les applications potentielles. Dans cette thèse, nous présentons la démonstration expérimentale du multiplexage spatial de trois peignes électro-optiques provenant d'une source laser commune, dans une fibre non linéaire à plusieurs cœurs. Ce choix d'architecture vise à assurer une cohérence mutuelle intrinsèque entre les trois peignes. Ce manuscrit fournit une étude du développement et de la caractérisation des trois peignes. Nous avons validé leur cohérence par paire grâce à des expériences à double peigne. Nous avons exploité la cohérence à trois peignes pour étudier expérimentalement le phénomène de mélange à quatre ondes intra-enveloppe dans les fibres optiques. L'utilisation du troisième peigne comme oscillateur local multi-lignes nous a permis d'extraire et d'analyser les composantes entremêlées résultant de l'interaction non linéaire entre les deux premiers peignes. Nous avons ensuite révélé la haute cohérence mutuelle entre les trois peignes élargis en appliquant cette approche à la démonstration d'une expérience de spectroscopie tri-peigne en 2D.

Mots clés : optique non linéaire fibrée, fibre multi-coeur, multiplexage spatial, peigne de fréquences, spectroscopie cohérente multidimensionnelle, mélange à quatre ondes, modulation électro-optique, auto-modulation de phase

Laboratoire de Physique des Lasers, Atomes et Molécules (PhLAM) – Campus Cité Scientifique – 2 Avenue Jean Perrin – 59655 Villeneuve d'Asq Cedex – France
Institut de Recherche en Composants logiciels et matériels pour l'Information et la Communication Avancée (IRCICA) – Parc Scientifique de la Haute Borne – 50 avenue Halley – 59658 Villeneuve d'Asq Cedex – France
Office national d'études et de recherches aérospatiales (ONERA) – 6 Chemin de la Vauve aux Granges – 91120 Palaiseau – France

Remerciements

Cette thèse est une collaboration entre le laboratoire PhLAM de l'Université de Lille et l'ONERA de Palaiseau. Elle a été rendue possible grâce au co-financement de la région Hauts de France et de l'ONERA. A ce titre, je tiens à remercier Marc Douay, ancien directeur, et Cristian Focsa, directeur du laboratoire PhLAM de l'Université de Lille et ancien directeur des études doctorales. Mes remerciements vont également à Riad Haidar, alors directeur scientifique du domaine Physique de l'ONERA.

Je tiens ensuite exprimer ma gratitude aux membres du jury pour avoir évalué mon travail de thèse : tout d'abord les rapporteurs, François Léo et Thibaut Sylvestre, ainsi que les examinateurs et examinatrice, Benjamin Wetzel, Hervé Rigneault et Anne Durecu. J'adresse une pensée particulière à Hervé et Anne, qui ont constitué le comité de suivi de ma thèse.

J'ai bénéficié pendant cette thèse d'un encadrement exceptionnel. Je tiens donc à remercier Rosa Santagata et Arnaud Mussot pour leurs qualités humaines, leur expertise scientifique et le dévouement professionnel dont elle et il ont fait preuve pendant trois ans. Rosa, Arnaud, merci pour votre patience, merci pour votre sens de la pédagogie et merci pour votre soutien sans faille (même, et surtout quand ça ne marchait pas). Vous m'avez encouragée quand il y avait des "points à marquer", et vous vous êtes réjoui.e.s avec moi quand les points étaient enfin marqués. C'est grâce à vous que cette thèse est ce qu'elle est aujourd'hui, donc pour ça, et pour tout le reste, merci.

Les collègues avec qui j'ai travaillé ont également été une source indéfectible de soutien, à la fois scientifique et émotionnel.

Du côté ONERA, il y a les doctorant.e.s des premières heures, Jeanne, Jonas et Elodie, avec bien sûr une affection particulière pour cette dernière, vrai GPS dans la fôret palaisienne. Il y a également toute l'équipe SLM : Myriam, Jean-Michel, Jean-Baptiste, Michael, Clément, Maxime, Jean-Pierre, Philippe, Nelly, Christophe, Bavette, Alexandre, Nassim, Malo, Alexis, et Cédric. Je tiens à adresser ici toute ma gratitude à Michael, JB et Nassim qui ont toujours eu la porte ouverte et l'oreille attentive. Je rajouterai bien sûr la deuxième vague des doctorant.e.s : Antoine, Romain, Noémie et Clément. J'espère que vous savez à quel point j'ai apprécié votre compagnie dans les temps fatidiques de rédaction et de préparation de soutenance.

Mes remerciements vont ensuite à l'ensemble de l'équipe Photonique du PhLAM, qui m'a offert un cadre de travail exceptionnel, tant par les conditions matérielles que pour la qualité des échanges humains. Je tiens notamment à remercier toute l'équipe de FiberTech pour la fibre à trois coeurs sur laquelle repose nos travaux, et en particulier Damien Labat pour nos échanges à ce sujet. J'adresse également mes remerciement à Etienne Genier pour le travail effectué sur le montage avant mon arrivée à Lille, Jean-Loic Fixy pour sa persévérance administrative, Alexandre Kudlinkski, Vincent Andrieux et Aymeric Pastre pour le twist final. Je ne

saurai insister sur le plaisir que j'ai eu pendant un an et demi à travailler dans le bureau 105, avec la merveilleuse équipe que forment Aymeric, Vincent, Laure, et Thomas. Merci pour les explications sur les fibres et merci pour les fous rires. J'adresse ensuite ma gratitude et mon amitié aux compagnons du labo : Guillaume, Stefano, Thomas (encore et toujours là). Les trois peignes auraient drôlement moins bien marché sans vous. Et je tiens bien sûr à remercier les autres camarades du TechnoPhlam que sont Jean, Gaelle, Halima, Dylan et Sarah. Merci pour ces moments partagés, vous méritez tous les petits pains du monde.

Je me permets ici d'exprimer toute la reconnaissance que j'ai en mes ami.e.s qui ont été incroyablement présent.e.s pendant ces trois ans. Je ne vous nomme pas car ce sont des remerciements de thèse et non pas un annuaire, mais sachez que vous avez été un précieux cocon et une fabuleuse source d'énergie. J'aimerai faire mention (honorable) de la fanfare Cristina Ursula Cordula, la maison mère, celle chez qui on se sent bien parce que ça sent toujours les cookies. J'aimerais également adresser un grand et franc merci à la fanfare Tractopelle. Vous m'avez aidé à recréer l'odeur des cookies dans la capitale des Flandres, même si c'était un peu plus senteur frites et maroilles.

Ce manuscrit n'existerait pas sans la présence indéfectible dont a fait preuve ma famille. Papa, maman, merci de m'avoir fortement incitée à choisir la filière scientifique et l'espagnol en LV2. Vous êtes à vous deux le comité de soutien en logistique et en amour le plus efficace de ma planète.

J'aimerai adresser la dernière pensée de ces remerciements à Nicolas Louviaux. Merci pour tout, et bonne chance pour ton doctorat.

Acronyms

2D 2-dimension

2DS 2-Dimensional Spectroscopy

3D 3-dimension

AC Auto-Correlation

AM Amplitude-Modulation

ANDI All-Normal DIspersion

AOM Acousto-Optic Modulation

AOM Acousto-Optic Modulator

ASE Amplified Stimulated Emission

AWG Arbitrary Waveform Generator

BW BandWidth

CW Continuous Wave

DIAL Differential Absorption LIDAR

DCS Dual Comb Spectroscopy

DSF Dispersion Shifted Fiber

EDFA Erbium-Doped Fibered Amplifier

ESA Electronic Spectral Analyser

EM Electro-Magnetic

EO Electro-Optic

EOM Electro-Optic Modulation

EOM Electro-Optic Modulator

FBG Fibered Bragg Grating

FT Fourier Transform

FTIR Fourier-Transformed Infra-Red

FWHM Full-Width-Half-Maximum

FWM Four Wave Mixing

GNLSE Generalized Non-Linear Schrödinger Equation

GVD Group Velocity Dispersion

IEEE Institute of Electrical and Electronics Engineers

IM Intensity Modulator

LASER Light Amplification by Stimulated Emission of Radiation

LIDAR Laser Imaging, Detection, And Ranging

LO Local Oscillator

LPF Low-Pass Filter

MDCS Multi-Dimensional Coherent Spectroscopy

MLL Mode-Locked Laser

MZM Mach-Zehnder Modulators

NALM Non-linear Amplifying Loop Mirror

NLF Non-Linear Fiber

NLSE Non-Linear Schrödinger Equation

NMR Nuclear Magnetic Resonance

NZDSF Non-Zero Dispersion Shifted Fiber

OSA Optical Spectral Analyzer

OSO Optical Sampling Oscilloscope

PC Polarization Controller

PCF Photonic Crystal Fiber

PD Photo-Detector

PM Phase-Modulation

PM Polarisation-Maintaining

PPLN Periodically Poled Lithium Niobate

PSD Power Spectral Density

PSG Power Signal Generator

RF Radio Frequency

SA Saturable Absorber

SHG Second Harmonic Generation

SMF Single-Mode Fiber

SNR Signal-to-Noise Ratio

SPM Self Phase-Modulation

SSB Single SideBand

SVEA Slowly Varying Envelope Approximation

TCS Triple Comb Spectroscopy

TL Transform-Limited

XPM Cross Phase-Modulation

ZDW Zero-Dispersion Wavelength

Summary

Introduction

In 1960, Theodore Maiman invented the technique to produce a directional beam of monochromatic light [1], called Light Amplification by Stimulated Emission of Radiation (LASER). Inspired by the theoretical work of Arthur Schawlow and Charles Townes, he used a ruby crystal as amplifier medium, out of the concept of maser [2] in the optical wave range. As early as 1961, the potentialities of such a discovery were glimpsed, especially with the first experiment in nonlinear optics conducted by Franken [3]. His team managed to observe the light mark of second-harmonic generation in a quartz, using a ruby laser. To obtain such a non-linear answer from a medium, it is essential to have access to a source of high peak power [4]. This is why the first experimental results in this domain have coincided with the demonstration of Q-switching [5], and then mode-locking [6]. These methods generate pulsed laser sources, reaching the picosecond and femtosecond respectively in pulse duration. Like a conductor synchronizing the different instruments in the orchestra, mode-locking put in phase all the frequencies that participate in the pulse, in order to make them interfere constructively. The spectrum of such a source consists of discrete and evenly spaced frequency peaks [7]. It is one of the results Hargrove's experiment has demonstrated, and it was the first time that a light source with such a spectral structure, called frequency comb, was observed [8].

Historically, the first application of combs was frequency metrology [9]. Electronic instrumentation is too slow for high frequency optical oscillations (in the THz range). The determination of these frequencies with conventional devices requires measurement techniques based on long-term conversion chains, complex both theoretically and experimentally [10]. Using a frequency comb overcomes this difficulty. Their great spectral stability allows them to be used for reference. As a ruler works, any optical frequency can be measured from its difference with the teeth of a comb [11]. This is a relatively easy experiment to implement, which achieves good levels of precision [12]. Frequency comb have become an indispensable tool of measurement in physics, as proved by their use in fields as varied as astrophysics [13, 14] or microscopy [15]. Spectroscopy is a striking example of frequency combs applications, with half of the 2005 Nobel Prize won by J. L. Hall [16] and T. W. Hänsch [17]. They demonstrated the technique of dual comb spectroscopy (DCS). Designed in 2002 by Schiller [18], it achieves a spectral resolution that is no longer instrument-limited, but only set by the difference of repetition frequency of the two combs [19, 20] (traditionally in the Hz or kHz range). In recent years, DCS still keps its promise of high

precision combined with an increase in analysis speed of several orders of magnitude [7, 20].

The sensitivity and precision of DCS depends on the mutual coherence between the comb sources i.e. their weak relaive timing jitter [20, 21], to get high SNR and narrow linewidth spectral lines from the beating. Thus, several technological systems have been developed to generate frequency combs that are coherent with one another, such as phase-locking of two mode-separated lasers [20], bidirectional lasers [22, 23], dual microresonators on a chip [24], or arrays of electro-optic modulators (EOM) driven by a common laser [25]. In nonlinear fiber systems, both propagation directions have been exploited to make the frequency comb experience almost the same phase noise degradation without interacting together [26, 27]. By exploiting these different options, DCS has enabled a great leap forward in the science of linear and nonlinear spectroscopy, microscopy, ranging, and LIDAR [7, 20].

Despite these remarkable features, dual-comb spectrometers have limitations. DCS is a linear technique, with only one scanning parameter (being the difference of repetition rates of the two combs). Therefore, it fails to capture both the evolution both in time and frequency of a sample. On the other hand, multidimensional coherent spectroscopy [28–31] gives access to the monitoring of these evolutions, and enables to study of the coupling between the potential state transitions during chemical reactions in a complex mixture for instance. To achieve this, a third comb is added to the system [28, 31, 32] to access an extra dimension. The first two combs act as the pump and probe to stimulate the nonlinear response of the sample, and the third acts as a multi-line local oscillator, similarly to in DCS. Therefore, it is necessary to develop three-comb light sources with high mutual coherence for highly sensitive and fast multidimensional spectroscopy. Note that three-comb technology is not limited to nonlinear spectroscopy but also enables removing the ambiguity surrounding dual-comb measurements [33]. To obtain three highly coherent combs, one can phase-lock three mode-locked lasers [28, 29] or generate different propagation modes in microresonators [34]. These cavity-based techniques have their own advantages, but the frequency characteristics of the combs are tunable only over a small range, as they are severally dictated by the opto-geometric parameters of the cavity. The consequence is that repetition rates cannot be adapted to the decay rates of the samples to analyze, nor their relative repetition rates to conveniently sample the response of the medium, thus lowering the overall performances.

The work of this thesis consists in the development, the characterization and the proof-of-concept of the use of a fully fibered, freely-tunable, coherent tri-frequency-comb source. Inspired by the architecture proposed by Millot and al [26], a tri-core nonlinear fiber is used to spectrally broaden three electro-optic combs from a single continuous-wave laser. The goal is to keep the benefits of the high non-linearity of fiber optics to obtain wider spectra, while subjecting the three combs to the most similar phase degradation as possible through almost identical pathways. This is proven by a study of the combs stability. Coherence between each pair of the three-comb system is validated by DCS experiments. A demonstration of 2-D Four Wave Mixing (FWM) spectroscopy [28] allows to conclude on the high mutual coherence between

the three combs, proving the system to be efficient for nonlinear experiments.
My thesis is a collaboration between the Sources Lasers and Metrology team (SLM) of Onera's Departement of Physics, Instrumentation and Environnement (DPHY) and the Photonics team of the PHysique des Lasers, Atomes et Molécules laboratory (PhLAM - UMR8523). It was therefore organized between the two sites. At ONERA, a set-up using two commercial combs (C-comb at 1550nm, Menlosystems) enabled me to get to grips with the concept of dual-frequency comb spectroscopy. I stayed in Palaiseau from October 2020 to September 2021, when I moved to Lille. There, I took over and developed the three-comb set-up. This set-up and its utilization are the main subjects in this manuscript. Measurements taken with Menlosystems lasers are used to support the discussion, and the commercial system serves as a point of comparison.
The manuscript is organized in four chapters, as follows. Chapter 1 introduces the concept of multi-comb interferometry. Chapter 2 presents the multi-comb system and the individual characteristics of each comb. Chapter 3 demonstrates the use of the system for DCS. Chapter 4 is a study of FWM based on the interaction between the three combs.

Chapter 1

General information on frequency combs and non-linear effects in fibers

Outline of the current chapter

In this chapter, the notion of *frequency comb* is detailed. The benefits of using a frequency comb, and its applications, are explained. The different architectures available for generating a frequency comb are reviewed, with a particular attention to electro-optical modulation, since it is the technique used for the set-up developed in this thesis. In order to provide the means to apprehend the phenomena at stake, non-linear effects in optical fibers are mathematically described. The third section is about *dual-comb interferometry*, to finally extend the discussion to *tri-comb interferometry*.

1.1 Generalities on frequency combs

1.1.1 Mathematical definition

Temporally, a frequency comb is a train of pulses, of the same envelope A, and regularly emitted at the repetition period $T_{\text{rep}} = \frac{1}{f_{\text{rep}}} = \frac{2\pi}{\omega_{\text{rep}}}$ and at the optical carrier frequency $\nu_p = \frac{\omega_p}{2\pi}$, where ω_{rep} and ω_p are respectively the angular frequencies associated with frequencies f_{rep} and ν_p. The stability of this train comes from the exact repeatability of the pulses: the generation of a frequency comb requires that the periodicity applies not only to the pulses envelope, but also to their optical phase. That defines the concept of *temporal coherence* between the pulses. However, it is possible for the envelope and carrier to temporally shift, inducing at each repetition a constant phase shift $\Delta\phi$ between the two. This shift can be explained by the residual dispersion in the medium generating the pulses, which induces a difference between the phase velocity and the group velocity. In this context, the pulse train $C(t)$ (see Figure 1.1) can be written in the time domain as:

$$C(t) = \sum_{n=-\infty}^{\infty} (A(t)\cos(\omega_p t - n\Delta\phi)) * \delta(t + nT_{\text{rep}}) \tag{1.1}$$

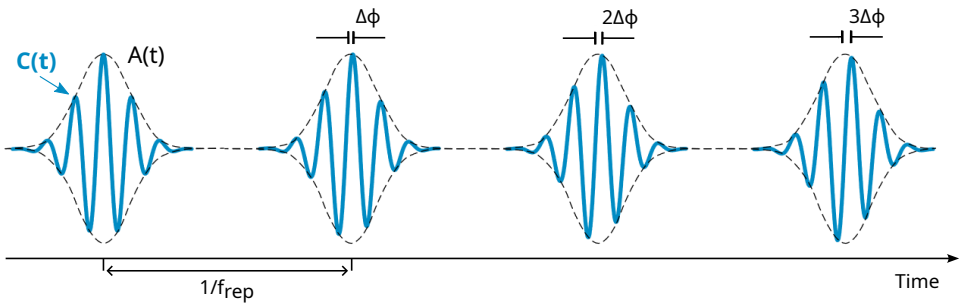

Figure 1.1: Time-domain representation of the train of pulses. Inspired by [7].

Using the Fourier transform (FT), the pulse train in the frequency domain $\tilde{C}$ can be written as :

$$\begin{aligned}\tilde{C}(\omega) = \mathcal{F}_\omega(C(t)) &= \int_{-\infty}^{\infty} C(t)e^{-i\omega t}dt \\ &= \int_{-\infty}^{\infty}\left(\sum_{n=-\infty}^{\infty}(A(t)\cos(\omega_p t - n\Delta\phi)) * \delta(t+nT_{\text{rep}})\right)e^{-i\omega t}dt \\ &= \sum_{n=-\infty}^{\infty}\left(F_\omega(A(t)\cos(\omega_p t - n\Delta\phi))\cdot F_\omega(\delta(t+nT_{\text{rep}}))\right) \\ &= \pi\sum_{n=-\infty}^{\infty}\left(\tilde{A}(\omega) * \left(e^{-in\Delta\phi}\delta(\omega-\omega_p) + e^{in\Delta\phi}\delta(\omega+\omega_p)\right)\right)e^{i\omega nT_{\text{rep}}}\end{aligned} \tag{1.2}$$

where $\tilde{A}(\omega) = F_\omega(A(t))$ is the TF of the temporal envelope.
Expanding the expression to separate positive and negative frequencies, one can find:

$$\begin{aligned}\tilde{C}(\omega) &= \pi\sum_{n=-\infty}^{\infty}\tilde{A}(\omega-\omega_p)e^{in(\omega T_{\text{rep}}-\Delta\phi)} + \pi\sum_{n=-\infty}^{\infty}\tilde{A}(\omega+\omega_p)e^{in(\omega T_{\text{rep}}+\Delta\phi)} \\ &= \pi\tilde{A}(\omega-\omega_p)\sum_{n=-\infty}^{\infty}e^{in\left(\frac{2\pi}{\omega_{\text{rep}}}\right)(\omega-\omega_0)} + \pi\tilde{A}(\omega+\omega_p)\sum_{n=-\infty}^{\infty}e^{in\left(\frac{2\pi}{\omega_{\text{rep}}}\right)(\omega+\omega_0)}\end{aligned} \tag{1.3}$$

by writing $\omega_0 = \frac{\omega_{\text{rep}}}{2\pi\Delta\phi}$. This quantity is called "the offset frequency", whose meaning is explained later in this paragraph.

The latter expression is a discrete sum, centered at $+\omega_p$ for negative frequencies and at $-\omega_p$ for positive frequencies, of exponentials spaced by the quantity ω_{rep}. Mathematically, this corresponds to the Fourier serie expansion of a Dirac comb distribution at the period ω_{rep}, represented by the "sha" function $\text{Ш}_{\omega_{\text{rep}}}$:

$$\text{Ш}_{\omega_{\text{rep}}}(\Omega) = \sum_{n=-\infty}^{\infty}\delta(\Omega - n\omega_{\text{rep}}) \tag{1.4}$$

whose Fourier serie expansion can be computed as:

$$\text{Ш}_{\omega_{\text{rep}}}(\Omega) = \sum_{n=-\infty}^{\infty}c_n(\text{Ш}_{\omega_{\text{rep}}})e^{2i\pi n\frac{\Omega}{\omega}} \tag{1.5}$$

The Fourier coeffients $c_n(\text{Ш}_{\omega_{\text{rep}}})$ of this serie expansion are:

$$\begin{aligned} c_n(\text{Ш}_{\omega_{\text{rep}}}) &= \frac{1}{\omega_{\text{rep}}} \int_{\omega_{\text{rep}}/2}^{-\omega_{\text{rep}}/2} \text{Ш}_{\omega_{\text{rep}}}(\Omega) e^{-2i\pi n \frac{\Omega}{\omega_{\text{rep}}}} d\Omega \\ &= \frac{1}{\omega_{\text{rep}}} \int_{\omega_{\text{rep}}/2}^{-\omega_{\text{rep}}/2} \delta(\Omega) e^{-2i\pi n \frac{\Omega}{\omega_{\text{rep}}}} d\Omega \\ &= \frac{1}{\omega_{\text{rep}}} e^{-2i\pi n} \\ &= \frac{1}{\omega_{\text{rep}}} \end{aligned} \tag{1.6}$$

This means that the Dirac comb at the period ω_{rep} can be written as:

$$\text{Ш}_{\omega_{\text{rep}}}(\Omega) = \sum_{n=-\infty}^{\infty} \delta(\Omega - n\omega_{\text{rep}}) = \frac{1}{\omega_{\text{rep}}} \sum_{n=-\infty}^{\infty} e^{2i\pi n \frac{\Omega}{\omega_{\text{rep}}}} \tag{1.7}$$

We recognize this expression in Eq. 1.3:

$$\sum_{n=-\infty}^{\infty} e^{in2\pi \frac{(\omega+\omega_0)}{\omega_{\text{rep}}}} = \omega_{\text{rep}} \text{Ш}_{\omega_{\text{rep}}}(\omega + \omega_0) \text{ and } \sum_{n=-\infty}^{\infty} e^{in2\pi \frac{(\omega-\omega_0)}{\omega_{\text{rep}}}} = \omega_{\text{rep}} \text{Ш}_{\omega_{\text{rep}}}(\omega - \omega_0) \tag{1.8}$$

Thus, Eq. 1.1 can be written [25]:

$$\tilde{C}(\omega) = \pi\omega_{\text{rep}} \tilde{A}(\omega - \omega_p) \text{Ш}_{\omega_{\text{rep}}}(\omega - \omega_0) + \pi\omega_{\text{rep}} \tilde{A}(\omega + \omega_p) \text{Ш}_{\omega_{\text{rep}}}(\omega + \omega_0) \tag{1.9}$$

The spectrum of a regularly spaced train of temporal impulses is therefore composed of two Dirac combs with the same envelop $\tilde{A}$, one in the negative frequencies and one in the positive frequencies, respectively centered at -ω_p and +ω_p. The positive part, grasping the real physical meaning, is shown in Figure 1.2. The peculiarity of this spectrum is that it is not null only at some regularly spaced frequencies f_n such as, for $n \in \mathbb{N}$:

$$f_n = f_0 + nf_{\text{rep}}, \quad f_n > 0 \tag{1.10}$$

This explains the naming of *frequency combs*, as for the mathematical structure and the particular spectrum composed of equidistant spectral lines that are called *the teeth of the comb*. The position of these lines is entirely defined by two quantities: the repetition frequency $f_{\text{rep}} = \frac{\omega_{\text{rep}}}{2\pi} = \frac{1}{T_{\text{rep}}}$, which represents the spacing between the teeth, and the offset frequency $f_0 = \frac{\omega_0}{2\pi} = \frac{f_{\text{rep}}}{2\pi\Delta\phi}$, which represents the abscissa of the first tooth. Depending on the research team, it is customary to refer to the comb by its offset frequency f_0 or by its carrier frequency f_p. This is simply a matter of usage, and a neophyte should not lose sight of the fact that a frequency comb has only two degrees of freedom. Knowing and controlling these two quantities means knowing and controlling all the spectral lines of the comb. Those parameters are traditionally in

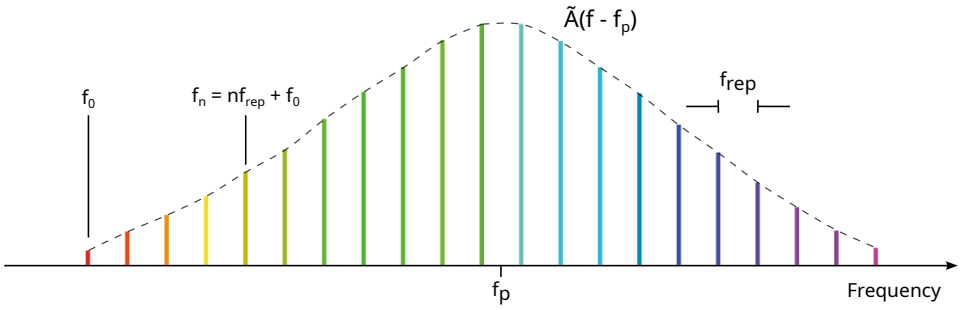

Figure 1.2: Frequency-domain representation of the train of pulses. Inspired by [7].

the radio-frequency (RF) domain. That explains the adage that frequency combs are the link between the optical and radio-frequency domains, since the control of the RF parameters gives access to an optical precision at a THz carrier frequency (and vice versa). That leads to many applications.

1.1.2 Applications

The carrier of an optical wave (300 GHz - 400 THz for the infra-red, 400 THz - 700 THz for visible light) is too fast to be detected by precision frequency counters, whose bandwidth limit is 10 GHz. However, any optical frequency difference can be easily measured as long as they fall under this limit. Let's take the example of two optical carrier frequencies ν_1 and ν_2. Their interference created a signal at a $\nu_1 + \nu_2$ carrier, with an amplitude modulated at the frequency $\Delta f = \nu_1 - \nu_2$. This modulation can be detected by a photo-diode, which produces a proportional voltage. This technique is known as *heterodyne detection*. It is a very common tool to detect the carrier of an optical wave, from a known reference called local oscillator (LO). In such way, frequency combs can be described as rulers for light. By providing a segmentation of the optical domain into spectral lines separated by a radio-frequency quantity, frequency combs (if stable enough) can be used as LOs to measure any optical frequency. The technique of measuring the difference frequency is crucial in most measurement methods involving combs.

Indeed, it is possible to measure any optical frequency from its inference with the comb. This interference produces a multitudes of spectral lines. The lowest frequency f_{beat} of theses lines results from the beat between the unknown frequency ν_i and the comb line that is the closest in frequency ν_n. One can find ν_n by a simple wavelength measurement, or by slightly shifting the central wavelength of the comb or the frequency to be determined. Indeed, f_{beat} is necessarily smaller than $f_{\text{rep}}/2$, and f_{rep} is in the RF range. One can conclude that f_{beat} is also in the RF domain, and therefore be detected on a photo-diode. The unknown frequency ν_i is then indirectly measured: $\nu_i = nf_{\text{rep}} + f_0 + f_{beat}$.

Because they provide very precise measurements, frequency combs have become an indispensable tool in fundamental and applied research. The following is a non-exhaustive list of

fields in which the use of frequency combs has led to major advances. Readers may refer to the bibliographic references [35, 36] for more information.

Optical clocks [37] interrogate a very narrow atomic transition using a laser of extremely high stability and spectral purity. The stability of these optical standards (of the order of a few 10^{-15} at 1 second) far exceeds that of microwave standards based on caesium or rubidium. However, measuring or comparing optical frequencies with other standards is a challenge, since no electronic system is fast enough to process them. Before the development of frequency combs, optical frequency measurements were carried out using complex frequency multiplication chains [10] requiring many lasers and were difficult to implement. Referenced frequency combs have revolutionised this field by providing a simple, compact and reliable way of measuring optical frequencies in absolute terms and comparing them with each other [12, 38].

Frequency combs are also used in astronomy. It has, for instance, been involved to search for dark matter [39] and for exoplanets around distant stars [13, 40]. By meticulously monitoring the precise colors of light emitted by these stars, subtle fluctuations in motion can be detected, indicating the potential existence of an exoplanet orbiting the star, with characteristics similar to Earth.

Frequency combs also found a use in LIDAR. Traditionally, they have been equipped with a limited number of wavelengths, usually consisting of two "ON/OFF" wavelengths (known as DIAL). Using a frequency comb to scan a broader range of the spectrum enables more robust retrieval techniques and ultimately leads to more precise measurements with reduced biases [41–43].

Last but not least, frequency combs have revolutionized high-resolution spectroscopy [44]. By comparing the comb's evenly spaced frequencies to the absorption or emission spectrum of a sample, its features can be determined [45]. This technique enables the measurement of ultra-narrow spectral lines with exceptional precision, accuracy and speed. As this is a target application for the tri-comb light source, an in-depth study will follow in this manuscript.

1.1.3 Stability of a frequency comb

All the benefits listed above assume that the comb structure is stable. This section details what is underneath the notion of stability applied to a frequency comb.

Stability of an oscillator

Phase noise and frequency stability both characterize the variations in periodic signals, albeit from slightly different perspectives. This subsection is dedicated to the presentation of these two concepts, in order to contextualize the stability measurements made in this thesis. The discussion will be developed based on a monochromatic oscillator. The conclusions drawn from this analysis can then be readily applied to a frequency comb, which can be envisioned as the coherent sum of N monochromatic oscillators (refer to Equation (1.1)). This presentation is

not intended to be exhaustive; readers seeking more detailed information can refer to the cited bibliography for further insights [46].

Phase noise

A oscillator signal affected by amplitude-modulation (AM) and phase-modulation (PM) noise can be written as [47]:

$$v(t) = V_0[1 + \alpha(t)]\cos[2\pi\nu_0 t + \phi(t)] \tag{1.11}$$

where V_0 is the amplitude, ν_0 the frequency, $\alpha(t)$ is the random fractional amplitude, and $\phi(t)$ is the random phase. Generally, the power spectral density $S_v(f)$ of a random process $v(t)$ is defined as:

$$S_v(f) = \mathbb{E}\left\{\mathcal{F}_f\{R_v(t_1, t_2)\}\right\} \tag{1.12}$$

In this equation, $S_v(f)$ represents the power spectral density, $\mathbb{E}$ denotes the expectation operator, $\mathcal{F}$ stands for the Fourier transform, and $R_v(t_1, t_2)$ is the autocorrelation function of the process $v(t)$ at time instants t_1 and t_2. In practice, $S_v(f)$ is measured by applying the Wiener-Khinchin theorem, under the hypothesis that the process v(t) is ergodic, as:

$$S_v(f) = \left|\mathcal{F}_f\{v(t)\}\right|^2 \tag{1.13}$$

Ergodicity entails the interchangeability of ensemble and time-domain statistics, and represents experiment reproducibility. Stationarity implies statistical independence from the time origin, and represents experiment repeatability. In numerous real-world instances, processes exhibit both ergodicity and stationarity [46].

It is common practice in the literature not to refer for phase noise to the power density $S_{\phi(f)}$ (in rad^2/Hz), but rather to the quantity $L(f)$:

$$\mathcal{L}(f) = \frac{\text{SSB power in 1Hz bandwidth}}{\text{carrier power}} \tag{1.14}$$

with SSB refering to single-sideband. This has been defined since the IEEE Standard 1139-1988 [46] as follows:

$$L(f) = \frac{1}{2}S_\phi(f) \tag{1.15}$$

where $S_\phi(f)$ is the PSD of the random process $\phi(t)$. This measurement cannot be made using a traditional spectrum analyser, notably because it is not able to discriminate PM from AM noise, in addition with an inadequate dynamic range. The SSB power is mesured by RF heterodyne detection, by scanning the LO frequency along one side of the line under study. Phase detector saturation allows amplitude noise to be rejected, in order to only select the phase noise. This is the method used in the following of this thesis to characterise the stability of the three developed frequency combs.

Allan deviation

In addition, the quality of a frequency comb is assessed over the long term by measuring the Allan variance of its repetition frequency. The next paragraph presents this physical quantity.

From Equation 1.11, the instantaneous frequency can be computed:

$$\nu(t) = \frac{1}{2\pi}\frac{d}{dt}[2\pi\nu_0 t + \phi(t)] = \nu_0 + \frac{1}{2\pi}\frac{d\phi(t)}{dt} \tag{1.16}$$

From this instantaneous frequency, its instantaneous deviation $\Delta\nu$ can be defined with respect to the reference frequency ν_0 and its normalized instantaneous deviation y(t), respectively:

$$\Delta\nu(t) = \nu(t) - \nu_0 = \frac{1}{2\pi}\frac{d\phi(t)}{dt} \tag{1.17}$$

$$y(t) = \frac{\nu(t) - \nu_0}{\nu_0} = \frac{1}{2\pi\nu_0}\frac{d\phi(t)}{dt} \tag{1.18}$$

The samples y_i are defined by the mean of $y(t)$ over a time τ:

$$y_i = \frac{1}{\tau}\int_{t_i}^{t_i+\tau} y(u)\,du \tag{1.19}$$

This can be further expressed in terms of the difference in phases at instants t_i and $t_i + \tau$:

$$y_i = \frac{\phi(t_i + \tau) - \phi(t_i)}{2\pi\nu_0} \tag{1.20}$$

Their mean over N samples gives $\bar{y}$:

$$\bar{y} = \frac{1}{N}\sum_{i=1}^{N} y_i \tag{1.21}$$

and their "classical" variance σ_y^2 is given by:

$$\sigma_y^2(\tau) = \frac{1}{N-1}\sum_{i=1}^{N}(y_i - \bar{y})^2 \tag{1.22}$$

where N is the total number of samples. Classical variance is a limited tool for describing random phenomena, since it depends on the number N of samples, and diverges if the spectrum decreases in 1/f or steeper [46]. This is why David W. Allan introduces the variance between two samples [48] that converges for all types of noise, and which is called the Allan variance:

$$\sigma_y^2(\tau) = \frac{1}{2(M-1)}\sum_{i=1}^{M-1}(y_{i+1} - y_i)^2 \tag{1.23}$$

where y_i is the ith sample obtained by averaging over time τ = M τ_0, M the number of considered

periods and τ_0 the sampling step. The analysis period cannot exceed half the total measurement duration as a minimum of two samples is required. The Allan variance estimates the stability of an oscillator at different time intervals.

Link between phase noise and Allan deviation

The power spectral density of frequency noise of an oscillator $S_y(f)$ is well modeled by the superposition of five independent types of noise, each corresponding to a different power law (Table 1.1):

$$S_y(f) = \sum_{n=-2}^{\infty} h_n f^n \tag{1.24}$$

where h_n represents the amplitude of the noise component with power law n.

Noise type	Main contribution	$S_y(f)$	$\sigma_y^2(\tau)$
Random Walk Frequency Noise	Oscillator environment (temperature, vibration, shocks, etc.)	f^{-2}	τ^1
Flicker Frequency Noise	Leeson effect supplied by flicker phase/resonator thermal noise	f^{-1}	τ^0
White Frequency Noise	Resonator in band / quantum / thermal noise	f^0	τ^{-1}
Flicker Phase Noise	Up-conversion of the amplifier flicker noise by amplifier non-linearity	f^1	τ^{-2}
White Phase Noise	Thermal / quantum / electronics noise in amplifier	f^2	τ^{-2}

Table 1.1: Frequently encountered types of noise.

An analysis of the phase noise and Allan variation of a frequency comb can therefore help identify the types of noise at stake. These are the tools used to study the effects of the different methods used to stabilize a comb. In the literature, it is usual for the two to complete each other, with an analysis of short-term stability through phase noise measurement, and an analysis of long-term stability with Allan variation measurement.

Referencing of a comb

The repetition rate and the offset frequency are the two degrees of freedom of the spectral structure of a frequency comb. Measuring these two parameters is therefore equivalent to measuring the position of all the spectral teeth. That is what is called *referencing the comb*.

Detection of the repetition rate

The pulse train of a comb can be understood as the constructive interference between all its spectral modes. The greater the number of modes, the greater the modulation and the shorter

the pulses. Direct photo-detection of these pulses is equivalent to heterodyne detection of all the modes beating with one another. Each line of the comb is both signal and LO. Therefore, direct photo-detection enables the measurement of a strong modulation of the amplitude at all the frequency differences within the comb, meaning at every multiple of f_{rep}. In conclusion, the repetition rate can be easily detected using a fast photo-diode [49].

Detection of the offset frequency

It is not the case for the frequency offset, which is in the optical domain. A method has been proposed [49–51] to avoid having to resolve the ultra-rapid oscillations of the carrier wave. It consists of producing a beat at f_0 between one extreme of the comb and the other extreme of its non-linear duplication. The most commonly used effect is frequency doubling, and this technique is called *f-2f self-referencing* [50]. Figure 1.3 describes its principle. It consists in making the 2n mode at frequency ν_{2n} interfere with the mode at frequency $2\nu_n$, generated by frequency doubling the mode n of the comb. The resulting beat is at frequency $2\nu_n - \nu_{2n} = 2(f_{\text{rep}} + f_0) - 2f_{\text{rep}} - f_0 = f_0$.

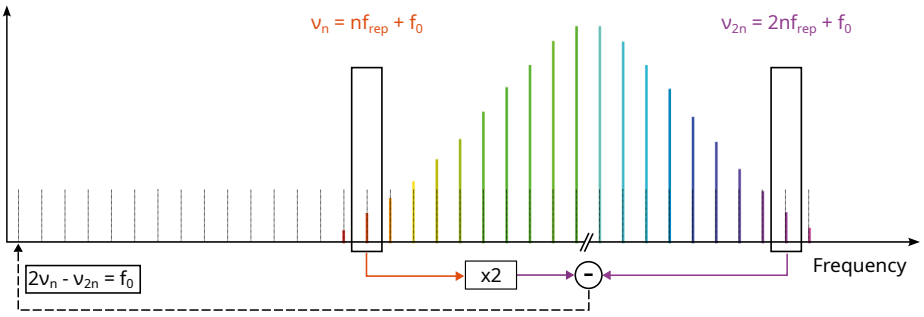

Figure 1.3: Offset frequency detection via f-2f self-referencing.

While this method is mathematically simple, it assumes having access to both mode n and mode 2n. In other words, the spectral spectrum must have a span over an octave. It is one of the motivations behind the development of super-continuum sources [52]. These sources have been developed since the 1970s [53, 54], but their advent coincides with the use of photonic crystal fibers (PCF) [55, 56] or tapered fibers [57]. Their experimental demonstrations have led to the first realisation of self-referenced frequency combs [51].

During my thesis, I used the super-continuum source (spectral bandwidth: 1µm - 2µm) of a commercial C-Comb comb from MenloSystems GmbH, in order to measure its offset frequency. I built an f-2f interferometer, a photograph of which is shown in Figure 1.4. A dichroic mirror separates the high frequencies from the low frequencies on two separate channels. The low frequencies are doubled by Second Harmonic Generation (SHG) in a Periodically poled lithium niobate (PPLN) crystal, then recombined with the high frequencies. Half-wave plates are used to control polarisation on both channels. Different spectral filters are used to select the beat

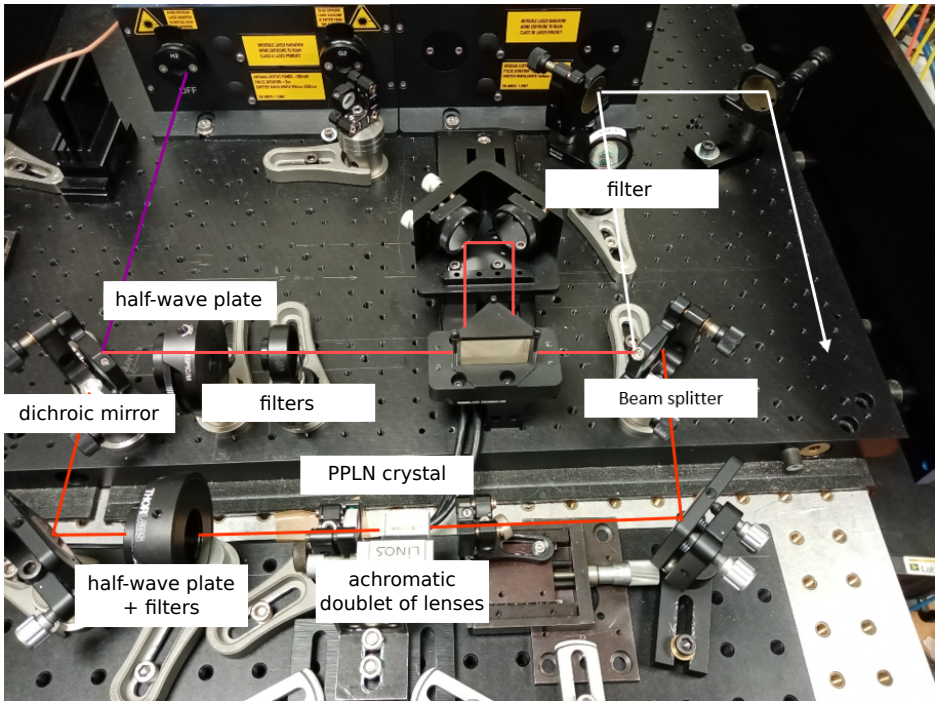

Figure 1.4: Photograph of the f-2f interferometer set-up I developed for the stabilization of the offset frequency of Menlosystems C-combs. The super-continuum beam (purple) is divided into two paths. In the low-frequency channel (red beam), the signal is frequency doubled by passing through a PPLN crystal. On the high-frequency channel (orange beam), a delay line is used to adjust the phase of the initial signal. The two channels are then recombined into a beat detected on a photo-diode.

between the doubled n mode and the 2n mode. A delay line is used to superimpose them in time.

However, this set-up did not result in the measurement of the offset frequency. This is most likely due to the fact that the pulses are too widely dispersed in the crystal that we used (L = 2 cm), which is too long for sub-picosecond durations. This unsuccessful approach highlights the importance of dispersion management with broadband frequency combs. For pulses of 100 to 200 fs, as in the case of the C-Comb of Menlosystems, a less-than-1-mm-long crystal would be more appropriate [58, 59]. This is what will be used by the team to obtain the measurement. Detecting the offset frequency of the comb would enable its locking to a reference source, turning the C-comb source at ONERA into a fully referenced frequency comb (see Appendix A). This improvement could lead to the customization of dual-comb detection protocols, particularly for enhancing the SNR and precision of gas spectroscopy measurements achieved thus far [60]. The specifics of the stabilization process of a frequency comb are elaborated upon in the following.

Locking of a comb

The assessment about the comb's spectral structure relies on its stability. A frequency comb is truly considered as such only if its repetition frequency and offset frequency are stable over time, or at least stable enough to neglect their variations during the measurement time. Indeed, the main property of a comb is its Dirac-like structure. If either of these parameters varies, the fine characteristics of its spectral lines gradually diminish. When the structure that generates the comb is stable enough (the criterion being, of course, the intended application) without any retro-action, the operation is called to be *free-running*. When the initial structure is not stable enough, the comb must be stabilized. To do so, il it possible to lock the self-beatnote from f_{rep} direct detection and the self-beatnote from f_0 indirect detection to microwave references, or only one of them, still depending on the degree of stability required. It is also possible to use known optical references to beat with the comb, and then to lock the beatnotes to microwave references. Since the different modes are all coherent, locking only one or two of them stabilises the other modes of the spectrum. There are alternatives to these stabilization techniques [61], but they remain the most commonly used [62]. Tara Fortier and Esther Baumann provided a illustrated review of the comb performances depending on the stabilization scheme [35]. The comb performances also greatly vary depending on the architecture chosen to generate it, which is the subject of next section.

1.1.4 Common set-ups for comb generation

As presented in Section 1.1, the principle of frequency combs is based on the generation of short pulses. According to Fourier analysis, the shortest pulses are obtained from a large spectrum with a constant phase across all frequencies. Under certain dispersion conditions, this can be achieved using a cavity pumped by a continuous-wave. Those cavity-based configurations are the most common architecture for generating these ultra-short pulses, with two main families: active and passive cavities. Another widespread technology is electro-optic modulation of a continuous-wave laser, which is the technique at the heart of this thesis.

Mode-locked lasers

Frequency comb generation historically relies on the use of mode-locked lasers. These lasers operate by constructive interference between all the longitudinal modes of a cavity. That arises from a large-bandwidth gain medium, pumped by a continuous-wave laser. Kerr-lens effect establishes a fixed phase relationship between all the modes [63]. As a result, the laser emits a train of pulses with a duration as short as a few tens of femtoseconds [64], creating a broad frequency comb spanning over a hundred nanometers. The repetition frequency of these lasers is set by the time of flight in the cavity, and their offset frequency by the residual dispersion. Their value is typically of the order of a hundred MHz [12], and can go from several kHz [65, 66] up to a few GHz [67].

Ti:Sapphire lasers

Until recently, Ti:sapphire lasers have been the most widely used mode-locked lasers. They offer several advantages, including a broad emission spectrum spanning over 300 nm centered at 800 nm, which enables the generation of extremely short pulses with duration of less than 10 fs [68]. That is possible thanks to a precise control of the dispersion, as shown in Figure 1.5. However, despite their capabilities, these lasers come with certain drawbacks. They can be expensive, particularly due to the need for a high-power pump laser in the green region. Thermal lensing effects in the crystal can also limit their output power and their mechanical stability is often a concern for various applications.

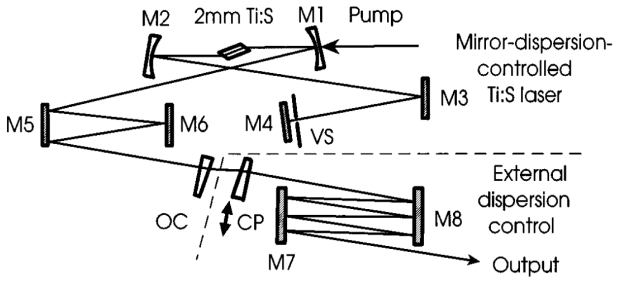

Figure 1.5: Schematic of a Ti:sapphire laser from [68]. M1, M2, quarter-wave dichroic mirrors; M3 – M8, chirped dispersive mirrors; VS, vertical slit; OC, broadband output coupler; CP, wedged glass plate.

Fiber lasers

Fiber lasers are an advantageous alternative to bulk lasers, offering enhanced stability [69]. The most popular types of fiber lasers are erbium-doped and ytterbium-doped fiber lasers, emitting respectively around 1550 nm and 1030 nm. These fiber laser models are gaining popularity and finding more applications, especially since they are commercially available as user-friendly turn-key systems. This is the case with Menlosystem's C-comb model, used as a reference system in this thesis. It is a pulsed laser based on the well-established non-linear Amplifying Loop Mirror (NALM) mode locking mechanism [70]. In a fiber loop mirror (Figure 1.6 (a)), a light pulse gets to a fiber coupler, splitting it at one of its input ports into two equal portions (ⓐ). The two portions propagate in opposite directions and interfere again at the splitter (ⓑ). When the two counter-propagating waves have no phase difference i.e. $\Delta\varphi = 0$, the original pulse is reflected back to where it came from: the fiber loop acts like a mirror (ⓒ).The reflectivity of the loop mirror changes if for some reason there is a phase shift i.e. $\Delta\varphi \neq 0$ between the two counter-propagating pulses (ⓓ). In conclusion, a fiber loop is a device whose transmission/reflection ratio depends on the asymmetry of the phase added by the propagation in the loop. The idea behind NALM is to disymmetrize the propagation in the loop so that the phase shift induced between the two counter-propagating pulses is intensity-dependent. As a result, the transmission

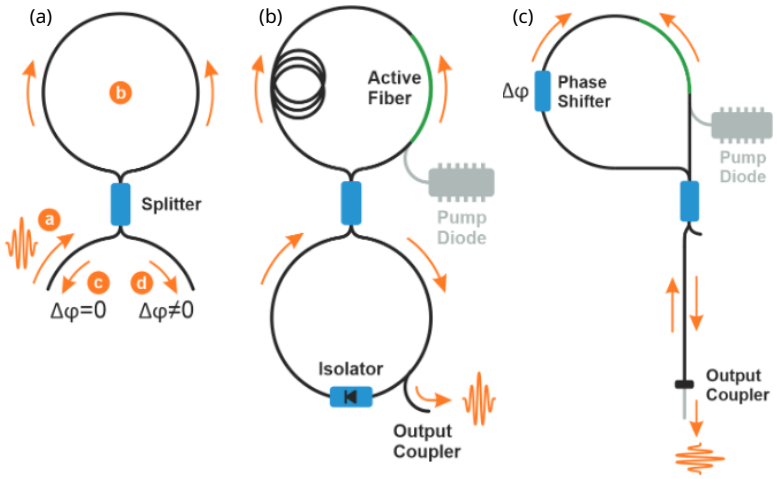

Figure 1.6: Principle of mode-locking in Menlosystem's C-comb laser. (a) Fiber loop mirror. (b) Figure-of-eight laser. (c) Menlosystem's figure 9 design. Courtesy of Menlosystem.

at the coupler is intensity-dependent, and the fiber loop act as a fast artificial saturable absorber (SA). In a figure-of-eight laser (Figure 1.6), the active medium of the laser is a doped optical fiber, whose non-linearity effect is intensity-dependent. Because it is placed asymmetrically with respect to the resonator loops, it induces an intensity-dependent phase difference between the counter-propagating waves. Mode locked laser operation can thus be achieved in this type of cavity. A major drawback of this configuration, however, is the difficulty to achieve self-starting of mode locked operation in polarization-maintaining fibers. That is the reason why Menlosystem's figure 9 (Figure 1.6 (c)) relies on operating the NALM in reflective mode, rather than in transmission, and enables to implement polarization-maintaining fiber components [71].

Micro-resonators

Micro-resonators are miniature optical cavities which confine light in a small volume. Ongoing advancements in microfabrication techniques and material engineering have led to strong light-matter interactions. Figure 1.7 shows an example of the great diversity of existing devices. By carefully designing the geometry and material properties of the micro-resonator, it is possible to achieve ultrafast pulse generation through the phenomenon of cavity soliton [72, 73]. It emerges from a particular solution of the propagation equation in a resonator, based on the interplay of Kerr nonlinearity and optical dispersion [74]. The length of the cavity, which is typically less than 1 mm, determines the repetition rate ranging from tens of gigahertz up to terahertz. Reaching such high values has unlocked many applications [75, 76], from next generation time-domain multiplexed optical networks [9, 38] to multiple wavelength sources for optical interconnects [17, 77]. Micro-resonators offer many other advantages, including compact size, low power consumption, and high stability. Their integration with other photonic

components leads to the development of integrated frequency combs [74, 78, 79].

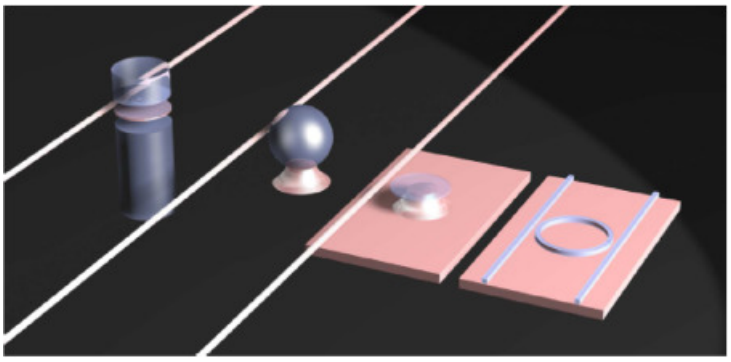

Figure 1.7: Micro-combs have been generated by a large class of resonator devices, such as whispering-gallery mode-based bulk toroids, spheres, monolithic toroids and integrated ring-resonators. From [75].

However, these components do have some disadvantages, such as the low energy conversion and the limited freedom they offer with regard to the parameters of the combs they generate [75].

Tunability of cavity-based set-ups

The setups described above have the particularity of generating periodic pulses from a laser injected into a cavity. In the case of mode-locked lasers, the cavity length can be adjusted by manipulating movable components like mirrors or piezos, leading to a tunability of few mm. The corresponding range of adjustement for the repetition rate is a few kHz. In the case of micro-resonator frequency combs, an external actuation mechanism, such as a heater [80] or a piezoelectric element, is required to mechanically deform the cavity. Adjusting the phase-locking conditions is another option to tune the repetition rate [81], by the use of auxiliary lasers [82], modulation of the pump laser [83] or phase-locked loops [84]. These solutions are technically complicated to implement, and affect the coupling efficiency of the micro-resonator. In conclusion, cavity-based set-ups for comb generation have the major drawback of offering very few tunability of the repetition rate, since it is fixed by the cavity opto-geometrical parameters. This is not the case for frequency combs generated by electro-optic modulation, a technique that offers a wide range of freedom for the parameters of the comb.

Electro-optic modulation

The electro-optic effect is a non-linear phenomenon appearing in anisotropic media, where the refractive index can be affected by the application of a static electric field. This phenomenon, known as the *Pockels effect*, enables to modify the phase of an electromagnetic wave by applying a voltage across a crystal through which the wave propagates. Its application within a specific

configuration can result in the modulation of various other parameters of light. There are elementary electro-optic modulators, whose operation is detailed in Appendix B, which modify the phase, polarization and intensity of a light wave. The performance of such architectures is limited, and they are rarely used in practice [25]. However, they provide insight into how electro-optic modulation works.

In this thesis, a stage of intensity modulation of a continuous laser is employed to generate pulses. This is achieved using Mach-Zehnder modulators (MZM) [85], which are an interferometric structure made from $LiNbO_3$. Applying electric fields to the arms changes optical path lengths resulting in phase modulation. Combining two arms with different phase modulation converts phase modulation into intensity modulation. In our case, the MZM are powered by RF pulses and set at the zero-transmission point using a bias voltage. This configuration facilitates the conversion of RF pulses into optical pulses (see Appendix B for more detail). From a continuous EM wave, electro-optic modulation enables the generation of a train of optical pulses by RF driving. This technique offers a great freedom in the tunability of the repetition rate and the waveform. Like other photonic devices, it has its strengths and weaknesses, as summarized in Table 1.2. For more information, Chang and all provided an exhaustive comparison of the existing integrated optical frequency comb technologies [86].

	Repetition rate	**Pulse duration**	**Tunability**	**Power efficiency**
MLLs	250MHz to 2.5GHz	tens of fs	few kHz	few losses
Micro-combs	GHz to THz	tens of fs if compressed	few GHz to few THz	injection losses
EO-combs	100MHz to 10GHz	tens of ps	completely tunable	modulator losses

Table 1.2: Comparison of the possible devices to generate a frequency comb

We chose the generation of frequency combs through electro-optic modulation because we aimed for frequency agility and ease of use. The main drawback of eo-combs is the pulse duration, whose limited by the bandwidth of the modulators (around 25 GHz). That is why many electro-optic set-ups resort to non-linear effects in optical fibers to broaden the spectrum of the frequency combs. The set-up developed in this thesis leans on the complementary of electro-optic modulation and spectral broadening in non-linear fibers. This latter technique will be the subject of the next section.

1.2 Cartography of the effects in optical fibers

The previous section described what is a frequency comb, how it is used, and presented the photonic devices currently employed to generate such spectral structure. In the associated set-ups, it may be necessary to further broaden the spectrum of the combs, which is generally achieved using an optical fiber. This is especially true for electro-optic combs due to their

narrow spectral width. In this section are presented the theoretical tools to understand the non-linear processes that are used to generate and broaden a frequency comb in a optical fiber. The technical methods to do so are varied and various, as the subject has gained an intense interest over the last decade [87]. This description is not intended to be exhaustive, but simply to introduce the main concepts for interpreting the results of the following chapters. Readers can refer to the bibliographic reference in the field for more details [88].

1.2.1 Light-matter interaction in a optical fiber

As it propagates through an optical fiber, an electromagnetic wave undergoes some physical phenomena.

Linear losses

Due to scattering and material absorption, a light wave that propagates through an optical fiber suffers from losses. The linear attenuation coefficient of an optical fiber is conventionally denoted as α. It quantifies the extent to which the intensity of a signal changes as it propagates through the fiber. The relationship between the output power P_{out} from a fiber with length L and the input power P_{in} is described by the Beer-Lambert law:

$$P_{\text{out}} = P_{\text{in}} \cdot e^{-\alpha L} \tag{1.25}$$

where α is measured in units of m^{-1}. Attenuation is commonly quantified in decibels per kilometer (dB/km), defined as $\alpha_{\text{dB}} = -10 \cdot L \log\left(\frac{P_{\text{out}}}{P_{\text{in}}}\right)$. Modern fibers offer as low as 0.2 dB/km loss at 1.55 µm [88].

Chromatic dispersion

Silica, used in optical fibers, is a dielectric material whose refractive index n depends on the angular frequency ω. This leads to spectral components of an optical pulse propagating at different velocities, due to a phenomenon called dispersion. Considering a spectral width of the signal $\Delta\omega$ negligible compared to the carrier frequency ω_0, chromatic dispersion is generally described using a Taylor expansion of the propagation constant $\beta(\omega) = n(\omega) \times \omega/c$ around ω_0:

$$\beta(\omega) = \sum_{k=0}^{\infty} \frac{\beta_k}{k!}(\omega - \omega_0)^k \tag{1.26}$$

$$= \beta_0 + \beta_1(\omega - \omega_0) + \frac{\beta_2}{2}(\omega - \omega_0)^2 + \frac{\beta_3}{6}(\omega - \omega_0)^3 + (\omega - \omega_0)^3 \tag{1.27}$$

where $\beta_n = \partial^n \beta / \partial \omega^n$. The group velocity dispersion (GVD), represented by the term β_2, is

defined as:

$$\beta_2 = \frac{\partial^2 \beta}{\partial \omega^2} = -\frac{1}{v_g^2}\frac{\partial v_g}{\partial \omega} = \frac{1}{c}\left(2\frac{\partial n}{\partial \omega} + \omega\frac{\partial^2 n}{\partial \omega^2}\right) \tag{1.28}$$

where $v_g = \frac{d\omega}{dk}$ is the group velocity. It's common in the literature to express GVD as:

$$D = \frac{\partial \beta_1}{\partial \lambda} = -\frac{2\pi c}{\lambda^2}\beta_2 \tag{1.29}$$

Unlike the units of β_2 (ps^2/m), the units of D (ps/nm/km) more clearly reflect the physical effect of group velocity dispersion, quantifying the time separation (in ps) between two pulses with central wavelengths differing by 1 nm after propagating 1 km.

The GVD captures the difference in velocity among the component waves of a non-monochromatic signal. It exhibits two distinct regimes determined by the sign of β_2. When $\beta_2 > 0$, the regime is call *normal dispersion*, causing shorter wavelengths to propagate slower than longer wavelengths. Conversely, in the case of $\beta_2 < 0$, the regime is called *anomalous dispersion*, resulting in shorter wavelengths traveling more slowly compared to longer wavelengths. The wavelength for which $\beta_2 = D = 0$ is known as the zero dispersion wavelength (ZDW).

Non-linearity

A single-mode optical fiber has the property of confining light in a small volume, the surface area of which is of the same order of magnitude as its core (around 10 µm in diameter). This confinement explains that the electric field intensity associated with a guided mode within a SMF can reach magnitudes on the order of MW/cm^2. In such cases, the material's electromagnetic response in no longer linearly proportional to the applied field. Because it is a centrosymmetric medium, nonlinear effects in a fiber stem from the third-order susceptibility $\chi^{(3)}$. As a result, most nonlinear effects in optical fibers arise from nonlinear refraction, a phenomenon from which the index is dependent of the intensity. This is called *Kerr effect*, and gives rise to a multitude of intriguing nonlinear phenomena such as Self-Phase Modulation (SPM), Cross-Phase Modulation (XPM), or Four-Wave Mixing (FWM). The most relevant one within the context of this thesis is SPM, which will be the focus of the discussion in section 1.2.3.

Nonlinear effects stemming from the instantaneous third-order susceptibility $\chi^{(3)}$ exhibit an elastic nature, implying no energy exchange between the field and the material. However, an additional category of nonlinear phenomena emerges due to inelastic scattering, involving transfer of energy, such as Brillouin or Raman scatterings. Within this thesis, we demonstrated that these effects do not play a significant role, and they will be negligible in the following of the discussion.

1.2.2 Propagation in an optical fiber

Let us consider a pulse propagating along the z-axis in a single-mode optical fiber. This pulse is characterized by its electric field A(r,t), with the envelope assumed to vary slowly compared to the rapid variations of the carrier wave (Slowly Varying Envelope Approximation, SVEA). It is assumed that the pulses are sufficiently intense to induce a non-linear response of the material composing the fiber. In our configuration, we neglect dispersion of order greater than 2 and inelastic non-linear terms. For all results presented in this manuscript, we checked that these assumptions were relevant. Under these conditions, Maxwell's equations can be applied to the envelop, in the frame moving at the group velocity of the wave (z, t). A(z, t) therefore satisfies:

$$i\frac{\partial A}{\partial z} + i\frac{\alpha}{2}A - \frac{\beta_2}{2}\frac{\partial^2 A}{\partial t^2} + \gamma|A|^2 A = 0 \tag{1.30}$$

This equation is called *non-linear Schrödinger Equation* (NLSE). It introduces several characteristic parameters of pulse propagation in an optical fiber:

- α is the absorption coefficient (in cm^{-1}), which quantifies the linear attenuation of the pulse's intensity due to absorption in the fiber material.
- β_2 is the second-order dispersion coefficient (in $\mathrm{s}^2 \cdot \mathrm{m}^{-1}$), which describes how the pulse broadens or narrows due to the different group velocities of its spectral components.
- γ is the non-linear coefficient or Kerr coefficient (in $\mathrm{W}^{-1} \cdot \mathrm{m}^{-1}$), which characterizes the strength of the non-linear response of the fiber material. It determines how the pulse interacts with itself through Kerr effect.

The NLSE is an approximate equation that is suitable in the case of our studies. The effects of dispersion are only taken into account up to the second order, and inelastic effets such as the Raman effect are neglected. It is this simpler form of the NLSE that was developed for the first time in the 1970s, and it was only later that the generalized nonlinear Schrödinger equation (GNLSE) [88] was derived [89]. The NLSE depicts the propagation of the wave in a fiber as a interaction between the losses, the dispersion and the $\chi^{(3)}$ non-linearity. It is possible to define a length beyond which the Kerr effect becomes significant, the non-linear length L_{NL} defined as:

$$L_{\mathrm{NL}} = \frac{1}{\gamma P_0} \tag{1.31}$$

where P_0 is the peak power of the injected pulse. Similarly, it is possible to define a characteristic length at which dispersive effects become significant. This is the dispersion length L_D defined as:

$$L_D = \frac{\delta_0^2}{|\beta_2|} \tag{1.32}$$

where δ_0 is the temporal full-width at half-maximum (FWHM) of the pulse intensity. These two quantities help to evaluate, based on the initial conditions and fiber parameters, which

effects dominate during propagation. For some specific applications which require high spectral broadening, optical fibers can be engineered in order for non-linearity to predominate [56, 90, 91].

1.2.3 Self-Phase modulation

As presented in Eq. 1.30, intense pulses propagating in a fiber induce an optical response of the medium through the non-linear term $\gamma|A|^2A$. This response leads to a dependence of the fiber's refractive index on the electric field intensity, known as the Kerr effect, and the refractive index can be written as:

$$n(\omega) = n_0(\omega) + n_2\frac{|A|^2}{A_{\text{eff}}} \quad \text{with} \quad A_{\text{eff}} = \frac{(\iint_{\mathbb{R}^2}|A(x,y)|^2\,dx\,dy)^2}{\iint_{\mathbb{R}^2}|A(x,y)|^4\,dx\,dy} \tag{1.33}$$

where n_0 is the linear refractive index, n_2 is the non-linear refractive index (in $m^2.W^{-1}$) and A_{eff} is the effective area of the fiber associated with the spatial mode function $A(x,y)$. The Kerr coefficient is related to the non-linear index by the equation:

$$\gamma = \frac{2\pi n_2}{\lambda A_{\text{eff}}} \tag{1.34}$$

Non-linear fibers can be engineered to obtain the highest possible value for the parameter γ while minimizing losses and dispersion [88]. In this case, L_{NL} is smaller than L_D and the dispersion term of Eq. 1.30 can be neglected. While also neglecting the linear losses, the propagation equation in a purely non-linear fiber becomes:

$$i\frac{\partial A}{\partial z} + \gamma|A|^2A = 0 \tag{1.35}$$

and its solution is given by:

$$A(L,t) = A(0,t)e^{i\gamma|A|^2L} \tag{1.36}$$

The phase of the impulsion is modified during the propagation of a quantity $\gamma|A|^2z$ that depends of the wave itself. Therefore, there is a modulation of the phase by the impulsion itself: it is Self-Phase Modulation.

Because any temporal variation of the phase affects the instantaneous frequency of the pulse, SPM leads to changes in the optical spectrum. When the pulse is initially without chirp or with positive chirp, SPM results in spectral broadening, expanding the optical bandwidth. Conversely, if the initial pulse has negative chirp (assuming a positive nonlinear index), there can be spectral compression. In our case, an initially unchirped pulse interacts with a $\chi^{(3)}$ medium with $n_2 > 0$ and negligible dispersion ($L_D > L_{NL}$). SPM introduces some positive chirp, and we obtain a broadening of the spectrum (see Figure 1.8 (b)). It displays oscillations. That stems from the fact that, depending on the temporal profile $A(z=0,t)$, there are two times where the induced

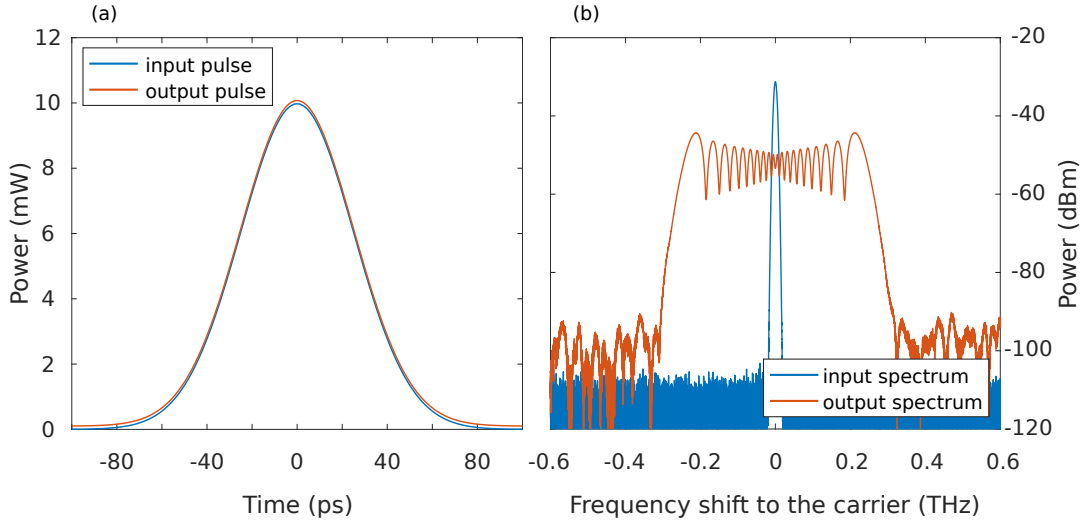

Figure 1.8: SPM simulation for a gaussian pulse of 50 ps at P_0 = 14 W (P_{avg} = 350 mW at 500 MHz of repetition rate) in a fiber of L = 1 km and γ = 5 $W^{-1}.km^{-1}$ at 1550 nm. Linear effects have been neglected to isolate the contribution solely related to SPM. (a) Temporal profile of the pulses before and after propagation. The amplitude of the output pulse has been slightly shifted to be able to distinguish the two curves. (b) Spectral envelop of the pulses before and after propagation.

instantaneous frequency is similar [92]. As a consequence, the Fourier integral for a specific frequency component receives contributions from different time instances. Depending on the precise frequency, these contributions may either enhance or cancel each other out, resulting in oscillations in the spectrum. As for it, the temporal profile remains unchanged, as pictured in Figure 1.8 (a). Because the added phase term $\gamma|A|^2z$ has the same periodicity as A(z=0,t), the comb structure of the spectrum, as previously derived, is not affected. This is why it is such a powerful tool to broaden the spectrum of a frequency comb [93, 94], keeping the phase relationship between all its modes. SPM-induced broadening was first observed in a liquid-filled cell [95], and then demonstrated in optical fibers 10 years later by R.H. Stolen and C. Lin [96]. Given the inherent stability of fiber systems, it has become feasible to distinctly observe the increase of the broadening as the input peak power became bigger. Stolen and Lin also dissected the impact of the pulse's temporal shape on the SPM-induced spectral envelope, which is something that will be relevant from the setting of our tri-comb system (see section 2.1.3).

SPM is a particular case of the Kerr effect, where a single optical wave propagates in a non-linear fiber and interacts with itself. This phenomenon is naturally phase-matched. However, there is a more general scenario in which, under certain conditions, multiple waves interact and generate new waves.

1.2.4 Four Wave Mixing

In the case where A(z,t) no longer represents a single optical wave but the sum of multiple waves, the NSLE is no longer a single equation (see Eq. 1.1) but a system of coupled equations [88, 97].

Let's take the example of four waves at the respective frequency ω_1, ω_2, ω_3, and ω_4, with respective envelop A_1, A_2, A_3 and A_4. Always within SVEA, their superposition at the entry of a non-linear fiber gives rise to $A = A_1 + A_2 + A_3 + A_4$. NLSE applied to A leads to [88]:

$$\frac{\partial A_1}{\partial z} = -\frac{\beta_2}{2}A_1 + i\gamma\left(|A_1|^2 + 2|A_2|^2 + 2|A_3|^2 + 2|A_4|^2\right)A_1 + 2A_3A_4A_2^*e^{i\Delta\beta z} \tag{1.37}$$

$$\frac{\partial A_2}{\partial z} = -\frac{\beta_2}{2}A_2 + i\gamma\left(|A_2|^2 + 2|A_1|^2 + 2|A_3|^2 + 2|A_4|^2\right)A_2 + 2A_3A_4A_1^*e^{i\Delta\beta z} \tag{1.38}$$

$$\frac{\partial A_3}{\partial z} = -\frac{\beta_2}{2}A_3 + i\gamma\left(|A_3|^2 + 2|A_1|^2 + 2|A_2|^2 + 2|A_4|^2\right)A_3 + 2A_1A_2A_4^*e^{-i\Delta\beta z} \tag{1.39}$$

$$\frac{\partial A_4}{\partial z} = -\frac{\beta_2}{2}A_4 + i\gamma\left(|A_4|^2 + 2|A_1|^2 + 2|A_2|^2 + 2|A_3|^2\right)A_4 + 2A_1A_2A_3^*e^{-i\Delta\beta z} \tag{1.40}$$

where $\Delta\beta = \beta(\omega_1) + \beta(\omega_2) - \beta(\omega_3) - \beta(\omega_4)$ is called the *phase mismatch*. This system reveals all manifestations of the Kerr effect and the dispersion from the interactions between the different waves. Let's take the example of wave A_1 to detail these interactions. The term $|A_1|^2$ represents SPM. The term $2|A_2|^2 + 2|A_3|^2 + 2|A_4|^2$ corresponds to XPM, indicating the influence of the intensity of waves A_2, A_3, and A_4 on wave A_1. Lastly, the term $2A_3A_4A_2^*\exp(i\Delta\beta z)$ represents FWM, which involves energy exchange among the four waves. This term is sensitive to the phase of the waves, and the coupling efficiency depends on the phase mismatch $\Delta\beta$. Indeed, contrary to SPM, the efficiency of the FWM phenomenon depends on phase matching between the interacting waves. In our case, it is approximately given because the frequencies involved are very close to each other, meaning the chromatic dispersion profile is flat over this small range. In other cases, it is possible to balance the dispersion by utilizing various waveguide modes, as it was the case for the first observation of three-wave mixing in optical fibers [97].

The same system of equations dictates the generation of new waves at frequencies ω_3 and ω_4 from two pump waves at frequencies ω_1 and ω_2. This case is studied in Chapter 4 of this manuscript. FWM from two pump waves is a powerful non-linear technique to obtain broadband optical frequency combs, with improved performance and flexibility compared to traditional single pump methods [98, 99]. One of the key advantages of dual-pump frequency comb generation is the enhanced control over the generated comb spectrum [98]. By carefully adjusting the parameters of the two pump sources, such as their relative frequencies, powers, and phase difference, one can tailor the resulting frequency comb properties, including the spacing between the comb lines. This flexibility demonstrates the dual-pump scheme to be an optimal approach to generate high repetition rates (GHz-THz) frequency combs in both cavity-less [100–103] and micro-cavity schemes [82, 104–107].

1.3 Dual-comb interferometry

The previous section described the non-linear phenomena in optical fibers involved in the generation and spectral broadening of frequency combs. Indeed, depending on the desired application, a large number of modes may be required. This is the case in spectroscopy, where the use of combs has deeply impacted the field, by providing broadband measurements with high spectral resolution. The first experimental demonstrations of this method date back to the early 1990s [108], and would be rewarded with the Nobel Prize in Physics in 2005 for the teams of T.H. Hansch and J. Hall [16, 17].

1.3.1 Principle

The utilization of two frequency combs in an interferometric configuration has introduced a groundbreaking approach to Fourier Transform Infra-red spectroscopy (FTIR) [109]. This innovative method, initially proposed by Schiller in 2002 [18], eliminates the need for scanning components by optically sampling one frequency comb with another comb at a slightly different repetition rate. That allows for the instrument's limitations on speed and resolution to be removed [20, 110] The overlapping of the two frequency combs using a beam combiner generates a RF comb, which can be detected using a low-bandwidth photo-detector (PD). The signal of the detector output is a function of time and is called the *interferogram*. Mathematically, this interferogram g is the superposition of C_1 and C_2, two frequency combs as defined in Eq. 1.1, at the respective repetition rate f_{rep1} and f_{rep2}, with the respective offset f_{01} and f_{02}, and at the respective carrier frequency f_{p1} and f_{p2}. The interferogram can be written as:

$$g(t) = C_1(t) + C_2(t) \tag{1.41}$$

Unlike the calculation of the optical spectra discussed in Section 1.1.1, here we are interested in calculating the spectrum of the RF signal generated by the PD also known as the *electrical spectrum*. We emphasize this distinction by denoting the variable of the Fourier Transform as ω_{RF}. The rigorous way to calculate the power spectrum of an ergodic process [111] is to consider the autocorrelation function and then to apply the Wiener-Khintchine Theoreme [112]. An alternative (and more concise) method [18] is to express the detected RF signal as $|g(t)|^2$, and

then to look at its FT:

$$\begin{aligned}\tilde{g}_{RF}(\omega_{\mathrm{RF}}) &= \mathcal{F}\,\omega_{\mathrm{RF}}(|g(t)|^2)\\ &= \mathcal{F}_{\omega_{\mathrm{RF}}}\left(|C_1(t)+C_2(t)|^2\right)\\ &= \mathcal{F}_{\omega_{\mathrm{RF}}}\left(|C_1(t)|^2+|C_2(t)|^2+2C_1(t)C_2(t)\right)\\ &= \tilde{C}_{\mathrm{RF1}}(\omega_{\mathrm{RF}})+\tilde{C}_{\mathrm{RF2}}(\omega_{\mathrm{RF}})+2\mathcal{F}_{\omega_{\mathrm{RF}}}\left(C_1(t)C_2(t)\right)\\ &= \tilde{C}_{\mathrm{RF1}}(\omega_{\mathrm{RF}})+\tilde{C}_{\mathrm{RF2}}(\omega_{\mathrm{RF}})+\underbrace{2\tilde{C}_1(\omega_{\mathrm{RF}})*\tilde{C}_2(\omega_{\mathrm{RF}})}_{\text{interference term}}\end{aligned} \tag{1.42}$$

One can note that Eq. 1.1 defines $C_1(t)$ and $C_2(t)$ in $\mathfrak{Re}$, which allows to develop $|C_1(t)+C_2(t)|^2$ as above.

Down-conversion in the RF domain

The first two terms of this expression $\tilde{C}_{\mathrm{RF1}}\omega_{\mathrm{RF}})$ and $\tilde{C}_{\mathrm{RF2}}(\omega_{\mathrm{RF}})$ correspond to the power spectra of combs 1 and 2, i.e. a multitude of lines spaced by the respective quantities f_{rep1} and f_{rep2}. The last term $2\tilde{C}_1(\omega_{\mathrm{RF}})*\tilde{C}_2(\omega_{\mathrm{RF}})$ corresponds to the interference between the two combs, and it's precisely this expression that contains all the dual-comb strucure. Taking the expression of the spectra in the form of dirac combs (see Eq. 1.9), one can find [25]:

$$\begin{aligned}\tilde{C}_1(\omega_{\mathrm{RF}})*\tilde{C}_2(\omega_{\mathrm{RF}}) = &\left(\pi\omega_{\mathrm{rep1}}\tilde{A}(\omega_{\mathrm{RF}}-\omega_{p1})\mathrm{III}_{\omega_{\mathrm{rep1}}}(\omega_{\mathrm{RF}}-\omega_{01})+\pi\omega_{\mathrm{rep1}}\tilde{A}(\omega_{\mathrm{RF}}+\omega_{p1})\mathrm{III}_{\omega_{\mathrm{rep1}}}(\omega_{\mathrm{RF}}+\omega_{01})\right)\\ &*\left(\pi\omega_{\mathrm{rep2}}\tilde{A}(\omega_{\mathrm{RF}}-\omega_{p2})\mathrm{III}_{\omega_{\mathrm{rep2}}}(\omega_{\mathrm{RF}}-\omega_{02})+\pi\omega_{\mathrm{rep2}}\tilde{A}(\omega_{\mathrm{RF}}+\omega_{p2})\mathrm{III}_{\omega_{\mathrm{rep2}}}(\omega_{\mathrm{RF}}+\omega_{02})\right)\end{aligned} \tag{1.43}$$

The development of this expression therefore introduces four different $\mathcal{P}_{i\in[\![1\ ;\ 4]\!]}(\omega_{\mathrm{RF}})$ terms of similar structure, but centered at different frequencies:

$$\begin{aligned}\tilde{C}_1(\omega_{\mathrm{RF}})*\tilde{C}_2(\omega_{\mathrm{RF}}) \propto &\left(\tilde{A}(\omega_{\mathrm{RF}}-\omega_{p1})\mathrm{III}_{\omega_{rep1}}(\omega_{\mathrm{RF}}-\omega_{01})\right)*\left(\tilde{A}(\omega_{\mathrm{RF}}+\omega_{p2})\mathrm{III}_{\omega_{rep2}}(\omega_{\mathrm{RF}}+\omega_{02})\right)\Big\}\mathcal{P}_1(\omega_{\mathrm{RF}})\\ &+\left(\tilde{A}(\omega_{\mathrm{RF}}+\omega_{p1})\mathrm{III}_{\omega_{rep1}}(\omega_{\mathrm{RF}}+\omega_{01})\right)*\left(\tilde{A}(\omega_{\mathrm{RF}}-\omega_{p2})\mathrm{III}_{\omega_{rep2}}(\omega_{\mathrm{RF}}-\omega_{02})\right)\Big\}\mathcal{P}_2(\omega_{\mathrm{RF}})\\ &+\left(\tilde{A}(\omega_{\mathrm{RF}}-\omega_{p1})\mathrm{III}_{\omega_{rep1}}(\omega_{\mathrm{RF}}-\omega_{01})\right)*\left(\tilde{A}(\omega_{\mathrm{RF}}-\omega_{p2})\mathrm{III}_{\omega_{rep2}}(\omega_{\mathrm{RF}}-\omega_{02})\right)\Big\}\mathcal{P}_3(\omega_{\mathrm{RF}})\\ &+\left(\tilde{A}(\omega_{\mathrm{RF}}+\omega_{p1})\mathrm{III}_{\omega_{rep1}}(\omega_{\mathrm{RF}}+\omega_{01})\right)*\left(\tilde{A}(\omega_{\mathrm{RF}}+\omega_{p2})\mathrm{III}_{\omega_{rep2}}(\omega_{\mathrm{RF}}+\omega_{02})\right)\Big\}\mathcal{P}_4(\omega_{\mathrm{RF}})\end{aligned} \tag{1.44}$$

The $\mathcal{P}_3$ and $\mathcal{P}_4$ terms are centered at - $(\omega_{p1}+\omega_{p2})$ and + $(\omega_{p1}+\omega_{p2})$ respectively, which means that their carrier frequencies are well outside the PD bandwidth, and are not detected. The terms $\mathcal{P}_1$ and $\mathcal{P}_2$ are centered in 0 and represent all possible frequency combinations between the different pairs of comb 1 and comb 2 lines. This can be understood mathematically by using

Eq. 1.4 to develop $\mathcal{P}_1$ for instance:

$$\tilde{A}(\omega_{\mathrm{RF}}-\omega_{p1})\mathrm{III}_{\omega_{rep1}}(\omega_{\mathrm{RF}}-\omega_{01})=\sum_{n_1=-\infty}^{\infty}\tilde{A}(n_1\omega_{rep1}+\omega_{01}-\omega_{p1})\delta(\omega_{\mathrm{RF}}-\omega_{01}-n_1\omega_{rep1}) \quad (1.45)$$

and

$$\tilde{A}(\omega_{\mathrm{RF}}+\omega_{p2})\mathrm{III}_{\omega_{rep2}}(\omega_{\mathrm{RF}}+\omega_{02})=\sum_{n_2=-\infty}^{\infty}\tilde{A}(n_2\omega_{rep2}-\omega_{02}+\omega_{p2})\delta(\omega_{\mathrm{RF}}+\omega_{02}-n_2\omega_{rep2}) \quad (1.46)$$

leading to:

$$\begin{aligned}\mathcal{P}_1(\omega_{\mathrm{RF}})=&\left(\sum_{n_1=-\infty}^{\infty}\tilde{A}(n_1\omega_{\mathrm{rep1}}+\omega_{01}-\omega_{p1})\delta(\omega_{\mathrm{RF}}-\omega_{01}-n_1\omega_{\mathrm{rep1}})\right)\\&*\left(\sum_{n_2=-\infty}^{\infty}\tilde{A}(n_2\omega_{\mathrm{rep2}}-\omega_{02}+\omega_{p2})\delta(\omega_{\mathrm{RF}}+\omega_{02}-n_2\omega_{\mathrm{rep2}})\right)\end{aligned} \quad (1.47)$$

Let's consider the simple case where the comb carriers are spaced by less than the smallest of the repetition frequencies, say $f_{\mathrm{rep1}}<f_{\mathrm{rep2}}$. The pairs that give the lowest frequency combinations are the neighboring pairs, i.e. the lines of combs 1 and 2 associated with the same number $n=-n_1=n_2$. The minus sign comes from the fact that the positive frequencies of one comb are convoluted with the negative frequencies of the other. The previous expression can then be truncated into a simple sum:

$$\mathcal{P}_1(\omega_{\mathrm{RF}})=\sum_{n=-\infty}^{\infty}\tilde{A}(-n\omega_{\mathrm{rep1}}+\omega_{01}-\omega_{p1})\tilde{A}(n\omega_{\mathrm{rep2}}-\omega_{02}+\omega_{p2})\delta(\omega_{\mathrm{RF}}-\omega_{01}+n\omega_{\mathrm{rep1}})*\delta(\omega_{\mathrm{RF}}+\omega_{02}-n\omega_{\mathrm{rep2}}) \quad (1.48)$$

For simplicity of writing, and therefore ease of understanding, $\tilde{A}$ is assumed to be symmetrical. Therefore it is possible to write $\tilde{A}(-n\omega_{\mathrm{rep1}}+\omega_{01}-\omega_{p1})=\tilde{A}(n\omega_{\mathrm{rep1}}-\omega_{01}+\omega_{p1})$. It is also assumed that the frequency differences $\Delta\omega_{rep}=\omega_{\mathrm{rep2}}-\omega_{\mathrm{rep1}}$, $\Delta\omega_0=\omega_{02}-\omega_{01}$ and $\Delta\omega_p=\omega_{p2}-\omega_{p1}$ are small compared with the variations in the spectral envelope $\tilde{A}$. From that, it is deduced that $\tilde{A}(-n\omega_{\mathrm{rep1}}+\omega_{01}-\omega_{p1})\approx\tilde{A}(n\omega_{\mathrm{rep2}}-\omega_{02}+\omega_{p2})\approx\tilde{A}(n\omega_{\mathrm{rep}}-\omega_0+\omega_p)$ with $\omega_{\mathrm{rep}}=\frac{\omega_{\mathrm{rep1}}+\omega_{\mathrm{rep2}}}{2}$, $\omega_0=\frac{\omega_{01}+\omega_{02}}{2}$ and $\omega_{\mathrm{p}}=\frac{\omega_{\mathrm{p1}}+\omega_{\mathrm{p2}}}{2}$. The interference between the two frequency combs then gives:

$$\mathcal{P}_1(\omega_{\mathrm{RF}})=\sum_{n=-\infty}^{\infty}\tilde{A}^2(n\omega_{\mathrm{rep}}-\omega_0+\omega_p)\delta(\omega_{\mathrm{RF}}-\omega_{01}+n\omega_{\mathrm{rep1}})*\delta(\omega_{\mathrm{RF}}+\omega_{02}-n\omega_{\mathrm{rep2}}) \quad (1.49)$$

And according to the convolution property between diracs:

$$\mathcal{P}_1(\omega_{\mathrm{RF}})=\sum_{n=-\infty}^{\infty}\tilde{A}^2(n\omega_{\mathrm{rep}}-\omega_0+\omega_p)\delta(\omega_{\mathrm{RF}}+\Delta\omega_0-n\Delta\omega_{\mathrm{rep}}) \quad (1.50)$$

And by taking this time $n = n_1 = -n_2$, $\mathcal{P}_2(\omega_{\mathrm{RF}})$ is found to be the symmetrical expression, containing the same spectral information:

$$\mathcal{P}_2(\omega_{\mathrm{RF}}) = \sum_{n=-\infty}^{\infty} \tilde{A}^2(-n\omega_{\mathrm{rep}} - \omega_0 + \omega_p)\delta(\omega_{\mathrm{RF}} + \Delta\omega_0 + n\Delta\omega_{\mathrm{rep}}) \tag{1.51}$$

The low-frequency terms $\mathcal{P}_1(\omega_{\mathrm{RF}})$ and $\mathcal{P}_2(\omega_{\mathrm{RF}})$ thus map the envelope value in the optical domain $\omega_p - \omega_0 \pm n\omega_{\mathrm{rep}}$ to the RF frequencies $\omega_{\mathrm{RF}} = \Delta\omega_0 \pm n\Delta\omega_{\mathrm{rep}}$. This conversion is clearly understood by introducing the scaling factor:

$$a = \frac{f_{\mathrm{rep}}}{\Delta f_{\mathrm{rep}}} \tag{1.52}$$

That enables to use the expression of the mean offset frequency $\omega_0 = \frac{\omega_{\mathrm{rep}}}{2\pi\Delta\phi}$ to write at the first order $\Delta\omega_0 = \frac{\Delta\omega_{\mathrm{rep}}}{2\pi\Delta\phi} = \frac{\omega_0}{a}$. From that, one can write:

$$\begin{aligned}\mathcal{P}_1(\omega_{\mathrm{RF}}) &= \sum_{n=-\infty}^{\infty} \tilde{A}^2\Big(a\cdot(n\Delta\omega_{\mathrm{rep}} - \Delta\omega_0) + \omega_p\Big)\delta\Big(\omega_{\mathrm{RF}} - (n\Delta\omega_{\mathrm{rep}} - \Delta\omega_0)\Big) \\ &= \tilde{A}^2\Big(a\cdot(\omega_{\mathrm{RF}} - \Delta\omega_0) + \omega_p\Big)\mathrm{Ш}_{\Delta\omega_{\mathrm{rep}}}(\omega_{\mathrm{RF}} - \Delta\omega_0)\end{aligned} \tag{1.53}$$

This expression is that of a comb in the RF domain, at the frequency $\Delta\omega_{\mathrm{rep}}$ and with an offet frequency of $\Delta\omega_0$. This RF comb is a replica of the optical combs. Indeed, one can retrieve the optical spectrum by converting the frequencies ω_{RF} using the operation $a\cdot(\omega_{\mathrm{RF}} - \Delta\omega_0) + \omega_p$. This technique based on the multi-heterodyne detection of the two combs is called *dual-comb interferometry*, and is commonly referred as *dual-comb spectroscopy* for being particularly used to measure the optical spectrum of a sample. This is illustrated in Figure 1.9. Following the reasoning of heterodyne detection in 1.1.2, each tooth of the first comb interfere with the closest teeth of the second comb, which creates a sum of peaks all spaced by a frequency of $\Delta\omega_{\mathrm{r}}$, meaning the creation of the RF comb. The amplitude of each RF peak is therefore the product of the amplitudes of the two interfering optical peaks.

The interferogram

The whole concept of double-comb interferometry is to make the measurement of optical spectra accessible. The RF comb contains all the necessary information and is easy to detect. In fact, a simple PD with a bandwidth of $\frac{f_{\mathrm{rep}}}{2}$ is enough to calculate it from the TF of the interferogram. Figure 1.10 shows a schematic of the interferogram, plotted as a function of time. At each iteration, i.e. every $1/f_{\mathrm{rep}}$, the difference in repetition frequency creates a temporal step between the comb1 pulse and the comb2 pulse of $\Delta\mathrm{t} = 1/f_{\mathrm{rep}} - 1/(f_{\mathrm{rep}} + \Delta f_{\mathrm{rep}}) \approx \Delta f_{\mathrm{rep}}/f_{\mathrm{rep}}^2$. Each pulse of comb2 therefore samples a different point in the comb1 signal. This creates the optical analogue of the Vernier effect. The interferogram therefore consists of regularly spaced bursts, corresponding to the temporal overlap of the two combs. The burst repetition period is equal to

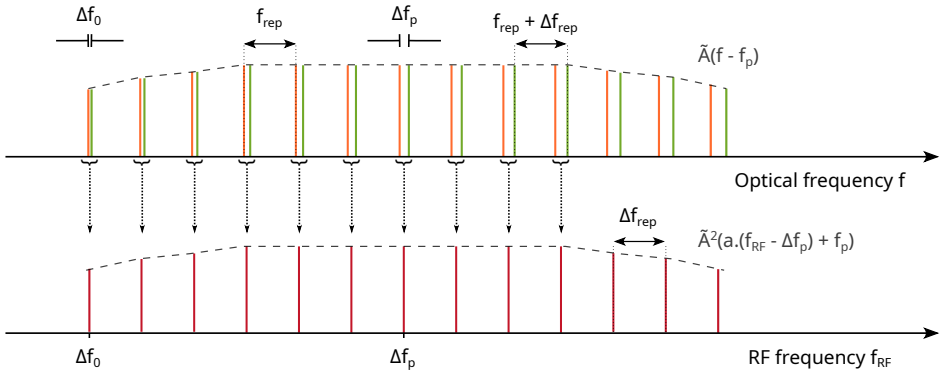

Figure 1.9: Principle of dual-comb interferometry. Two frequency combs with a repetition frequency of f_{rep} (orange comb) and $f_{\text{rep}} + \Delta f_{\text{rep}}$ (green comb) interfere. The detection of the interference signal by a PD down-converts the combs in the RF domain with a repetition frequency of Δf_{rep}.

$1/\Delta f_{\text{rep}}$, the time taken for the two combs to synchronise again.

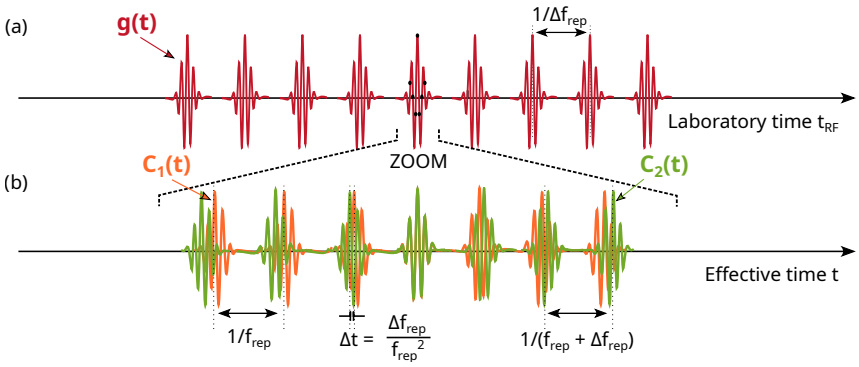

Figure 1.10: (a) The interferogram. The signal generated by the photo-diode consists of regularly spaced bursts, which correspond to the temporal overlap of the two frequency combs. The repetition period of these bursts is equal to $1/\Delta f_{\text{rep}}$, representing the delay required for the two combs to synchronize once again. (b) Optical sampling: zoom on one burst of the interferogram. Due to the different repetition rates, the pulses from each electromagnetic wave slowly drift past one another with a time difference of ΔT at each pulse iteration. This phenomenon leads to an optical sampling, marked as the black points in the upper part of the figure.

1.3.2 Operating conditions

The previous section provides a detailed description of the phenomenon of down-conversion by dual-comb interferometry. The lowest frequencies result from the interference between neighboring lines of comb 1 and comb 2 (ν_{n_1} and ν_{n_2}, where $n_1 = -n_2$). By generalizing the

expression of $\mathcal{P}_1$ given by Eq. 1.53 to $|n_1| \neq |n_2|$, the electrical spectrum is not only restricted to the lowest frequencies, but is composed of all the lines of one comb beating with all the lines of the other one. Its structure therefore consists of multiple RF combs with the same Δf_{rep} spacing, and centered at $(|n_1| - |n_2|) f_{\text{rep}} \pm \Delta f_p$. Thus, there are a pattern repetition each f_{rep}, setting a bandwidth for each pattern of $f_{\text{rep}}/2$, as schematized in Figure 1.11.

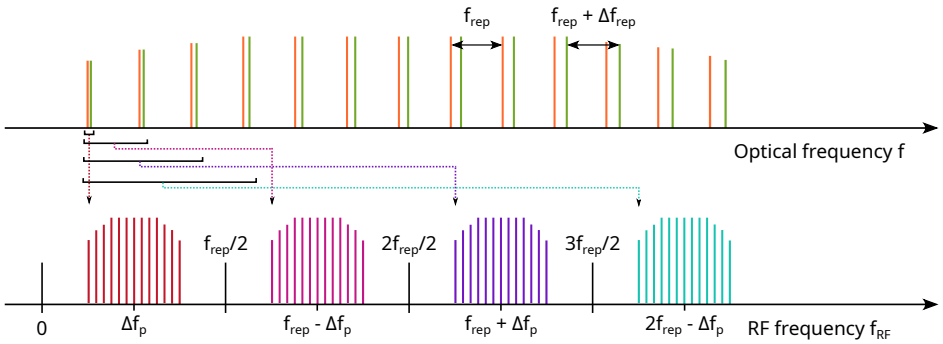

Figure 1.11: Scheme of the principle of the down-conversion by dual-comb interferometry. In the optical domain, a tooth of comb1 (orange) beats with the nearest comb2 (green) tooth, but also with all the other ones. In the RF domain, these multiple beats create several quasi-identical RF combs, centered at $m f_{\text{rep}} \pm \Delta f_p, m \in \mathbb{N}$.

The requirements of a spectroscopic measurement set the needed spectral width $\Delta\nu$ and spectral resolution f_{rep}. Given those parameter, the RF width Δf_{RF} is calculated thanks to the down-conversion factor a as $\Delta f_{\text{RF}} = a \times \Delta\nu$. In order to avoid any ambiguity while assigning the comb modes, and considering only the beat between neighboring lines, the bandwidth of each repeated comb pattern should not exceed half of the repetition frequency: $\Delta f_{\text{RF}} < \frac{f_{\text{rep}}}{2}$. This is the first constraint on the choice of the parameters $\Delta\nu$, f_{rep} and Δf_{rep}. However, one should not forget that the low-frequencies RF comb is centered at Δf_p (see Figure 1.9). The optimized configuration is therefore $\Delta f_p = f_{\text{rep}}/4$, where the whole [0 - $f_{\text{rep}}/2$] bandwidth is available, as chosen is Figure 1.11. However, if experimental constraints prevent from being in this ideal configuration, then the other parameters have to be adapted to avoid overlapping of the different RF combs.

This is the case for this work. Indeed, the difference of carrier frequencies are set by accousto-optic modulators (AOMs) of respectively 100 MHz and 200 MHz. These values are fixed, while the repetition frequencies of the set-up can be entirely tunable. This is why the RF bandwidth $f_{\text{rep}}/2$ and spectral resolution Δf_{rep} are adapted to the RF offsets, and not the other way around. Figure 1.12 shows two examples of recorded RF spectrum from the same comb sources interfering, with same optical width $\Delta\nu = 0.8$ THz, carrier offset $\Delta f_p = 200$ MHz and repetition rate $f_{\text{rep}} = 500$ MHz, but with two distinct repetition rate differences Δf_{rep}. In the first case (Figure 1.12 (b) and zoomed-in (c)), the condition $(\Delta f_p + \Delta f_{\text{RF}}/2) < f_{\text{rep}}/2$ is fulfilled, and the RF spectrum is indeed the down-converted alias of the optical spectra of the two comb (Figure 1.12 (a)). In the other case (Figure 1.12 (d) and zoomed-in (e)), there is an overlapping of the RF

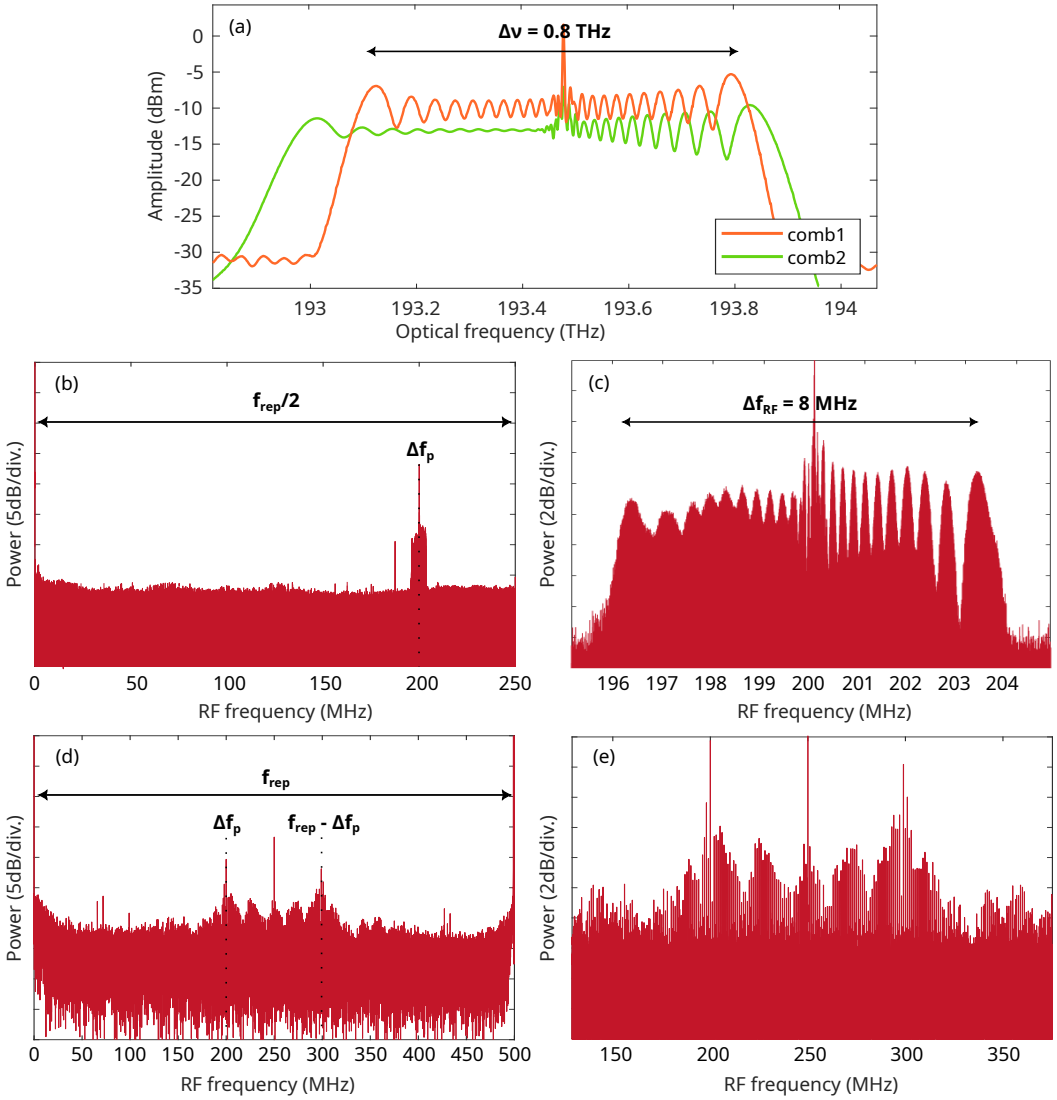

Figure 1.12: Experimental examples of operating conditions. (a) OSA spectra comb1 at f_{rep} and comb2 at $f_{\text{rep}} + \Delta f_{\text{rep}}$. The optical width is $\Delta\nu = 0.8$ THz. (b) Electrical spectrum between 0 and $f_{\text{rep}}/2$, for $f_{\text{rep}} = 500$ MHz and $\Delta f_{\text{rep}} = 5$ kHz. (c) Zoom on the area of interest, centered at $\Delta f_p = 200$ MHz and of RF bandwidth $\Delta f_{\text{RF}} = a \times \frac{\delta f_{\text{rep}}}{f_{\text{rep}}} = 8$ MHz. (d) Electrical spectrum between 0 and f_{rep}, for $f_{\text{rep}} = 500$ MHz and $\Delta f_{\text{rep}} = 1$ MHz. The RF bandwidth exceeds $\frac{f_{\text{rep}}}{2}$. (e) Zoom on the area of interest, where the contributions at $\Delta f_p = 200$ MHz and $f_{\text{rep}} - \Delta f_p = 300$ MHz overlap, leading to a poor-quality down-converted spectrum.

comb at $0 \times f_{\text{rep}} + \Delta f_p = 200$ MHz and of the RF comb at $1 \times f_{\text{rep}} - \Delta f_p = 300$ MHz. This leads to a poor-quality RF spectrum from which it is impossible to retrieve the optical spectra. These two experimental results illustrate the impact of the operating conditions of the dual-comb set-up.

In addition to the constraints imposed by signal processing, there are also conditions on the acquisition of the interferogram. In order to satisfy the Nyquist-Shannon criterion, the sampling frequency F_s must be at least $2 \times f_{\text{rep}}$. For a given acquisition time, this affects the amount of recorded data. The acquisition time and the repetition rate difference set the number of recorded interferogram periods, which defines the spectral resolution of the measurement. Therefore, the higher Δf_{rep}, the better the spectral resolution. From the various sampling and acquisition constraints, one can conclude that the choice of parameters in dual-comb interferometry is a trade-off between spectral resolution and acquisition speed, in addition with optical width and number of recorded data.

1.3.3 Dual-comb set-ups

When all the previously listed conditions are met, a dual-comb set-up can be used for absorption spectroscopy.

Configurations

The dual-comb measurement can be carried out using two different configurations. In the symmetric configuration, depicted in Figure 1.12 (a), the two frequency combs are coupled before interacting with the sample. In the asymmetric configuration, shown in Figure 1.12 (b), only one comb is sent through the cell, and then is coupled with the second comb. In both cases, the beat between the two combs is detected by a photo-detector to obtain the interferogram, as explained before.

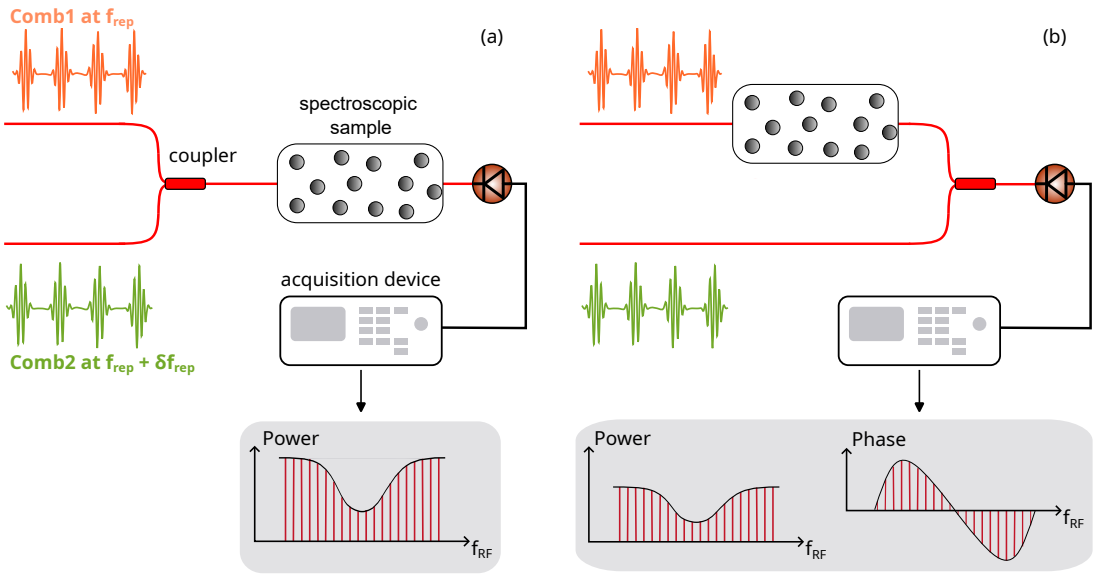

Figure 1.13: Dual-comb set-up in (a) symmetric configuration and (b) asymmetric configuration.

The retrieved spectral information depends on the configuration. In the symmetric configuration, the two combs interfere with each other before interacting with the sample. The optical path is therefore the same for both combs, and the information about the phase induced by the sample is lost. Only the effect on the amplitude, called the *absorption spectrum*, can be retrieved. In the asymmetric configuration, the second comb samples the first comb after it has interacted with the sample. It is thus possible to compute the complex spectrum, and therefore the spectral phase induced by the propagation through the sample, which is called the *dispersion spectrum*. However, the detected absorption spectrum is half as intense as in the symmetric configuration, since there is half as much optical power interacting with the sample [25]. In the following of this manuscript, the measurement set-up is in asymmetric configuration, precisely because I want to retrieve both the absorption and the dispersion spectra. My dual-comb (then tri-comb) measurements are each carried out in a waveguide that models the absorbing sample. This is a case in which it may be interesting to measure the phase, which a good indicator of the sensitivity and stability of the set-up [113–115].

Mutual coherence

Whatever the configuration, the prerequisite is the good coherence between the two combs. Such a condition means that the temporal jitter between the two pulse trains must not be higher than the optical sampling step $\Delta t = \Delta f_{rep}/f_{rep}^2$. This is necessary to obtain an electrical spectrum with resolved peaks, meaning narrower than the spacing Δf_{rep}. Broadly speaking, DCS demonstrations can be categorized into three groups: free-running combs, mutually coherent combs, and fully referenced combs, as outlined in Figure 1.14 from [20].

Demonstrations of dual-comb spectroscopy using two independent and free-running frequency combs showed that it was impossible to resolve the comb lines, limiting the resolution to tens of GHz [19, 109]. It is therefore essential to lock them with one another [45]. Additionally, the repetition frequencies and offset frequencies should remain relatively constant throughout the experiment, which is obtained by using the techniques described in Section 1.1.2. These methods have achieved excellent levels of stabilization [7, 80, 116]. However, the locking operations involve controlling the laser cavities through length, temperature, current, ect., which is often demanding in terms of space, cost and complexity [117, 118]. To get around this need for servo-control, it is possible to generate both combs from the same source. The two combs then share common noise sources, enabling good mutual coherence to be achieved in free-running conditions. The set-up is then designed so that the propagation on each arm is as similar as possible, in order to maintain the mutual coherence. This type of architecture has been applied to electro-optic combs [25, 26], microresonators [24, 119], fiber lasers [120–123], and solid-state lasers [124, 125]. It is also possible to compensate for the low coherence post-facto, using phase correction algorithms [117, 125–127]. This wide diversity of techniques to generate two coherent combs demonstrates the impact of dual-comb interferometry and the abundance of research work in this field.

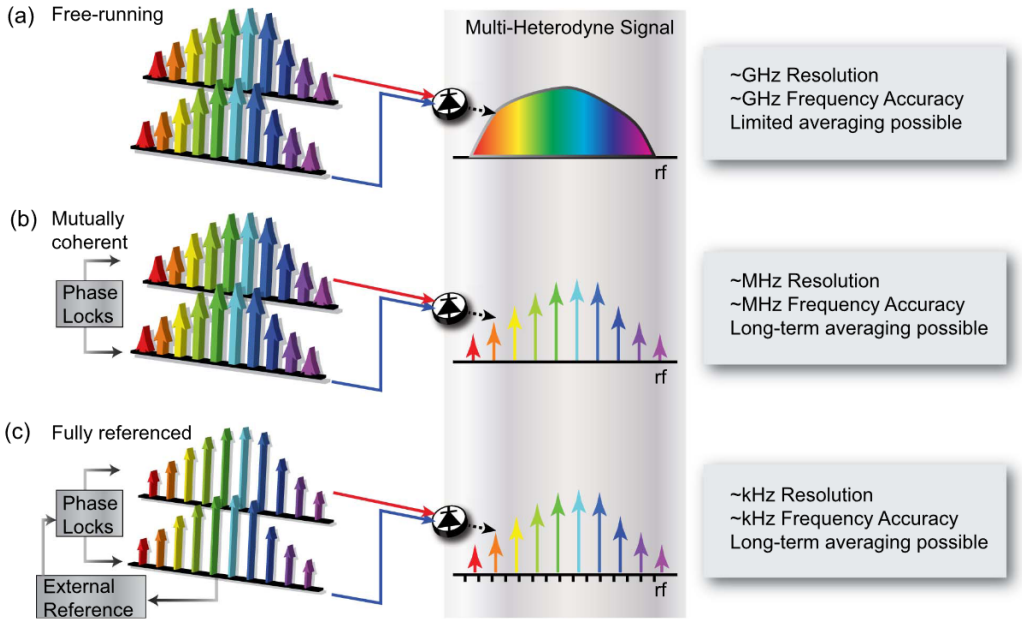

Figure 1.14: Three different categories of DCS demonstrations. (a) Free-running combs can yield dual-comb spectra, but with low resolution, low frequency accuracy, and low SNR, since only limited signal averaging is possible; (b) mutually coherent combs can yield comb-tooth-resolved spectra that can be averaged for high SNR; and (c) fully referenced combs yield spectra with simultaneous high resolution, absolute frequency accuracy, and high SNR. Text boxes indicate some general rules of thumb for frequency combs based on mode-locked lasers. From [20]

1.4 Tri-comb interferometry

Femtosecond coherence spectroscopy gathers a collection of ultrafast methods using laser pulses for creating and tracking coherent states within samples [128–130]. Within this realm of non-linear spectroscopy techniques, there has been a notable surge in the interest for Two-Dimensional Spectroscopy (2DS). The appeal of 2DS lies in its ability to observe rapid processes in real-time [22, 131–133]. This technique is extensively employed to uncover intricate aspects of ultrafast relaxation dynamics. The following discussion presents the method, and how a tri-comb system can enables the measurement of 2D spectra with high temporal and spectral resolutions. Readers can refer to bibliographic references in the field for more details [31, 134].

1.4.1 Coherent Multi-dimensional Spectroscopy

Ultrafast spectroscopy techniques have emerged to probe events at the fs time regime [135]. All these methods can be broadly classified under the umbrella of *FWM spectroscopy* [136], since it involves the non-linear interaction of three propagating light waves within a medium, leading to the generation of a fourth wave, often referred to as the 'signal'. The third-order

nonlinear response function governs the process, naturally presenting resonances specific to the medium. These resonances can be probed through the enhancement of the FWM output, leading to insightful characterization of the medium's properties. Within this overarching category, a range of techniques can be categorized based on factors such as the excitation geometry, time and frequency characteristics of the exciting waves, and detection set-ups.

General presentation

Multidimensional Coherent Spectroscopy (MDCS) constitutes an extension of the FWM techniques, drawing parallels with conventional 1D spectroscopies like photon echo [137] and pump-probe [138]. However, MDCS takes a leap by enabling the decomposition of complex spectra across multiple time or frequency coordinates in 2D. Originating in the 1960s, this approach found its genesis in nuclear magnetic resonance (NMR) spectroscopy [139]. The beauty of 2D spectroscopy lies in its capacity to define couplings between distinct states or transitions as cross-peaks. These cross-peaks emerge far from the diagonal zone, and are an unequivocal evidence of state interactions and couplings. These interactions are exclusively discernible within multidimensional techniques. Moreover, the temporal evolution of the cross-peaks can be tracked, providing insights into coupling strength and associated dynamics.

How to built the 2D map

In 2DS, a sequence of three short pulses interacts with the sample under study. It causes the stimulation of a $\chi^{(3)}$ response. In order to apprehend what happens, let's compare it with the pump-probe technique. In a standard pump-probe experiment, a brief pump pulse triggers an impulsive excitation of the sample. After a delay T, a weak probe pulse detects the modification of the absorption of the sample, due to the excitation (see Figure 1.15 (a) and (b)). A typical pump-probe spectrum plots the probe transmission as a function of its frequency ω_{probe} (see Figure 1.15 (c)). In this case, the first two interactions (collectively indicated as 'pump') are simultaneous, and the two exciting beams (E_1 and E_2) propagate along the same direction. The third interaction is with the 'probe' beam (E_3). The signal (green) is emitted in the same direction as that of the probe; it is self-heterodyned by the probe and measured as a function of the delay time T between the pump and probe beams. In 2DS experiments (see Figure 1.15 (e)), the three fields interacting with the sample (E_1, E_2, and E_3) and a fourth beam used only for detection purposes are arranged in a square. The LO is aligned in the same direction as the emitted signal (defined by phase-matching conditions) so that the measured quantity indeed results from the interference between the signal and the LO (heterodyne detection). In a 2D spectrum (see Figure 1.15 (f)), the third-order signal is displayed along two frequency axes, ω_1 and ω_3, obtained by Fourier transforming the delay times t_1 and t_3. The axis ω_3, often denoted as the 'emission' frequency, mirrors the ω_{probe} axis in the pump-probe response. The new frequency axis ω_1, known as the 'excitation' frequency, can be conceived as a distribution of frequencies excited by the pump pulse. The evolution of the 2D (ω_1, ω_3) maps is followed along t_2.

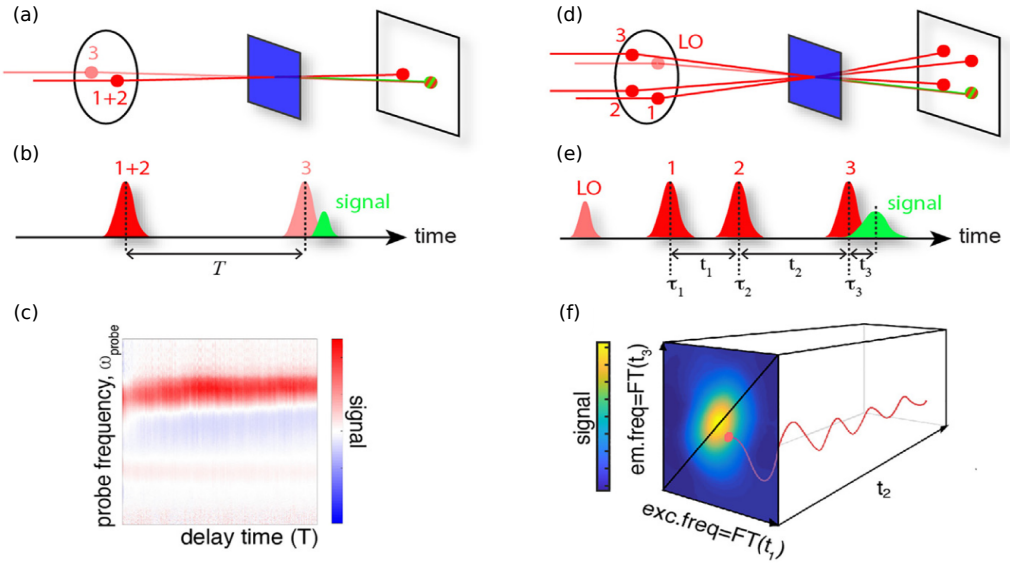

Figure 1.15: Excitation geometry for (a) pump-probe and (d) 2DS experiments. The associated pulse sequence and time delay definition is reported in (b) and (e) respectively. (c) Example of a typical plot ω_{probe} vs. T obtained as a result of a pump-probe experiment. (f) Pictorial representation of the matrix dataset obtained with a 2DS experiment. From [134]. 2DS = two dimension spectroscopy; LO = local oscillator.

It would be possible to enhance the excitation axis resolution by iteratively conducting a pump-probe experiment, scanning a singular narrowband pump pulse in frequency. However, this approach sacrifices time resolution. A trade-off thus arises between excitation axis resolution and the requisite time resolution for studying ultrafast relaxation dynamics. This challenge is circumvented by acquiring the excitation axis in the time domain while altering the delay t_1 between the first two interactions (see Figure 1.15 (d) and (e)). The ensuing signal oscillates as a function of delay time t_1, enabling the recovery of the excitation frequency axis via FT, akin to conventional FTIR spectroscopy [109]. This outcome exhibits both high temporal and spectral resolution.

Third-order signal

Figure 1.15 (f) depicts the collected signal within a 2D spectroscopy map. The following discussion presents the outlines of the 2D representation. As any FWM signal, the third order signal is proportional to the third-order polarization $P^{(3)}$ [88]. Using the perturbative approach [135, 140], $P^{(3)}$ can be formulated as the convolution of the nonlinear response function $R^{(3)}(t_1, t_2, t_3)$ with the three fields $E_j(k_j, t_j)$. This enables to write [134]:

$$P^{(3)}(t_1,t_2,t_3) = \int_0^\infty \int_0^\infty \int_0^\infty R^{(3)}(t-t_1,t-t_2,t-t_3) \times E_1(t_1)E_2(t_2)E_3(t_3) \times dt_1 dt_2 dt_3 \qquad (1.54)$$

The times t_1, t_2, and t_3 denote the interaction times with the fields, as illustrated in Figure 1.15 (b). It is then possible to decompose the nonlinear response function as a sum of elementary states, each of which corresponding to a specific evolution of the system. Indeed, $R^{(3)}$ is the fundamental quantity that contains all the relevant microscopic information of the FWM [141]. Each specific sequence of three successive interaction with the total electric fields can be associated with a specific time evolution. The 2D map is therefore the superposition of all these elementary contributions, which generate a signal at a specific (ω_1, ω_3) coordinate. Figure 1.16 sums up the process to understand the 2D map as the representation of the different pathways of the FWM interaction.

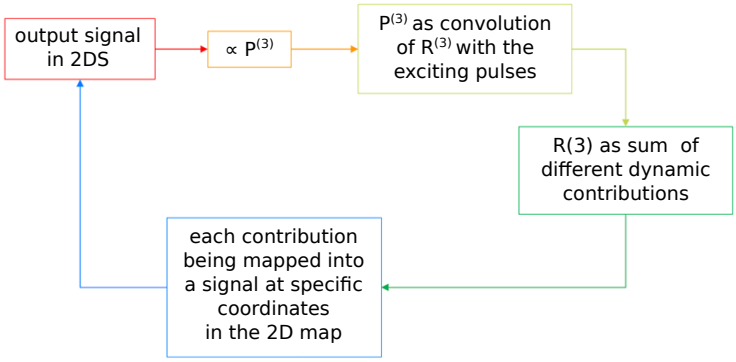

Figure 1.16: How to map the third-order signal. From the presentation of Elisabetta Collini at Femto-UP 2020.

While this multitude of contributions can make the interpretation of the 2D signal somewhat complex, it is possible to draw from this perturbative approach a few broad rules for reading the diagram. The general ones are listed below:

- signals appearing on the diagonal provide information on the excited states of the system
- the shape of these diagonal peaks depends on the interactions with the environment and broadening mechanisms
- cross-diagonal peaks appear anytime two levels are coupled and share a common ground state
- the position of these cross-peaks provide information on which states are interacting

Based on these reading rules, Figure 1.17 illustrates four examples of interaction between states that can be deduced from a 2D diagram. That offers a glimpse on the enormous potential and

versatility of 2D spectroscopy techniques.

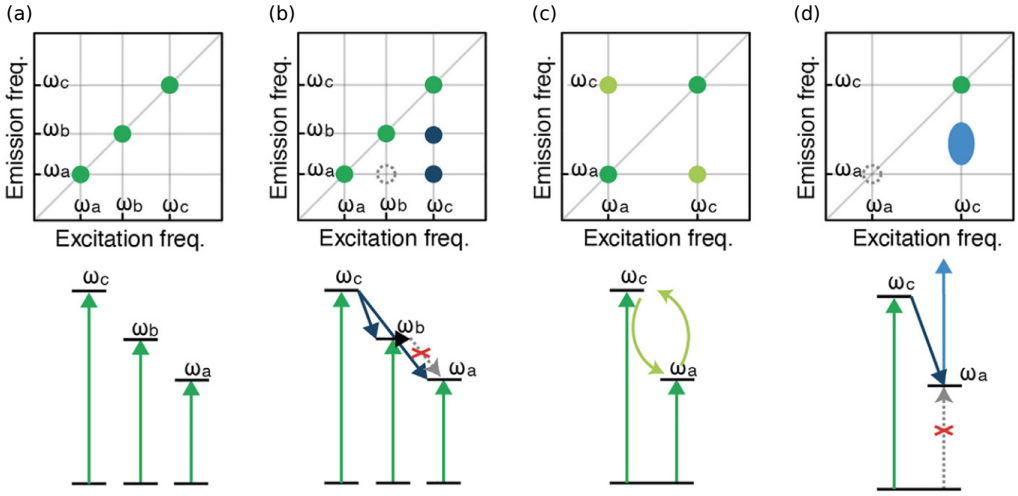

Figure 1.17: The position of the cross-peaks can be used to identify which states are interacting. (a) A system that produces multiple diagonal peaks but no cross-peaks can be modeled as a set of isolated non-interacting two-level systems. (b) The cross-peaks at coordinates (ω_c, ω_b) and (ω_c, ω_a) appearing at $t_2 > 0$ indicate that state c is coupled via energy transfer with states a and b. No coupling exists between states a and b because no cross peak appears at (ω_b, ω_a). (c) In the presence of resonance interactions between two states, cross-peaks appear already at $t_2 = 0$: the system can be modeled as a molecular dimer. (d) A dark state (ω_a) can be characterized by the coupling with a bright state (ω_c) in excited state absorption (ESA) processes. From [134].

1.4.2 2D spectroscopy with frequency combs

The preceding paragraph highlighted MDCS as a robust nonlinear method capable of untangling homogeneous and inhomogeneous linewidths, probing subtle many-body interactions, and offering valuable insights into resonance interactions [31]. However, the implementation of this technique requires the use of three coherent pulsed lasers, arranged in a configuration that ensures their phase matching. A fourth pulse is used as LO in order to retrieve the phase information from the interference pattern with the signal. [142]. Time delay regulation is also mandatory to be able to scan t_1, t_2 and t_3. That leads to complex and bulky experimental setups. The mechanical moving components to scan the delay between the pulses limit the spectral resolution and the acquisition speed [143–145].

Recent advancements have seen the integration of frequency combs into pump–probe spectroscopy and MDCS [146, 147], offering notable enhancements in resolution and acquisition speed. However, these experiments rely on a dual-comb method to detect the signal. Dual-comb interferometry is a linear technique where only one variable can be scanned at the time. That means that the time delay between excitation pulses still relies on moving mechanical stages.

To fully exploit the advantages of spectroscopy with combs, a third comb can be added to the system, offering a new dimension to the measurement. This has been applied to time-resolved impulsive stimulated Raman spectroscopy [29] to investigate the structural changes of photo-excited molecules. Another major demonstration of non-linear interferometry using three combs has been made by Lombsadze, Smith and Cundiff [28], for MDCS. They achieved measurement times under 1 second, with a comb-level resolution and no need for mechanical moving components. The principle of this experiment is to use two combs as pumps to generate the non-linear response in a medium to be characterized. A third comb then acts as LO to sample the resulting signal, employing a Vernier effect similar to dual-comb interferometry. This setup is schematically illustrated in Figure 1.18.

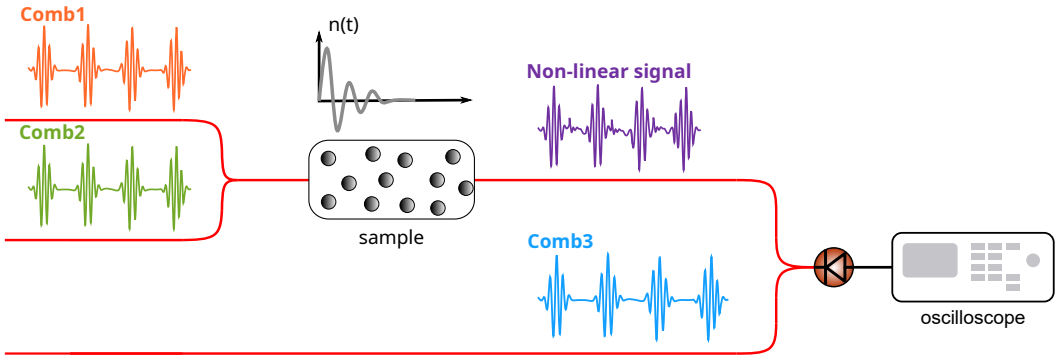

Figure 1.18: Scheme of non-linear spectroscopy using three combs. Two combs (orange and green) are used as pumps to generate a non-linear response from a spectroscopic sample. This interaction modulates the refractive index of the material, that gets inprinted in the output train of pulse. This non-linear signal is sampled by the third comb (blue) and the multi-heterodyne beat signal is detected by a photo-diode, and then recorded.

In this configuration, what is studied is the degenerate FWM between the two pumps, and the response of the medium is instantaneous. One can therefore acknowledge the differences in assembly with Figure 1.15, in particular the number of sources used and the variables measured. Let us elaborate on the example of FWM to illustrate the principle of tri-comb spectroscopy through numerical simulations in a simple case. Two Gaussian-envelope frequency combs with the same repetition frequency $f_{\text{rep}} = 1.25$ GHz but with a carrier offset of $\Delta f_p = f_{p,2} - f_{p,1} = 100$ MHz are used as pumps. The input spectrum thus consists of several packets separated of f_{rep}, which each packets composed of two lines separated of Δf_p. The FWM process (Figure 1.19 (a)) is simulated by numerically integrating the non-linear Schrödinger equation in a non-linear fiber (parameter given in the figure's legend), that mimics the sample. Each combination of pump lines at $f_{i,1}$ and $f_{i,2}$ generates side-bands at $2f_{i,1} - f_{i,2}$ and $2f_{i,2} - f_{i,1}$, as shown in zoom-in Figure 1.19 (b). Since the carrier offset is smaller than the repetition frequency, the new non-linear components are intermingled in the pump spectra. This phenomenon, that we call *intra-envelope FWM*, will be studied in greater depths in Chapter 4. The frequency shifts between each line are

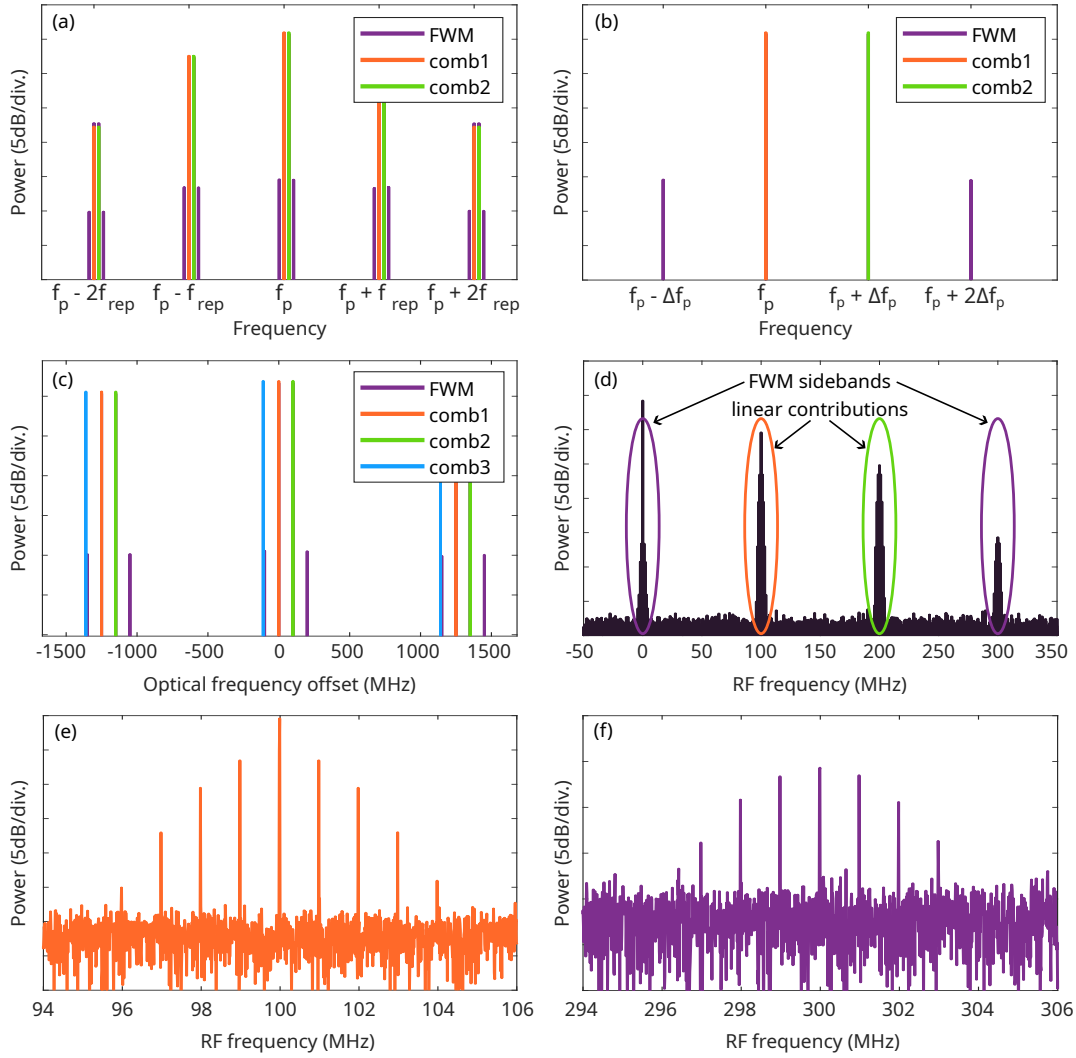

Figure 1.19: Numerical simulations of tri-comb interferometry for FWM spectroscopy. (a) Optical spectra of comb1 (orange) and comb2 (green) at f_{rep} that generate FWM sidebands (purple). The fiber has a length of L = 50 m, a dispersion parameter $\beta_2 = 1$ ps^2/km, and a non-linear coefficient $\gamma = 1$ /W/km. (b) Zoom on the central spectral packets that shows the frequency shift of Δf_p between each line. (c) Optical spectrum of the FWM of comb1 and comb2, coupled with comb3 (blue), at $f_{\text{rep}} + \Delta f_{\text{rep}}$, used as local oscillator. (d) Associated electrical spectrum. The multi-heterodyne beating down converts the optical spectrum in the RF domain. Each contribution is isolated in a spectral packet centered at its difference of carrier frequency with the LO. (e) RF linear contribution of comb1 beating with comb3, centered at 100 MHz. (f) RF non-linear contribution of blue-shifted FWM sideband beating with comb3, centered at 300 MHz.

too small to be individually resolved by standard characterization tools. This is why a third comb is used as local oscillator, as depicted in Figure 1.19 (c). It has a different repetition frequency

f_{rep3} = 1.251 GHz and an offset frequency with comb2 of $\Delta f_p' + \Delta f_p = f_{p,2} - f_{p,3}$ = 200 MHz. Each line of the FWM spectrum beats with the closest line of the oscillator, and this interference down-converts the spectrum to the RF domain, similarly to dual-comb interferometry. In Figure 1.19 (c), the blue lines of the LO and the low-frequency lines from the FWM are slightly shifted, so that they can be distinguished. In practice, they overlap.

Figure 1.19 (e) shows the associated electrical spectrum. The main difference from the dual-comb RF spectrum is that there are no longer one, but four spectral packets. Since comb1, comb2, and the FWM sidebands each have specific carrier offsets with respect to the local oscillator, each group of beating lines is centered at a specific frequency: at 100 MHz, the linear beat between the LO and comb1; at 200 MHz, the linear beat between the LO and comb2; at 0 MHz, the beat between the LO and the low frequencies of the FWM; at 300 MHz, the beat between the LO and the high frequencies of the FWM. The multi-heterodyne beating thus separates the linear contributions from the contributions originating from FWM. The peak at 0 MHz also emerges from all the continuous contributions of the beating, and the peak at 100 MHz results from the linear interaction between comb1 and comb2. The comb-like structure of the optical sources is maintained in both the linear contributions (as shown in the zoom-in of Figure 1.19 (e)) and the nonlinear contributions (as shown in the zoom-in of Figure 1.19 (f)). That shows that tri-comb interferometry achieves a high spectral resolution. It also enables to individually study the new components generated by non-linear effects. One can conclude that not only the multi-heterodyne beating replaces high-resolution spectrometers by a simple PD, but also produces a highly selective spectral filtering.

1.4.3 Other applications

A tri-comb set-up can also be used to double-heterodyne a signal to characterize, in order to avoid the ambiguity in determining the relative position between the beat signal and comb teeth. By accessing different repetition rates, there are no missing frequency points or dead zones in the measurement range [33]. Within the same idea, it also can ensures a comprehensive and continuous characterization of micro-wave signals [148]. In both those examples, tri-comb interferometry also enhances the measurement's resolution for the same acquisition speed. In a patent registred by ONERA and CNES [149], a two-comb set-up is combined with a third comb used as LO for LIDAR measurements using dual heterodyne detection to improve the quality of the signal received at long range, for atmospheric spectroscopy applications.

To conclude, adding a third comb to the system can overcome some limitations of DCS, such as ambiguities arising from the mode-beating process or the trade-off between resolution and acquisition speed. Tri-comb interferometry enables more flexible configurations for complex measurements and provides the means for the simultaneous acquisition of different physical quantities.

1.4.4 Experimental set-up for tri-comb generation

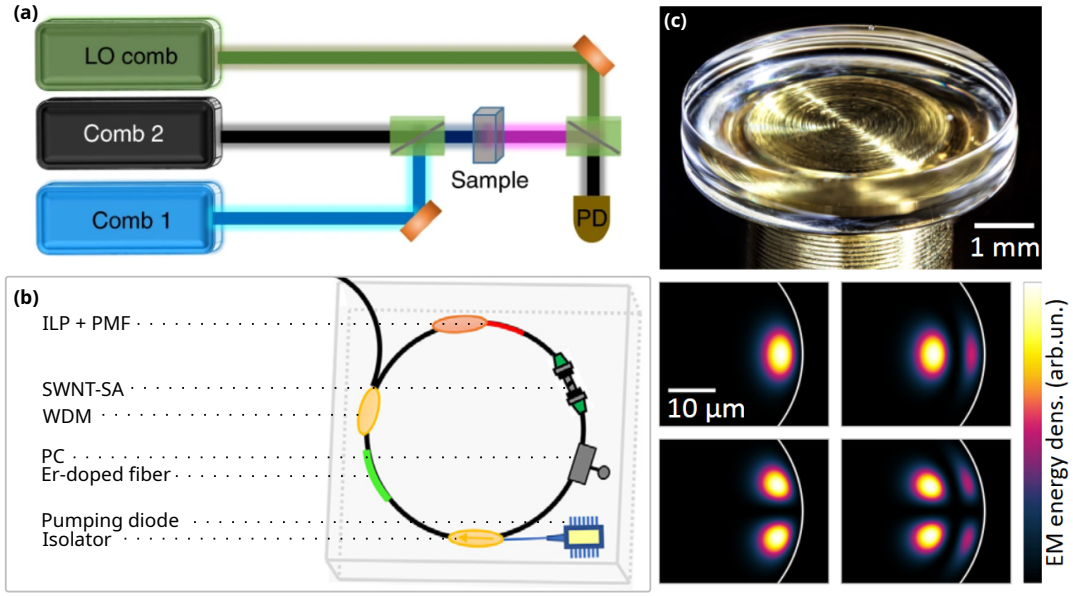

Figure 1.20: Examples of coherent tri-comb architectures. (a) Locking of three mode-locked lasers from [28]. (b) Wavelength and polarisation multiplexing in a fiber cavity from [150]. ILP = In line polariser, PMF = polarisation maintaining fiber, SWNT-SA = single-wall carbon nanotube saturable absorbant, WDM = wavelength demultiplexer, PC = polarisation controller. (c) Spatial multiplexing in a micro-resonator from [34].

Once again, the essential condition for the interference between multiple combs is their good mutual coherence. Tri-comb interferometry is even more demanding in this regard than two-comb systems, and the state-of-the-art in non-linear spectroscopy is the locking of three mode-locked lasers [28, 29, 151]. As explained in Section 1.3.3, these operations result in complex, expensive, and bulky set-ups. Clever architectures have been proposed to generate three highly mutually coherent combs under free-running conditions, resorting to wavelength and polarization multiplexing [33, 152, 153] in laser cavities or spatial multiplexing in micro-resonators [34]. The idea behind these set-ups is to generate the three combs from a common source and to make them propagate as identically as possible, so that they experience similar phase noise that are cancelled through interfering. In conclusion, the existing architectures for tri-comb systems rely either on the need for a complex servo-control, or on the use of cavities, some examples of which are presented in Figure 1.20. In these cavity-based solutions, the pulse repetition frequency is set by the cavity modes, and the frequency offset arises from the influence of certain phenomena on the effective index, such as polarization or dispersion. As a result, the degree of freedom in parameter choices is limited. There is therefore a need for a technological solution giving acces to three coherent frequency combs, that offers tunability and ease of implementation.

1.5 Conclusion

In this chapter, we have looked at the fundamentals of frequency comb, their applications, as well as the experimental set-ups for generating them. We shed light on the popular technique that is electro-optic modulation, that offers a great tunability of the parameters of the comb. We then introduced the basics of pulse propagation in optical fibers. We have seen that various physical phenomena exist, in particular the phenomenon of SPM that can be used to coherently broaden the spectrum of a frequency comb. We then presented the basics of dual-comb and tri-comb interferometry, which are the applications aimed for the set-up developed in this thesis's work.

Chapter 2

Presentation of the multi-comb system

Outline of the current chapter

In order to provide for a tunable coherent multi-comb platform, we aimed to develop a solution based on electro-optic modulation. The main inconvenient is that electro-optic combs have a narrow spectral bandwidth, which is a major drawback for some spectroscopic applications. Therefore, it is necessary to broaden the pulse spectra through coherent nonlinear effects, such as SPM. To preserve the mutual coherence, the broadening of the three sources can be achieved by multiplexing them within a single structure. This idea was applied to a dual-comb system counter-propagating in an optical fiber, developed by Guy Milllot and al. in 2016 [26]. The two sources have similar optical paths, and the degradation caused by fiber propagation cancels out when the two frequency combs interfere. However, because an optical fiber has only two propagation directions, the architecture remains limited to dual-comb generation. The solution we offer is the spatial multiplexing of three combs from EOM in a tri-core non-linear fiber.

In this chapter, we present an experimental setup based on these concepts, as well as the characterization of each comb. The work carried out on Menlosystem's commercial C-combs, available at ONERA (DPHY, SLM) serves as a point of comparison to support the discussion. In this chapter, as in the rest of this manuscript, all the results presented are the fruit of my personal work, unless explicitly stated otherwise.

2.1 Experimental set-up

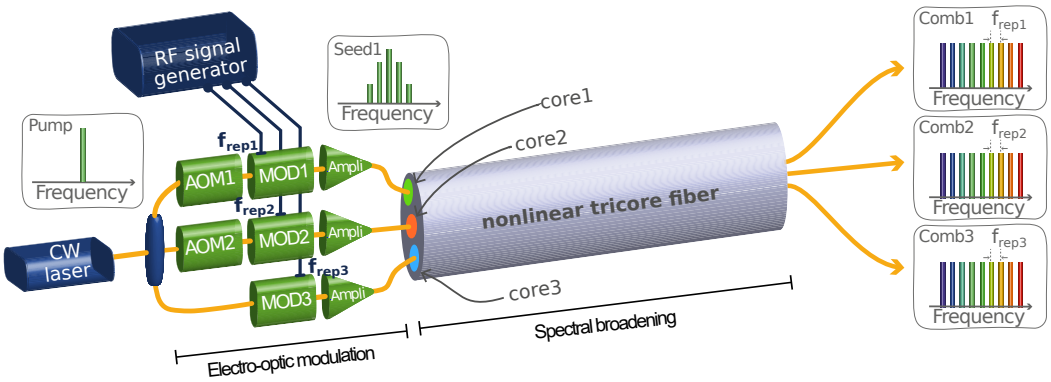

Figure 2.1: Simplified sketch of the experimental setup. CW = continuous-wave; AOM = acousto-optic modulator; MOD = intensity modulation; Ampl = optical amplification; RF = radio-frequency.

As mentioned earlier, the set-up we assembled is composed of two stages: first the electro-optic modulation and then the spectral broadening in the multi-core fiber, presented in the general scheme in Figure 2.1. I arrived in Lille at the start of my second year of thesis, and took over from Etienne Genier, then a post-doc. I added a third functional channel, and adapted the two pre-existing channels to optimise the SPM-induced spectrum of the three combs.

2.1.1 Prefiber set-up: EOM combs

General description

Figure 2.2 details the optical set-up. An ultra-narrow CW laser (Koheras Basik) centered at 1550 nm delivering 40 mW is amplified up to 500 mW before being split into three channels with a set of couplers. AOMs are inserted in the first two channels to have different carrier frequencies on each channel. The shift are respectively $f_{\mathrm{AOM1}} = 100$ MHz and $f_{\mathrm{AOM2}} = 200$ MHz. These AOMs induce optical losses and therefore a certain power asymmetry on the three paths. To pre-compensate for this effect, the continuous laser is divided asymmetrically, as shown in Figure 2.2.

On the three channels, the continuous waves are transformed into pulse trains using intensity

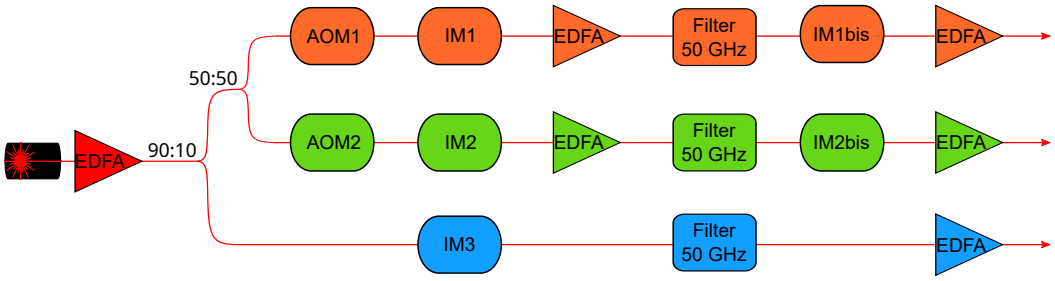

Figure 2.2: Scheme of the optical set-up. AOM = acousto-optic modulator; IM = intensity modulators; EDFA = Erbium-doped fiber amplifier.

modulators (iXBlue MXER-LN). The signal is then amplified and the amplified stimulated emission (ASE) in excess is removed by using a spectral filter. A second intensity modulator is used to increase the extinction ratio between the pulses to reach about 50 dB. This helps removing the central component in the spectrum, corresponding to the CW background between the pulses.

These intensity modulators are driven by RF signals (Fig.2.3 (a) and (b)) generated with three different Arbitrary Waveform Generators (AWG). Thank to those, each repetition rate can be tuned from 100 MHz to 10 GHz, which is the maximum of the BW of the IM. Repetition frequencies lower than 100 MHz can be achieved by adapting the set-up to the peak power required to obtain a good SPM spectrum. The experiments in this manuscript have been performed at 500 MHz and at 1.25 GHz, depending on the required RF bandwidth (limited at $f_{rep}/2$). The pulses have a FWHM of 55 ps. The AWGs generate a RF signal from a bits vector, which enables to tune the temporal width. At the input of each IM, there are amplifiers to enhance the RF power and minimize the optical losses introduced by the modulation. A example of these pulse trains at the output of the second IM, measured with an Optical Sampling Oscilloscope (OSO) of 700 GHz bandwidth is depicted in Figure 2.3 (c) and (d).To conform to the minimum limit of the bandwidth of the OSO, the repetition frequency is set at f_{rep} = 1.25 GHz. We assume this pulse pattern to be similar at all repetition frequencies. A typical optical spectrum is shown in Figure 2.3 (e) and (f). It is a narrow frequency comb with about 100 teeth, separated by the repetition rate (set at 500 MHz), with a high SNR of 50 dB at maximum.

Difference of repetition rates

On each channel, one AWG drives all the RF inputs (IMs and optional AOM), as presented in Figure 2.4 (b). Using AWGs to generate RF pulses gives the advantages of tunability and ease of use. However, the sampling rate is limited (25GHz / 50GHz depending on the model) and its resolution (+/- 100 MHz) does not allow much margin of choice on the difference of repetition frequencies δf_{rep}. To overcome this limitation, we use a Power Signal Generator (PSG) - Keysight E8257D (Fig.2.4 (c)) as follows: two of the AWGs share its 10 MHz reference; the signal output of this PSG is used as a clock for the third AWG in order to finely tune its repetition

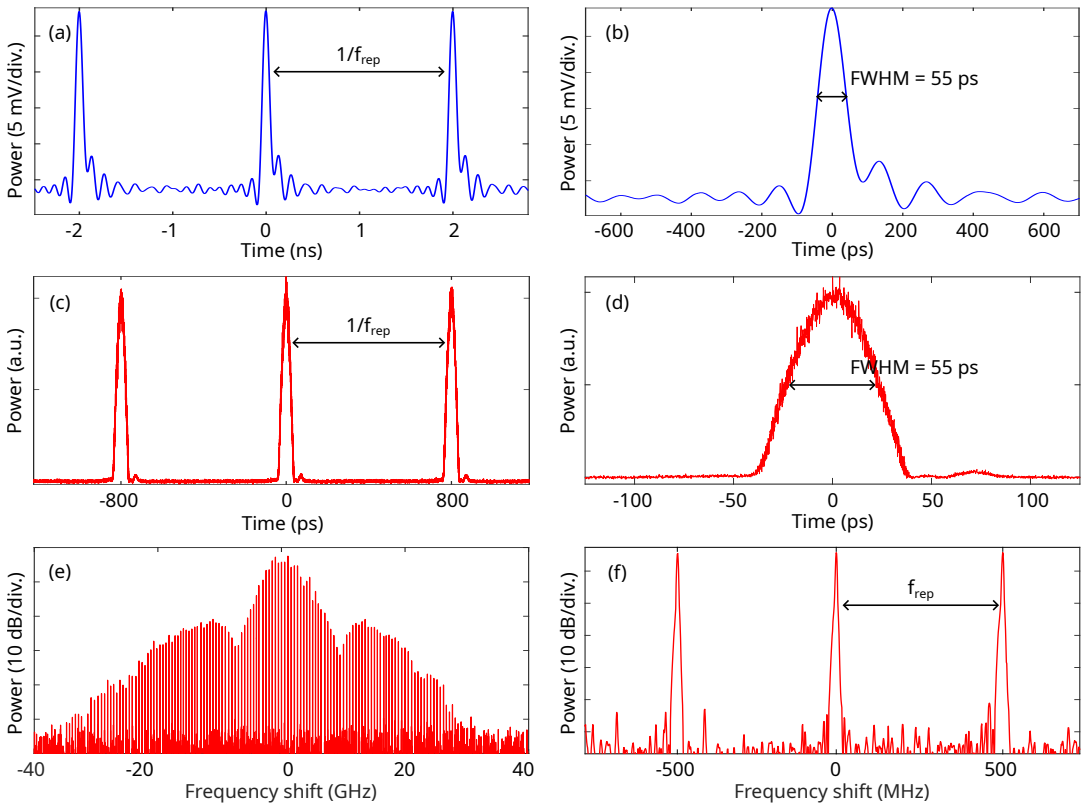

Figure 2.3: Characteristics of one eo-comb. (a) RF pulses from the AWG driving the two IMs at f_{rep} = 500 MHz. (b) Zoom on one pulse. (c) Optical pulses at the output of the EOM stage at f_{rep} = 1.25 GHz. (d) Zoom on one pulse. (e) High-resolution spectrum of the pulse train at f_{rep} = 500 MHz. (f) Zoom on three peaks. RF = radio-frequency; AWG = Arbitrary Waveform Generator; IM = intensity modulator; EOM = electro-optic modulation.

rate. The PSG signal frequency $f_{clock,\,PSG}$ is slightly shifted compared to the actual AWG clock frequency $f_{clock,\,AWG}$, which leads to the actual repetition rate $f_{rep}' = f_{rep} + \delta f_{rep}$ to be slightly shifted compared to the theoretical repetition rate: $\delta f_{rep} = f_{rep} \times (1 - f_{clock,\,PSG}/f_{clock,\,AWG})$. This is a way to ensure that the three AWGs share a common reference while being able to tune the repetition rate as freely as possible. The inputs are commutable and the repetition rate can be independently changed on each channel. However, this configuration is not optimal in terms of relative stability between the three EOM channels, and therefore it is an avenue for improvement that will be discussed in the perspective section of this manuscript.

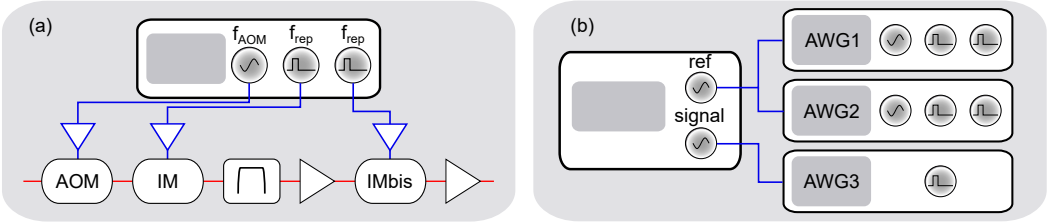

Figure 2.4: RF set-up. (a) RF driver scheme for one channel. For CH1 and CH2, an AWG drives the AOM and the two IMs. For CH3, the AWG drives only one IM. (b) Global RF driver scheme. The three AWGs are connected to a common PSG, used as a reference for two channels, and as a clock for the third channel. AWG = arbitrary waveform generator; PSG = power signal generator.

2.1.2 Spectral broadening in the multi-core fiber

General description

The three eo-combs are injected in the tri-core fiber with the help of a fan-in 3x1 that connects the three input SMF to each corresponding core of the non-linear fiber. The eo-comb spectra are broaden through Self-Phase Modulation (SPM) during their propagation in the fiber. The fiber was designed to be in the normal dispersion regime at 1550 nm, in order to avoid the amplification of ASE or input noise due to modulation instability. It also prevents the formation of solitonic effects known to affect the stability of the frequency combs. Normal dispersion regime makes generated broadened spectra more coherent, similarly to all normal dispersion (ANDI) supercontinuum [87, 154]. The three cores are spaced 30 µm apart, as shown in Figure 2.5. This distance has to be relatively small to ensure that propagation is as similar as possible in all three channels. However, the cores must be sufficiently apart to limit the cross-talk between them (as well as not being too constraining for the junction with the fans in/out). This will be studied in section 2.2.1 of this chapter. The fiber is 1 km long, the linear loss is 1 dB/km, the nonlinear coefficient is 5 /W/km and the dispersion is 5 ps^2/km at 1550nm. The cores are from the same glass preform, and have almost identical linear loss, dispersion, and non-linearity values.

The largest spectra recorded at the fiber output for each core are shown in Figure 2.6. Their widths are about 1 THz (8 nm) and they reveal a clear comb structure with more than 1500 teeth, a SNR of about 30 dB (see second row of Fig. 2.6). Note that in Figure 2.6 (c), there is a central spectral component corresponding to a continuous pump residue between pulses in the temporal domain. It arises from the lower extinction ratio of the EOM stage in Channel 3 compared to Channels 1 and 2, where a second IM has been added (see Figure 2.2 (b)).

In all channels, there is about 600 mW of input average power, which is equivalent to 21 W of peak power at f_{rep} = 500 MHz with 55 ps pulse duration. The light beam is injected within the tri-core fiber by using a commercial fan-in 3x1 (Chiralphotonics) with about 1 dB splice loss. At the fiber output, the frequency combs are demultiplexed by the mean of a fan-out 1x3 with

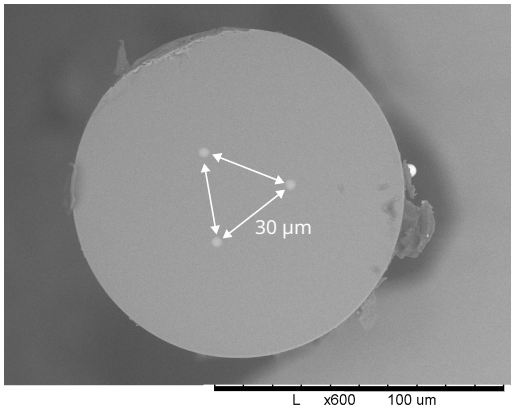

Figure 2.5: Scanning electron microscope image of the tri-core fiber.

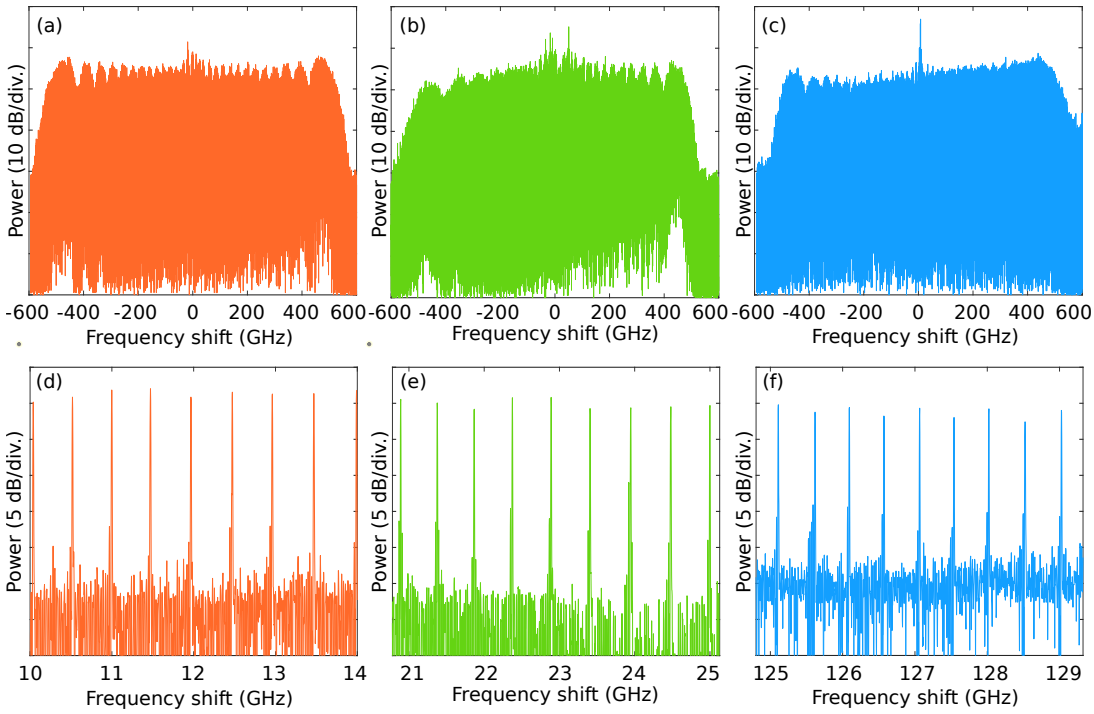

Figure 2.6: Example of broaden spectrum at the output of the tri-core fiber for (a) Channel 1, (b) Channel 2 (c) and Channel 3. The high resolution (20 MHz) enables to show the teeth structure for each comb ((d) -(f)).

about 2.5 dB splice loss for each core. The three combs are available at the output of three SMF 28 fibers. The system is PM (polarization maintaining) till the fan-in at the input of the tri-core fiber.

In Figure 2.7 (a) I recorded the evolution of the spectrum at the output of core 1 as a function of the input average power with an optical spectrum analyzer. At 19 mW of average power, the

spectrum is almost similar to the input spectrum (see Fig. 2.3) (e)). As the power increases, the spectrum broadens due to SPM [88]. With P_{in} = 650 mW, a spectral broadening of 7 nm is achieved, equivalent to almost 1 THz at 1550 nm. There is a slight peak at the center that is a residue of the CW pump. The spectrum is symmetrical and flat-top, with a SNR higher than 20 dB. Figure 2.7 (b) represents the corresponding numerical simulations by integrating the Nonlinear Schrodinger equation (NLSE) [88]. I used experimental parameters which are listed in the caption of Figure 2.7. Note that we considered the limited extinction ratio of the IM in these numerics with 50 dB. Thus, it is confirmed through these numeric simulations that the origin of the central component is indeed due to the CW background between the pulses due to the limited extinction ratio of the modulators.

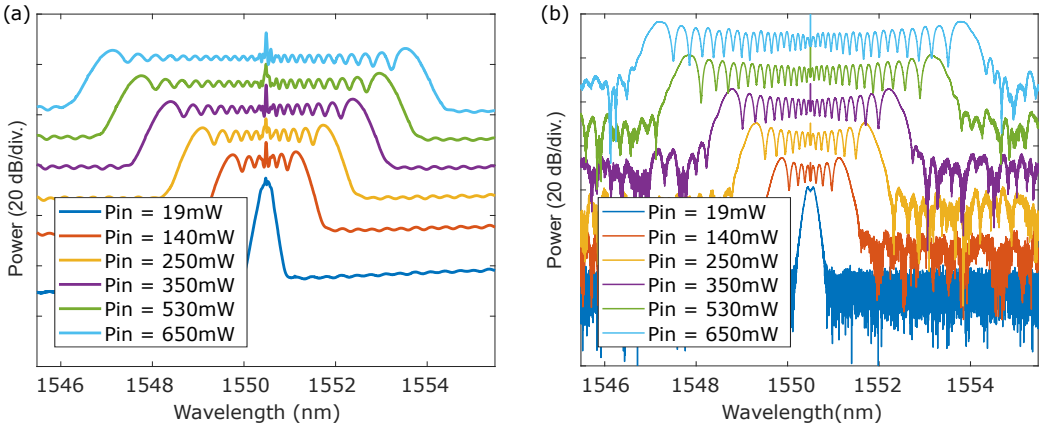

Figure 2.7: Evolution of the spectral broadening as a function of the input power. (a) Experimental recording. Example of Comb 3. (b) Numerical simulations from the NLSE. Parameters: γ = 5 $W^{-1}.km-1$, β_2 =5 ps^2/km, and α = 1 dB/km at 1550 nm, extinction ratioof the IM is 50 dB and Gaussian pulses of 55 ps duration FWHM. The average input power varies from 19 mW to 650 mW.

SPM spectrum depending on the parameter settings

What we aimed to achieve is a compromise between a wide, flat, symmetric spectrum with minimal central components, and good SNR. However, this heavily depends on the temporal envelope of the input pulses, strongly influenced by three main parameters, being:

- The bias voltage V applied to the intensity modulators sets the operating point. In our case, we aim to set it to -V_π to extinguish the continuous pump background and convert all the energy into the pulses.

- The amplitude V_{amp} of the applied electrical signal affects the pulse shape (see Appendix B.4), as well as the peak power of the pulses.

- The delay between the electrical signals driving the two intensity modulators on channels 1 and 2 also affects the pulse shape and power.

As a preliminary step, the eocomb pulses are monitored with a photo-diode and an oscilloscope for coarse adjustments. Once we have pulses with sufficient peak power to use the EDFA at the fiber's input, we adjust the parameters based on the shape of the output SPM spectrum.

We noticed that the various parameters to be adjusted each have a distinct impact. Figure 2.8 illustrates three examples of parameter variations on the SPM spectrum, starting from good settings, shown in Figure 2.8 (a). Each experimental measurement (blue curve) is compared to a specific numerical simulation configuration (yellow curve) to understand the deviation from Figure 2.8 (a). The simulations are conducted using the split-step method [88] with the same parameters for the non-linear fiber as previously detailed (see Figure 2.7).

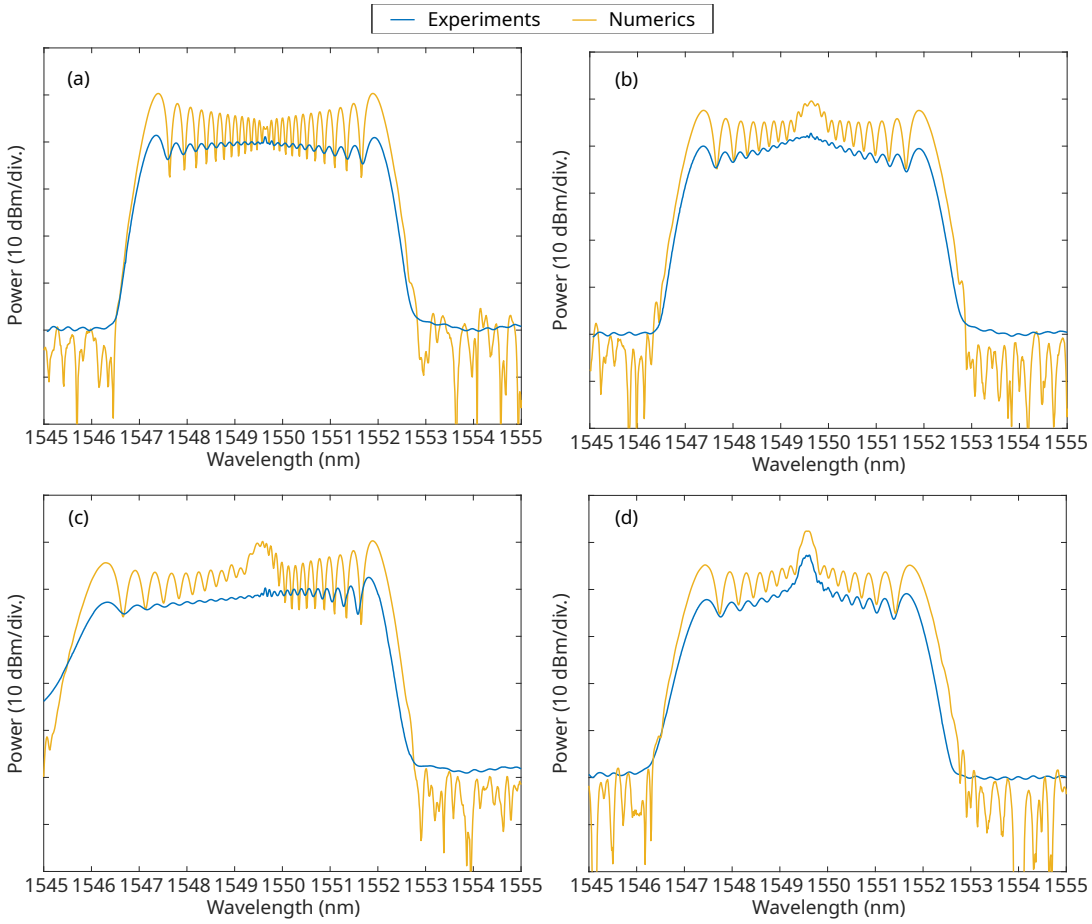

Figure 2.8: SPM spectrum depending on the parameters of the input pulses. (a) Optimal configuration. (b) Effect of RF amplification. (c) Effect of the delay between the RF pulses driving the IMs. (d) Effect of the voltage bias.

In configuration (a), we deal with SPM of a 50 ps Gaussian pulse with an average power of

350 mW at a repetition rate of 500 MHz and an extinction ratio of 90 dB. The number of periods of the spectrum matches in both the simulation and experimental measurements, indicating the same maximum phase shift (and thus the same peak power). There is a discrepancy in peak heights because the experimental input pulses are not precisely Gaussian [155], but this is considered a reasonable first approximation.

In configuration (b), I experimentally changed the power, denoted as V_{amp}, by increasing it by 1 V. The width and the number of periods of the spectrum remain unchanged; hence, the peak power remains nearly the same. Only the spectral envelope is modified, corresponding to a change in the temporal envelope of the input pulses [88]. This confirms that configuration (a) is a good optimum and that beyond this point, RF amplification becomes nonlinear. Numerically, this modification is simulated using a sharper function $e^{-|x|^3}$ (where x = t/τ with τ as the pulse width) rather than a gaussian [155]. The corresponding decrease in the height of the SPM spectrum lobes is observed.

In configuration (c), I experimentally changed the delay between the RF pulses from the intensity modulators by increasing it by 25 ps (for a 50 ps pulse width). This introduces asymmetry in the temporal envelope and, consequently, an asymmetry in the spectral envelope [155]. The downshifted part of the spectrum exhibits less sharp peaks, which corresponds to a faster decay of the temporal envelope at the leading edge compared to the trailing edge. Numerically, this modification is simulated by concatenating two temporal pulses: $e^{-|x|^3}$ for x < 0 and $e^{-|x|^4}$ for x > 0. This asymmetry is accompanied by an increase in peak power from 350 mW to 450 mW, with a broader spectral width for the leading edge (downshifted frequencies).

In configuration (d), I experimentally changed the bias voltage from 0.50 V (initially 2.66 V). This results in a greater proportion of the pump, but also a modification of the spectral envelope. There is also a narrower spectral width and fewer lobes, which corresponds to a lower peak power, as the electro-optic modulation does not convert all the energy from the continuous pump into the pulses. Numerically, these modifications are simulated by reducing the extinction ratio by 10 dB, decreasing the average power to 300 mW, and implementing $e^{-|x|^4}$ as the temporal envelope of the input pulses.

Thus, achieving optimal spectral broadening necessitates a careful and precise adjustment of the key parameters of the eo-comb chain. Once the experimental set-up had been developed, I characterized the generated combs individually, which is the subject of next section.

2.2 Properties of one comb

The main goal of the set-up is to generate coherent combs for multi-comb interferometry. Interferences between two and then three combs are the subjects of chapters 3 and 4. First, let's focus on describing each comb individually.

2.2.1 Independance of each comb

The technological choice of a multi-core fiber was made with the objective to broaden the three frequency combs while maintaining their coherence. A potential limitation of this architecture is the cross-talk between the cores, which would result in a degradation of the frequency comb structure at the three fiber outputs [156]. To quantify this, I recorded the OSA spectrum at the output of one core when its source channel is turned on (solid lines in Fig. 2.10). It represents the level of spectral density from the channel through its corresponding core. As a comparison, I recorded the OSA spectrum at the output of one core when its source channel is off while the two other channels are on (dash lines in Fig. 2.10). It represents the level of spectral density through the core from the two other channels, meaning the cross-talk power. Those measurements were made on the {fan-in; fiber; fan-out} system and the cross-talk contributions of the three different elements are indistinguishable.

Figure 2.10 concatenates those measurements for the three comb sources, with one colour attributed to one comb (orange for comb1, green for comb2, blue for comb3). The relative power between the three combs is due to a varying attenuation at the input to the OSA and is not what is relevant here. What is measured is the power difference between the signal (solid lines) and the cross-talk (dashed lines) at the output of each core. For the three combs, this power difference is more than 30 dB, indicating that there is minimal interaction between the three channels within the tri-core fiber. Consequently, their dynamics is assumed to behave similarly to single-core fibers, and the all-optical frequency comb formation dynamics reported in single-core fibers [157] are applicable to this tri-core fiber system.

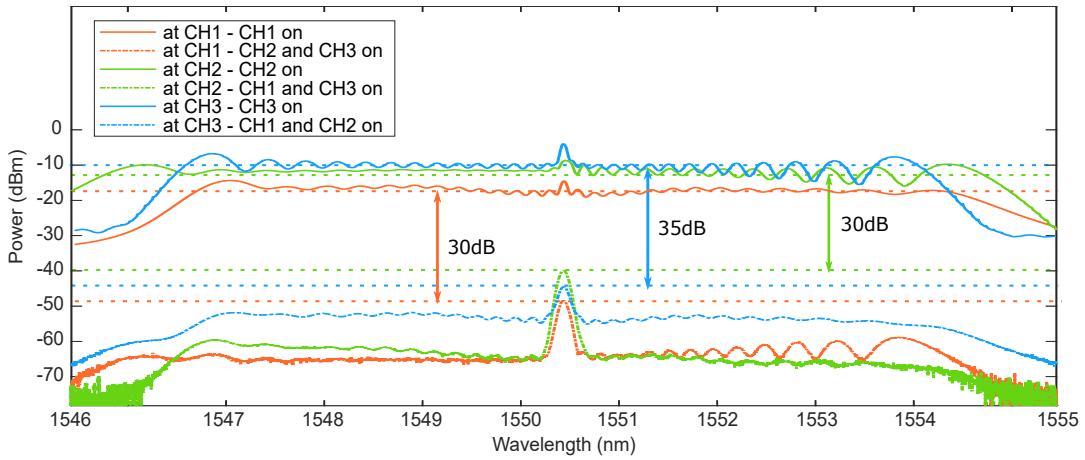

Figure 2.9: Cross-talk between the three combs. OSA spectra of the output of the tri-core fiber for Comb1 (orange), Comb2 (green) and Comb3 (blue). The full lines correspond to the output of one core when two other ones are off. The dotted lines correspond to the output of one core when the two other ones are on.

2.2.2 Temporal recompression

Post-compression is a common technique to achieve sub-ps pulses [158, 159]. The first step of this method is the SPM in the tri-core fiber, broadening the three spectra while keeping the temporal pulses almost unchanged. We assume that the dispersion during the SPM-induced broadening process is negligible since the tri-core fiber is shorter than its dispersion length (L = 1 km $\ll L_D = 10^3$ km). Secondly, a linear compression step is optimized to remove the chirp induced by SPM, reducing the temporal shape while keeping the spectral intensity constant. This step is commonly done using negatively chirped mirrors [160, 161], grating compressors [162] or fiber bragg gratings [163]. We chose to use a commercial all-fiber spatial light modulator (Waveshaper) to compress one comb via line-by-line pulse shaping [164]. If it is compressible to the bandwidth limited duration, we infer a high-degree of spectral phase stability.

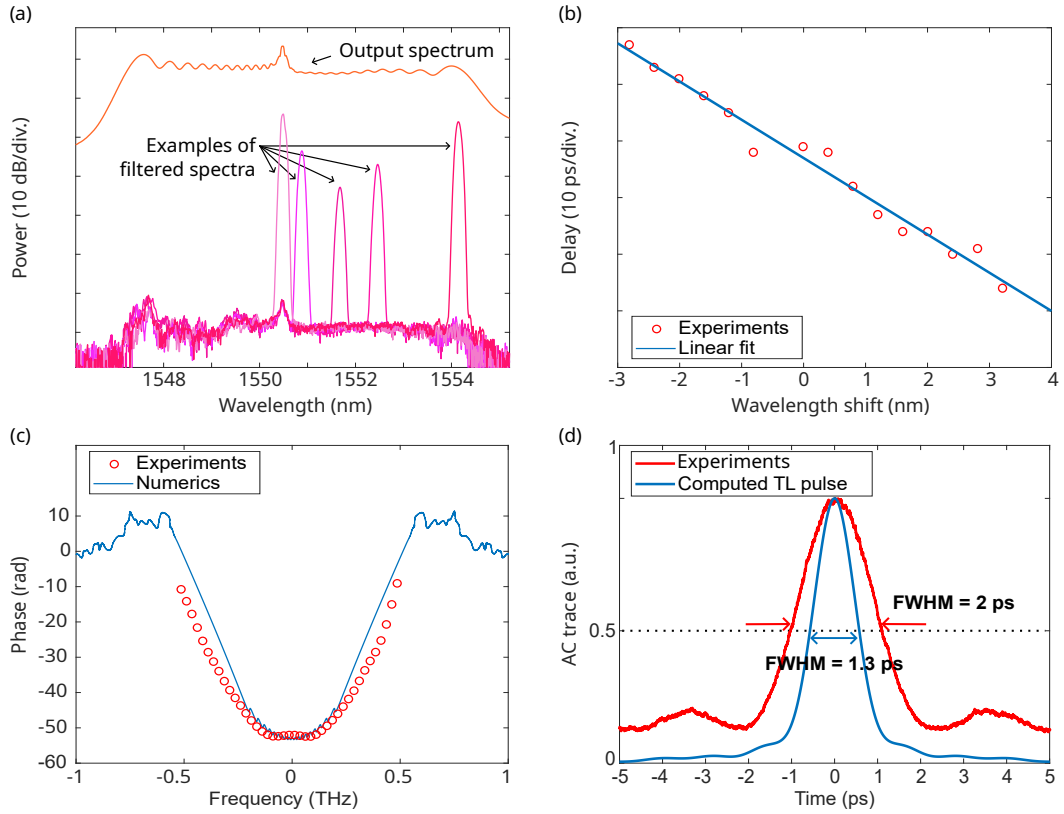

Figure 2.10: Temporal compression of the pulses at the output of CH2. (a) Examples of filtered spectra compared to the output spectrum of CH2. (b) Delay as a function of the filter wavelength shift (red circles) and corresponding linear fit (blue line) (c) Spectral phase by integration of the measured delay (red circles), and by numerical simulation (blue line). (d) AC trace of one pulse after compression, by experimental measurement (red line) and by computation of the TL pulse from the experimental spectrum. AC = auto-correlation, WS = WaveShaper, FWHM = full width at half maximum, TL = transform-limited.

Arnaud Mussot made the experiments. To do so, we first measured the chirp as follows. We used an ultra-narrow tunable pass-band filter (EXFO XTM50 - 50 GHz FWHM) to record the delay of each spectral component as a function of the central one. Figure 2.10 depicts some examples of filtered spectra (a) and the corresponding measurement of the delay (b). We used an ultra-fast oscilloscope combined with a high band-pass photo-detector (70 GHz band-pass each). We then integrated this curve to calculate the phase depicted in Figure 2.10 (c). We then used a commercial WaveShaper (Coherent 1000A) to apply the reversed-phase law to compress the pulses. Figure 2.10 (d) presents the auto-correlation (AC) trace experimentally recorded (red) after compression. It has a duration of 2 ps at FWHM. The measured AC trace is compared to the transform-limited case (blue curve in Fig.2.10 (d)), which was calculated from the measured optical spectrum while assuming a flat spectral phase. The recompression is close to the FT limit, and the slight discrepancy is mainly attributed to the limited spectral resolution of the Waveshaper (10 GHz) which avoids reproducing the small phase modulation on the bottom of the curve (blue curve in Fig. 2.10 (c)). The agreement between the measured AC trace and its TL limit demonstrates the high spectral-phase stability of the source. With this proof of concept, we reach pulses of 1 ps (assuming a Lorentzian pulse profile). Shorter durations would be easily accessible by cascading phase and intensity modulators upstream of the non-linear fiber, as discussed in the perspective section of this manuscript. Ultrashort pulses of 350 fs have be generated in a single core fiber from EOM [165], and this could be transposed in multi-core architectures.

2.3 Stability measurements of one comb

The goal of the set-up is to provide a coherent tri-comb system in a free-running configuration. Each step is designed to preserve the intrinsic mutual coherence. The intended application is interferometry, where stability relies on a low uncorrelated noise between the combs. However, it is essential to estimate the noise characteristics for each comb to quantify individual performances and gain a thorough understanding of the setup. In this section, the C-comb from Menlosystem that is available at ONERA (DPHY,SLM) is used as a state-of-the-art reference to contextualize the performance of the "home-made" frequency combs. Stability measurements will thus be carried out on both types of sources to compare them.

2.3.1 Allan variation

Tri-comb system

One first characterization is the long-term stability of the periodicity of the optical pulses. For this purpose, I measured the Allan deviation of the optical repetition rate, set at 500 MHz to fall in the bandwidth of the frequency counter (Keysight 53210A). It is the direct photo-detection of the comb, which is the equivalent to the heterodyne detection of all the modes beating with one

another. The red traces of Figure 2.11 depicts the results for the three combs. As a comparison, the Allan deviation of the repetition of the RF pulses driving the IM on each channel is also computed (blue traces).

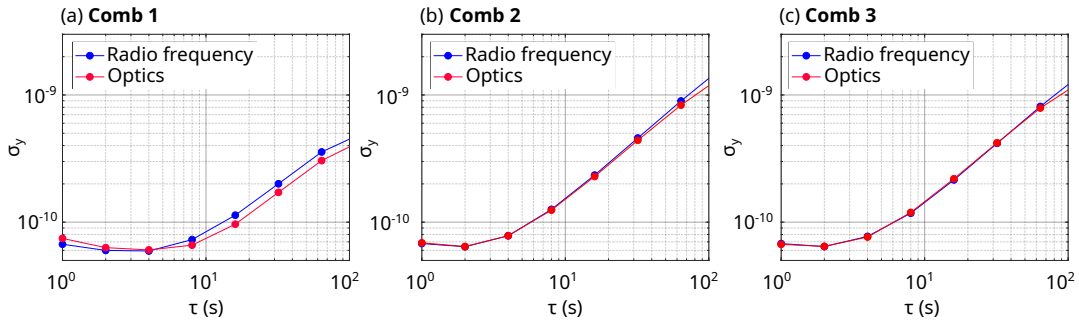

Figure 2.11: Allan deviation of f_{rep} = 500 MHz and τ = 1 s for (a) comb1 (b) comb2 and (c) comb3. The blue line is the measurement for the RF system and the red line is the measurement of the optical system.

For each comb, both RF and optical measurements highlight flicker noise up to a few seconds, then random walk frequency modulation and frequency drift up to about 100 seconds. A maximum stability plateau of $\sigma_y = 6\times10^{-11}$ is reached in the region 1 s - 10 s. All measurements are truncated at 10^2 s, a threshold value beyond which the estimated error for a 1-sigma confidence interval is too large. The measurements for the three combs exhibit the same features. There is a small gap between the measurement for Comb 1 and the two other combs. This affects the value of σ_y at τ = 100 s, but not the minimum stability floor at $\sigma_y = 6.10^{-11}$.

Menlosystem C-comb

To compare our system with the state-of-the-art, I conducted similar measurements on a commercial frequency comb, C-comb model from Menlosystem that is available at ONERA (DPHY,SLM). Details of how the system works are given in Appendix 1A. This frequency comb comes with an electronic module that allows the repetition frequency to be locked to an external clock, as described in section 1.1.2. The offset frequency, induced by residual dispersion in the fiber cavity generating the comb, remains in free-running mode. I measured the Allan variation of the repetition frequency for both commercial frequency combs available at ONERA, in the case when it is locked (configuration "locked") and when it is not (configuration "unlocked"). These measurements are presented for both commercial combs in Figure 2.12.

The two combs exhibit very similar curves. The "unlocked" configuration, where frep is in free-running mode, shows an Allan variation typical of white noise [46]. The locking effect indeed increases the stability level. The solid curve highlights flicker noise up to a few tens of seconds, then random walk frequency modulation and frequency drift up to about 10^3 seconds. A maximum stability plateau of $\sigma_y = 5\times10^{-11}$ is reached in the region 1 second - 10 seconds. The

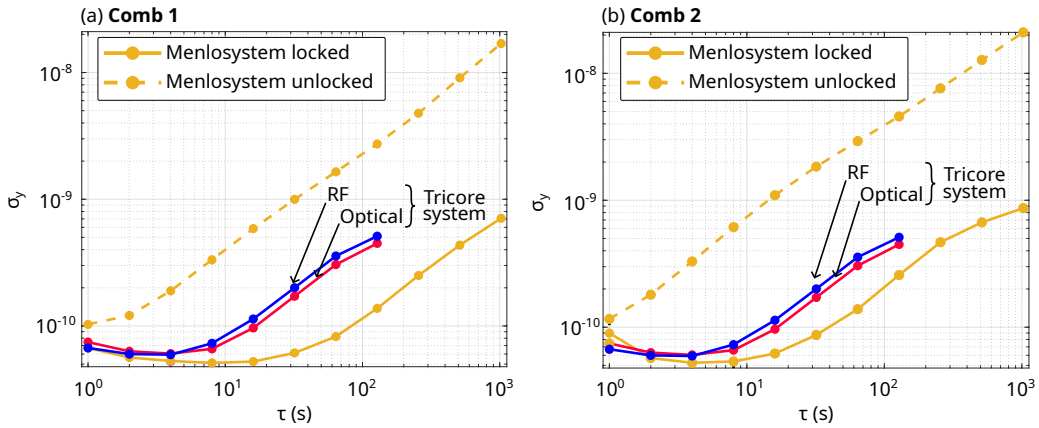

Figure 2.12: Allan deviation of the two Menlosystem combs at f_{rep} = 100 MHz and τ = 1 s. The curves of 2.11 (a) have been superposed for comparison with the Allan deviation of the tricomb system at f_{rep} = 500 MHz.

value is close to the stability of the tricore system. However, this level of stability is sustained for a longer time in the case of the locked Menlosystem comb. Our "home-made" frequency combs have a long-term stability level that lies between a frequency-locked mode-locked laser and the same pulsed laser operating in free-running mode. This suggests a good stability level for our architecture, which eliminates the need for a complex feedback system on the repetition frequency.

2.3.2 Phase noise

As a complement to the long-term measurement of Allan deviation, the measurement of phase noise indicates the rapid fluctuations of an oscillating system. As a first step, I measured the phase noise of a frequency comb directly detected by a photodiode (Thorlabs PDB480C).

The setup is schematically shown in Figure 2.13 (a). This represents the electronic spectrum of the optical comb, composed of spectral lines spaced at the repetition frequency, set at 500 MHz. The lines correspond to the interferences between all the lines in the optical spectrum. An example of the electronic spectrum is shown in Figure 2.13 (b). A zoom on the 500 MHz line (with a higher resolution) is depicted in Figure 2.13 (c). This first line represents the 1st optical mode and corresponds to the interaction between all neighboring lines. Figure 2.13 (d) shows the phase noise of the 1st RF mode derived from the AWG output signal (dark blue). In contrast, the lighter blue curve represents the phase noise of this electrical mode after amplification, which drives the intensity modulators. We observe a signal degradation with very sharp resonance peaks in the 1.10^2 - 5.10^3 Hz range and two broader peaks around 8.10^3 Hz and 1.10^5 Hz. This measurement allows us to identify amplification as having a significant impact on the purity of the RF signal. Figure 2.13 (e) displays the phase noise of the 1st optical mode. In comparison, the black curve represents the phase noise of the 1st electronic mode of the RF oscillator that drives

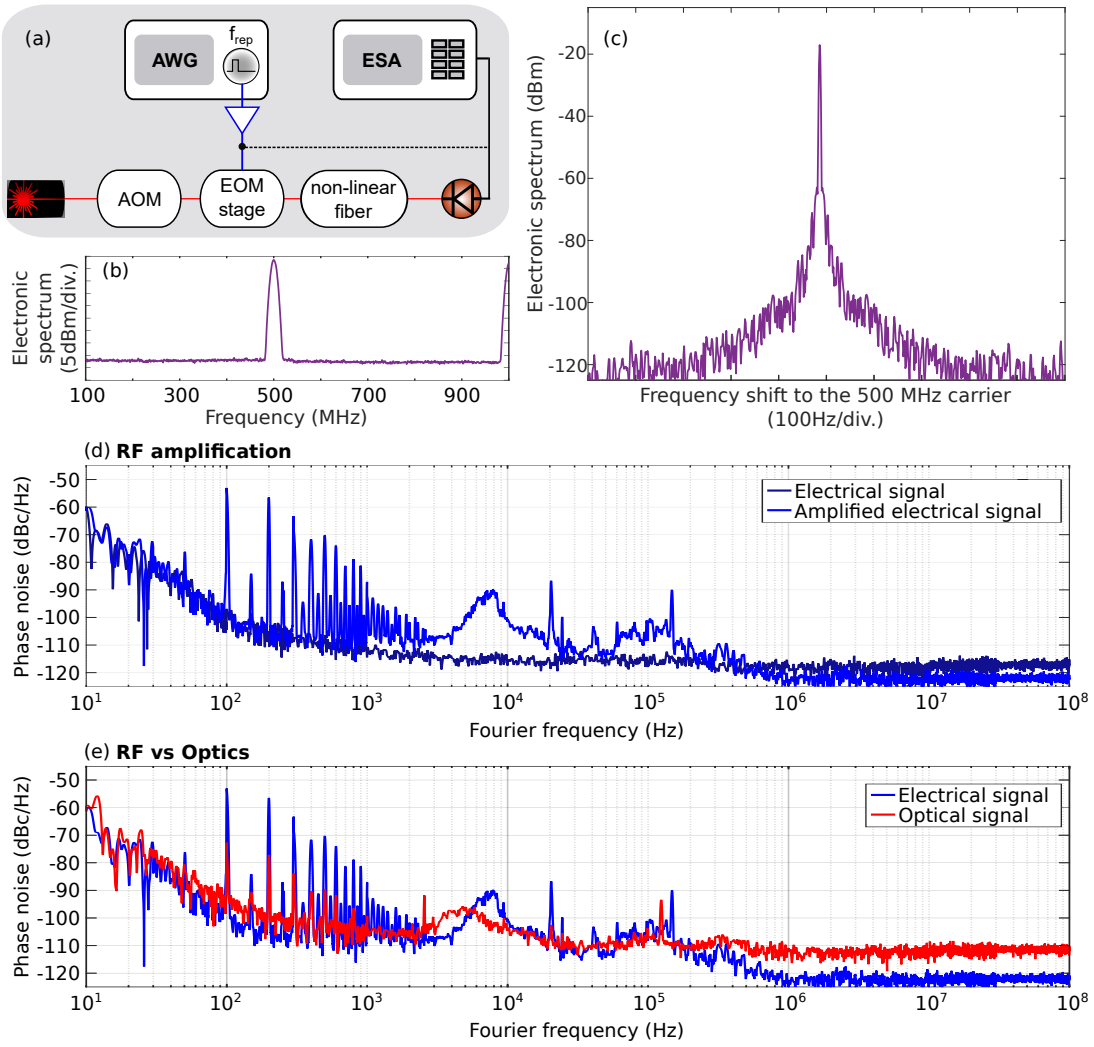

Figure 2.13: Phase noise of the repetition rate. (a) Scheme of the measurement. (b) Example of electric spectrum for comb1 at the input of the tri-core fiber. (c) Zoom on the first line at 500 MHz. (d) Measured SSB phase noise of this first mode at 500 MHz for the AWG output signal before (dark blue) and after (light blue) amplification. (e) Measured SSB phase noise of this first mode at 500 MHz for the RF system (blue line) and for the optical system (red line).

the intensity modulators. Resonances in the 1.10^2 - 5.10^3 Hz range, caused by the non-linearity of RF amplification, are reflected in the optical signal's phase noise. However, the optical curve and the RF curve do not exhibit the same noise trends, indicating that there is noise on the repetition frequency added by the optical chain.

Once this conclusion is drawn, it is necessary to identify which stage of the setup affects the short-term stability and in what manner. I therefore measured the phase noise at the input (effect of the electro-optic modulator stage) and at the output of the non-linear fiber (effect

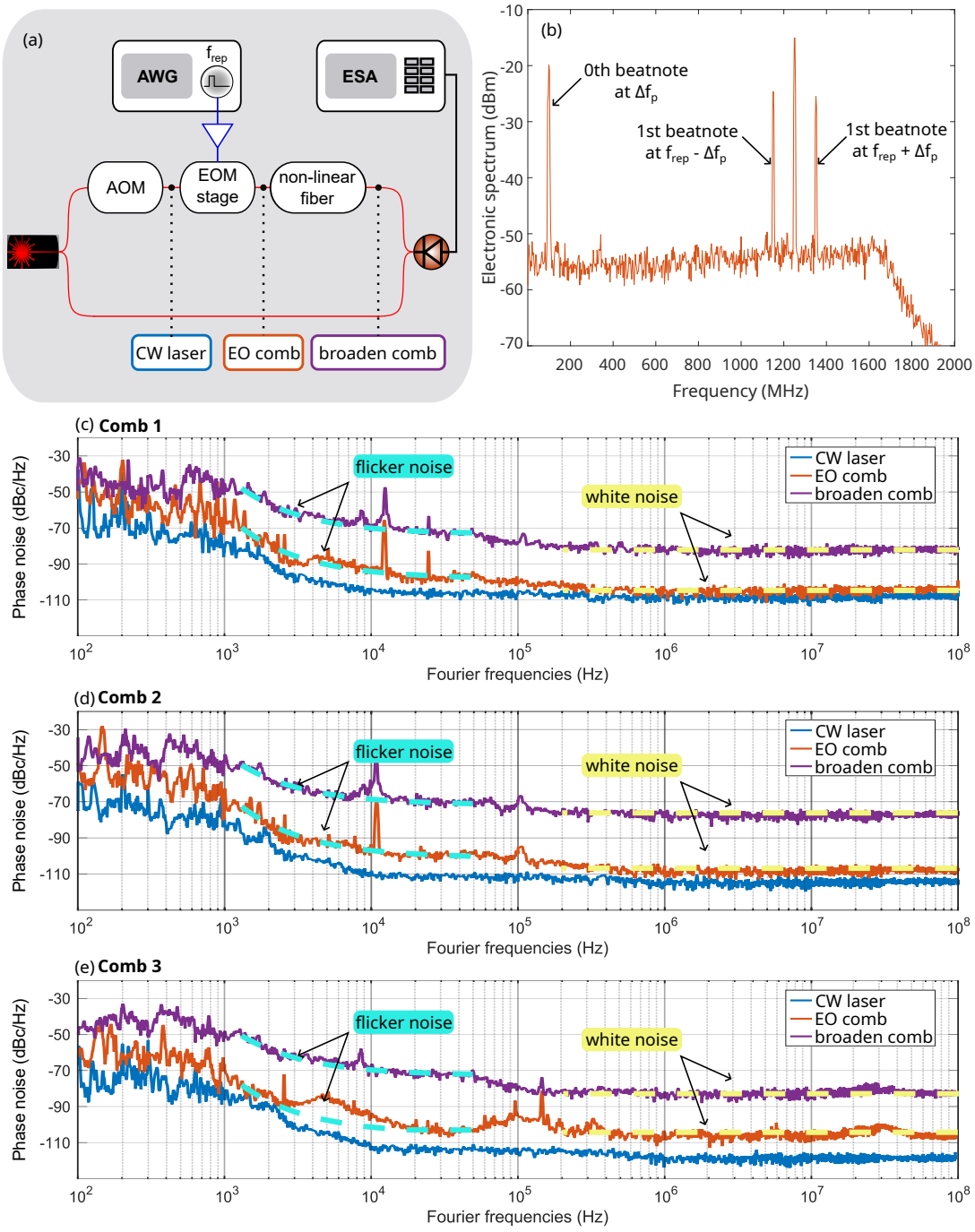

Figure 2.14: Uncorrelated phase noise at different stages of the set up. (a) Scheme of the measurement. (b) Example of electric spectrum for comb1 at the input of the tri-core fiber. (c)-(e) Measured SSB phase noise of the first mode from the beating with the initial cw laser, at different stages of the setup, for the three combs. The blue dotted line is the 1/f fit of the flicker noise, the yellow dotted line is the straight fit of the white noise due to detection.

of spectral broadening). To isolate the total contribution of a single optical line, the signal of interest is recombined with a portion of the continuous laser and detected by a photodiode (Thorlabs PDB480C). This represents the uncorrelated phase noise between the initial source and the generated frequency comb. Figure 2.14 presents the measurement set-up (a), an example of electronic spectrum from the beating (b) and the obtained phase noise spectra (c)-(e). The phase noise at the output of the AOM (blue curve) represents the measurement limit. The repetition rate is set at 1.25 GHz to minimize the number of modes within the photo-detector bandwidth (1.6 GHz), in order to enhance the SNR per mode. The measurements at both the input (EO comb) and the output of the non-linear fiber (broaden comb) exhibit flicker noise in the 10^3 Hz - 10^4 Hz region, eventually reaching the photo-detection noise floor. The spectral broadening is accompanied by a phase noise increase of 30 dBc/Hz, which is attributed to the effect of the EDFA, and the thermal and mechanical disturbances during the propagation in the 1 km fiber.

The remaining question is whether the accumulated phase noise depends on the repetition frequency. Figure 2.15 compares two measurements at f_{rep} = 500 MHz and f_{rep} = 1.25 GHz at the input (a) and at the output of the fiber (b). One noticeable difference is the increase in the photo-detection floor from 1.25 GHz to 500 MHz for the EO-comb measurement. Decreasing the repetition frequency results in an increase in the number of modes within the photo-diode bandwidth. As the measurement is done at a constant power on the photo-diode (2 x 50 µW), the power per mode is lower in the case of f_{rep} = 500 MHz, leading to a lower SNR per mode and thus an elevation of the photo-detection noise floor. In the case of the broadened combs, the phase noise is above the photo-detection threshold in all cases, and the two curves are similar.

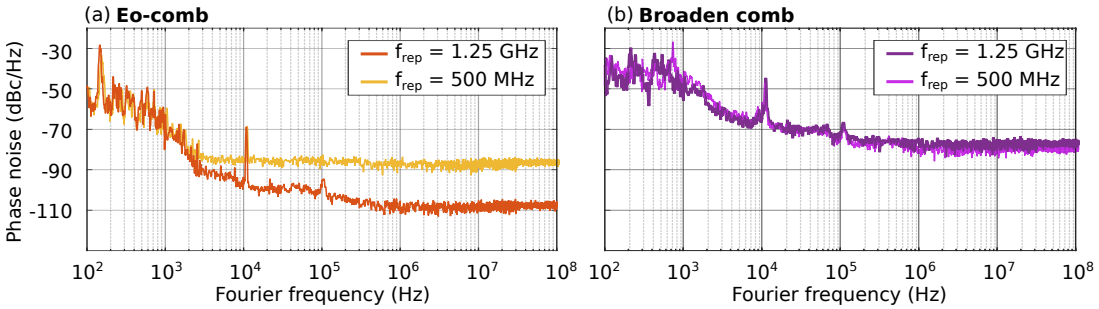

Figure 2.15: Uncorrelated phase noise for different repetition rates (a) at the input and (b) at the output of the tri-core fiber.

Consequently, it can be deduced that the phase noise at the output of the non-linear fiber is overall independent of the repetition frequency.

Recombining the frequency comb with the initial laser allows the evaluation of the uncorrelated noise between the two. To measure the total phase noise of the comb accurately, a heterodyne measurement can be performed using an independent local oscillator. I tried to implement that method using a second laser of the same model (NKT Koheras). However, both lasers were not frequency-locked to each other, and their carrier frequencies fluctuated over

the measurement time, causing significant spectrum fluctuations. These variations made it impossible to obtain a meaningful phase noise measurement that could reveal the system's behavior. To overcome the need for laser stabilization, the delayed self-heterodyne interferometric technique [166] was developed. It involves introducing a sufficient length of fiber in one of the interferometric arms to decorrelate the source with its duplicate. However, the CW laser used in the set-up has a very narrow linewidth (< 0.1 kHz). Its coherence length is therefore several thousands of kilometers. It would be very much impratical to use such a long length of fiber, in particular because of the induced losses. A method to circumvent this issue is the short delay self-heterodyne interferometry [167]. This technique could complete the study of the short-term stability of each comb.

2.4 Conclusion

In this chapter, I presented the experimental setup I developed to generate three coherent frequency combs from a single laser source using an all-fiber method that offers frequency agility. To achieve this, the transverse dimension of optical fibers was used for spatial multiplexing. A nonlinear tri-core fiber was designed by FiberTech, at PhLAM, wherein three narrow EOM combs are broadened by SPM. The resulting output of each core exhibits a flat-top spectrum with a spectral width of 1 THz, equivalent to over 1500 laser lines at a repetition rate of 0.5 GHz. The output pulse energy is measured to be 0.3 nJ, and we demonstrated that these pulses could be efficiently compressed to approximately 1 ps in pulse duration.

I evaluated the individual stability of each comb. A comparison with a commercially available frequency comb, using an Allan variation measurement, positioned the tri-comb system as more stable than a free-running fiber laser. I also conducted phase noise measurements to assess the short-term stability impact of each stage in the setup. The propagation in the non-linear fiber impacts the uncorrelated phase noise, thus degrading the SNR. However, these conclusions were established for each individual comb, whereas the interest of this set-up lies in its application to multi-comb interferometry. Indeed, it is possible for the coherence of a comb to be degraded, but for the mutual coherence between combs to be preserved. This will be the focus of the next chapter.

Chapter 3

Application of the multi-comb system to dual-comb interferometry

Outline of the current chapter

To assess the potential of the source developed for multi-comb interferometry applications, we evaluated the coherence between each pair of the three combs. First, we measured the stability of the interference signal, and then we carried out a dual-comb set-up to demonstrate the system's potential in practice.

3.1 Stability measurements

3.1.1 Stability of the difference of repetition rates

Tri-comb system

The last part of Chapter 2 presented the Allan deviations of the repetition frequencies of each individual comb. I performed the same measurement for the repetition difference, that is, for the repetition frequency of the optical beating between two combs. Indeed, this is the parameter that impacts the stability of recorded dual-comb interferograms. The optical signal is detected by a photodiode (Thorlabs PDB480C) and then filtered in the RF domain using a low-pass filter at 1 MHz. This filtering process selects only the repetition frequency difference. Its Allan deviation is shown in Figure 3.1 (a). Two measurements, made under similar conditions, compare the beating between the RF signals driving the EOMs (blue line) and the one between the optical first modes (red line). They both follow the same curve trend of $1/\sqrt{\tau}$ white frequency modulation noise [46]. This confirms that the frequency instabilities originate mainly from the control electronics in these EOM comb devices [25]. A longer measurement on the optical system (red dashed line) shows a stability level between $\sigma_y = 10^{-6}$ at low integration times and $\sigma_y = 10^{-9}$ over 3h. This order of magnitude corresponds to similar free-running fiber-optic systems [25, 26], with which high-precision spectroscopic measurements have been performed [168].

Menlosystem C-combs

Continuing with the intention of comparing the performance of our "home-made" system with those of a commercial system, I conducted identical measurements using the two mode-locked lasers from Menlosystem. This dual-comb system is equipped with electronic modules designed to lock the repetition frequencies of the two combs to a common reference. The stabilisation system is made such that comb1 must be locked first before locking comb2. Technical details regarding the operation of this feedback control are provided in Appendix A. In order to conduct a comprehensive comparison between the "home-made" system and the commercial system, I measured the Allan standard deviation of the repetition frequency difference in the following three configurations: when both lasers are locked, when only comb1 is locked, and when both lasers are in free running. The corresponding plots are shown in Figure 3.1 (b). The results are similar whether none or only one of the combs is locked, since the repetition frequency difference is influenced by the fluctuation of at least one of the repetition frequencies. In this respect, both dotted lines exhibit flicker noise up to a few seconds, and then random walk frequency modulation and frequency drift up to about 100 seconds. A maximum stability plateau of $\sigma_y = 2 \times 10^{-4}$ is reached in the region 0.1 s - 1 s. The quality of the stabilisation module is demonstrated by the position of the solid line below the other two lines. This solid line corresponds to a white noise fit. After 10^3 seconds, the Allan standard deviation is $\sigma_y = 1 \times 10^{-5}$, indicating that the commercial system is 1000 times more stable with feedback control.

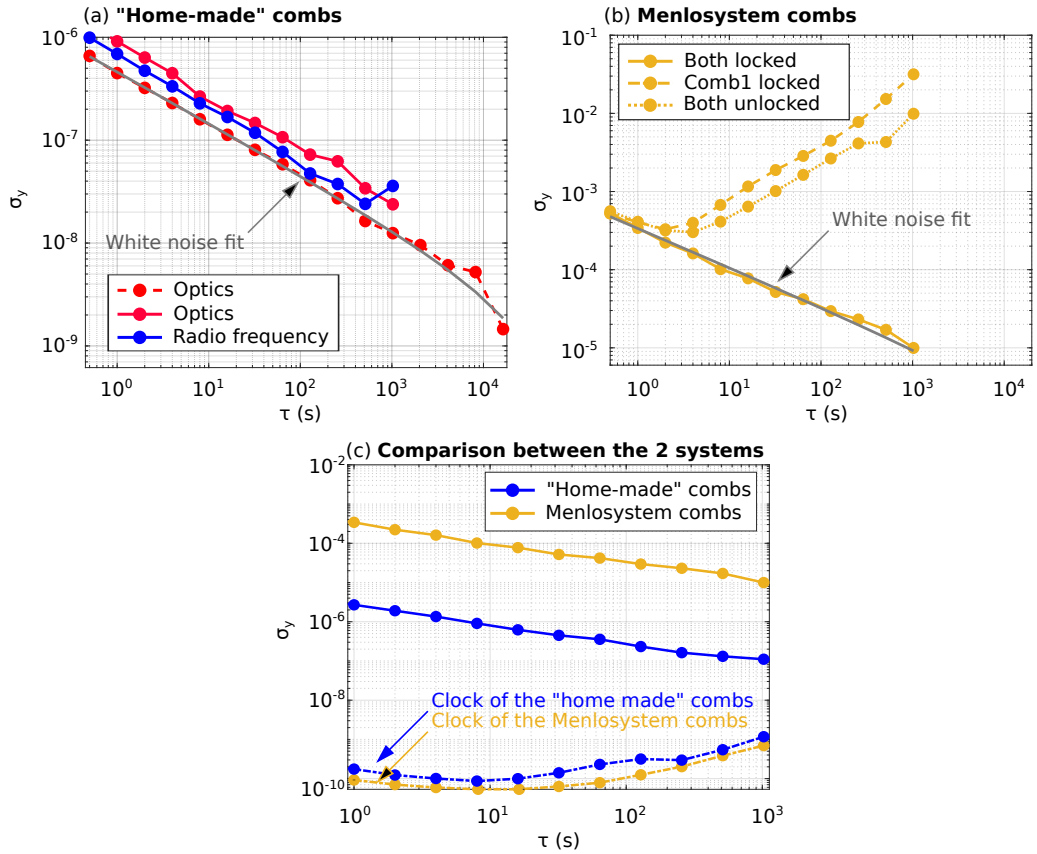

Figure 3.1: Allan deviation of δf_{rep}. (a) Measurement of the tri-comb system at 50 kHz between Comb1 and Comb 3 for $\tau_0 = 100$ ms and $\tau_{end} = 1$ h for the RF output (blue curve) and the optical output (red curve). A longer measurement ($\tau_{end} = 12$ h) is depicted in red dotted line, with the corresponding $\tau^{-1/2}$ characteristic white noise fit in grey. (b) Measurement of the the two commercial Menlosystems combs at 100 Hz for $\tau_0 = 100$ ms and $\tau_{end} = 1$ h in different configurations, with the corresponding $\tau^{-1/2}$ characteristic white noise fit (grey line) of the measurement when δf_{rep} is locked (solid yellow line). (c) Comparison between the two systems.

The comparison between the two systems is shown in Figure 3.1 (c). The Allan standard deviations of the clocks used in each set-up are also depicted for reference. They exhibit a similar trend, and their Allan standard deviation values are close. Hence, the difference of clocks cannot explain the difference in stability between the two systems. Indeed, the Allan standard deviation of the locked commercial dual-comb system is 10^2 higher than the one of "home-made" system over the entire range 1s - 100s. This observation does not allow to conclude that the tri-comb system is more stable, given the difference in spectral elements between the two dual-comb systems. Indeed, the Allan deviation of a relative frequency is $\sigma_y^2(\tau) = \frac{1}{2}\langle(y_{n+1} - y_n)^2\rangle$. As a first basic approach to assessing the influence of the number of modes, let's make the assumption that the variation in the difference of frequency between the modes vary independently of frequency. That implies that the overall fluctuation of frequency difference is proportional to the number

of modes. This hypothesis is not true for EO combs for instance, for which the linewidth of the modes increases in N^2, N being the number of modes [152]. However, the two dual-comb systems behave in a very different way, in addition with the fact that the dynamics of dual-combs from mode-locked lasers depend on many parameters [169], not least the stabilisation system. Therefore the assumption of white noise in the frequency difference does not reflect the real physics behind dual-comb systems, but it does allow us to understand the importance of the number of modes on their Allan variation. From this hypothesis, we can express that the relative frequency of the difference between N modes at the time t_n, denoted as y_n', is proportional to the relative frequency of the difference between two modes $\Delta\delta f_{\text{rep}}$ at the time t_n, denoted as y_n:

$$y_n' = \frac{(N-1)\times\Delta\delta f_{\text{rep}}}{\delta f_{\text{rep}}} = (N-1)\times y_n \tag{3.1}$$

And from this assumption, we can deduce that Allan's standard deviation is proportional to the number of modes:

$$\sigma_{y'}(\tau) = (N-1)\times\sigma_y(\tau) \tag{3.2}$$

The frequency comb spectrum of the Menlosystem extends from 1490 nm to 1650 nm, resulting in a spectral width of 19.5 THz at f_{rep} = 100 MHz. Therefore, the commercial system is composed of 10^5 modes, whereas the tri-comb system consists of 10^3 modes. However, the difference in the Allan standard deviation between the two systems is greater than 10^2. This suggests that the difference of repetition rates of the "home-made" free-running system achieves a level of stability comparable to the one of the commercially available dual-comb system, whose repetition frequency is stabilized.

3.1.2 Coherence between two combs

To highlight the added value of using a tri-core fiber rather than three separate fibers, I evaluated the relative coherence between the combs by measuring the linewidth of the RF beat note between two combs. This method is inspired by [23]. A scheme of the measurement setup is provided in Figure 3.2 (a). The measurements were performed on combs 1 and 2, whose optical spectra are presented in Figure 3.2 (b). The spectrum obtained by SPM in a non-zero-dispersion-shifted fiber (NZDSF - LEAF; D = 4.4-5.8 ps/(nm.km) at 1550 nm), with the same input EO-comb as comb1, is also shown in the figure. This NZDSF output will be used later for comparison to highlight the importance of spatial multiplexing to maintain the mutual coherence between the combs.

An ultra-narrow continuous-wave laser (NKT Koheras), identical to the CW source used in the tri-comb setup, is divided into two parts to interfere with each output comb, acting as the local oscillator (LO). This produces a multitude of beating lines at frequencies of $n\times f_{\text{rep}} \pm \Delta f_p$ and $n\times f'_{\text{rep}} \pm \Delta f'_p$, with Δf_p being the LO's carrier frequency difference with comb1, $\Delta f'_p$ the LO's carrier frequency difference with comb2, and $f_{\text{rep}} = f'_{\text{rep}}$ the repetition frequency of both

combs. As the carriers of comb 1 and comb 2 are separated by 100 MHz (imposed by the AOMs on Channels 1 and 2), we obtain $|\Delta f_p' - \Delta f_p| = 100MHz$. These two optical beatings are detected separately on two photodetectors (Thorlabs PDB480C and Menlosystems FPD610). Figure 3.2 (c) and (d) show the two electronic spectra recorded on the ESA. Both spectra contain peaks from the comb centered at $n \times f_{\text{rep}}$, as well as the beating with the LO at $\pm\Delta f_p$ (respectively $\Delta f_p'$) of each of these peaks. The goal is to combine the first modes at frequencies $f_{\text{rep}} - \Delta f_p$ for comb 1 and $f_{\text{rep}} - \Delta f_p'$ for comb 2. To achieve this, RF filters (high-pass filter at 200 MHz and low-pass filter at 400 MHz) are used to select only the line of interest in the beating with comb 2. The two RF signals are then combined using a frequency mixer. This RF recombination eliminates the noise component of the LO. The width of this final RF beat note provides the inverse of the coherence time between the two combs.

Figure 3.2 (e) shows this RF beating recorded on an ESA with a resolution of 1 Hz, and averaged 10 times. The one between combs 1 and 2 broaden in the multi-core fiber is about 20 Hz at 0.2 of its maximum (dark blue curve). It indicates high relative coherence of the pair of combs. For comparison, the light blue curve is the measurement made upstream of the setup, on the source laser divided in two, with one arm shifted in frequency by an AOM. It corresponds to the limit of our measurement, physically due to the spectral resolution of the ESA.

To obtain a comparative measurement, I repeated the same experiment with two combs at the output of two fibers on separate spools of the same fiber length. For that, I used comb2 (at the output of the tri-core fiber) and the output of a NZDSF with eo-comb1 as input, to operate under the same conditions. The purple curve in Figure 3.2 (b) shows the SPM induced spectrum at the output of the NZDSF. The broadening is less than that of the tri-core fiber output, as the fiber parameters are not the same (length L = 1 km, low dispersion D = 4.4-5.8 ps/(nm·km) at 1550 nm, and slightly smaller non-linearity with Mode Field Diameter = 9.6 µm at 1550 nm). However, this does not affect the measurement on the first beatnote. As can be seen in Figure 3.2 (f), the linewidth of the RF beating between comb2 and the separate comb from the NZDSF is 400 Hz at 0.2 of its maximum power (ESA signal averaged 10 times). Coherence degradation is 20 times higher than when using two cores of the tri-core fiber. This degradation in coherence by more than one order of magnitude illustrates the great advantage of implementing spatial multiplexing in a non-linear fiber to broaden the combs while preserving the mutual coherence.

One can argue that this difference in mutual coherence might be due to the fact that independent fibers are not localized at the same spot. Therefore, they are not subjected to the exact same mechanical and thermal variations. The contribution of the multi-core fiber to mutual coherence would primarily come from the physical proximity of the cores. To evaluate the validity of this statement, I repeated the coherence linewidth measurement, this time comparing two comb spectra broadened in the cores of the TC fiber and two comb spectra broadened in two independent NZDSFs, but wound on the same spool. Figure 3.3 (a) shows the OSA spectra from the respective broadenings, with the same input eo-comb parameters for both TC fiber and NZDSFs. Their differences arise from the fact that the NZDSFs are not strictly identical to the

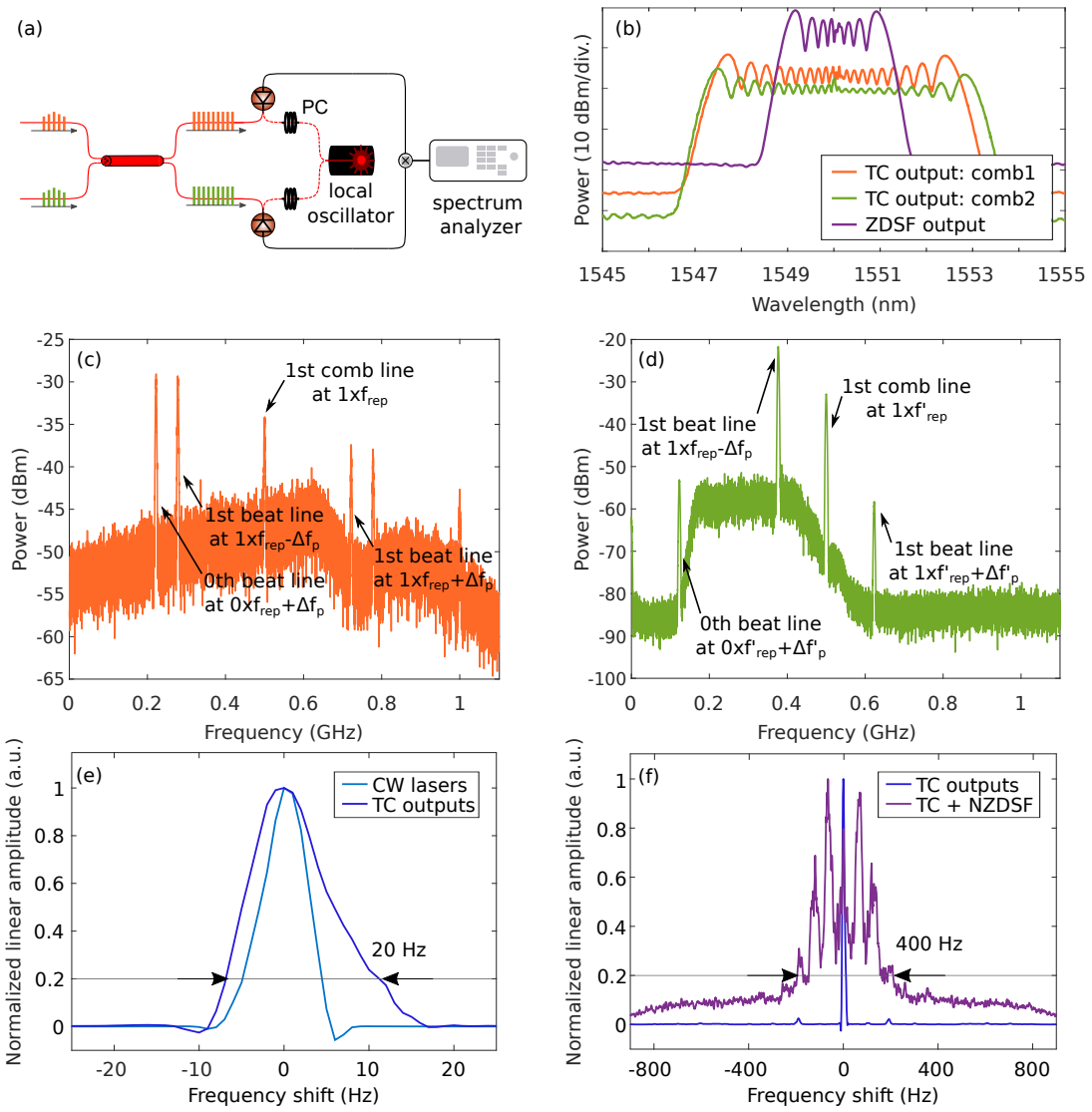

Figure 3.2: Coherent linewidth of the beating between the first modes of the output combs. (a) Experimental set-up. (b) OSA spectra of the two broaden combs in the TC fiber and in the NZDSF. (c) ESA spectrum of the beating between comb1 and LO. (d) ESA spectra of the beating between comb2 and LO. (e) RF beating obtained between the optical beatings of comb1 and comb2 with the LO, after broadening in the tricore fiber. (f) Beating obtained between two broadened combs in two independent nonlinear fibers (1 NZDSF and 1 core of the TC fiber). PC = polarisation controller; OSA = Optical spectrum analyzer; LO = local oscillator; ESA = electronic spectrum analyzer; TC = tri-core; NZDSF = non zero dispersion shifted fiber.

TC, but they have similar parameters (length L = 1 km, low dispersion D = 4.4-5.8 ps/(nm·km) at 1550 nm, and slightly smaller non-linearity with Mode Field Diameter = 9.6 µm at 1550 nm). Figure 3.3 (b) presents the RF beating resulting from the recombination of the two combs

with the LO, this time averaged 100 times. The light blue curve is the reference measurement with the input eo combs, to compare with the broadening in the TC (dark blue curve) and the broadening in the independent NZDSFs (pink curve). It can be observed that the beating with the independent fibers is more than twice as wide as that obtained with the TC fiber. This means that spatial multiplexing ensures mutual coherence at least two times higher. This is in addition to the fact that it naturally provides equalization of mechanical and thermal disturbances, as well as a smaller spatial footprint compared to multiple independent fibers.

The conclusion regarding the contribution of the multi-core fiber to mutual coherence by a factor of 2 is a minimum assertion. Indeed, the comparison with the measurement on the eo-combs allows us to deduce that mutual coherence is limited by the degradation upstream of the TC fiber, since the dark blue and light blue curves are very similar in shape and width. The limitation of our system would therefore be due to the electro-optical chain before the broadening, and the multi-core fiber would offer even greater stability compared to multiple independent fibers.

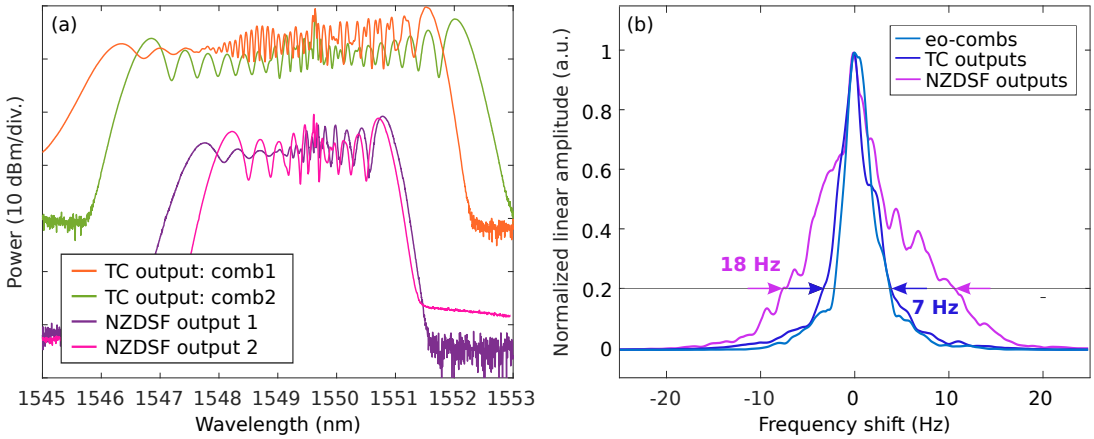

Figure 3.3: Coherent linewidth of the beating between the first modes of the output combs. (a) OSA spectra of the two broaden combs in the TC fiber and of the comb broaden in the two NZDSFs. (b) RF beating obtained between the optical beatings of comb1 and comb2 with the LO, after broadening in two cores of the TC fiber (dark blue) and after broadening in two independant NZDSFs on the same spool. LO = local oscillator; ESA = electronic spectrum analyzer; TC = tri-core; NZDSF = non zero dispersion shifted fiber.

We believe that this could be even better by optimizing the core separation. In this work, it was set at 30 μm to ensure there is a negligible cross-talk between the cores, and to facilitate the fabrication of the fans, but as it gets closer, the phase noise degradation due to the external perturbations of the light beams propagating in each core would get increasingly similar, leading to an enhancement of the mutual coherence. The practical limitation is imposed by the cross-talk if the cores are too close and/or by the the fan fabrication. Another option is to twist the fiber during the fabrication process to achieve a nearly identical average perturbation for the beams. This will be investigated in the next section.

3.2 Twisted tri-core fiber

3.2.1 Description of the twisted tri-core fiber

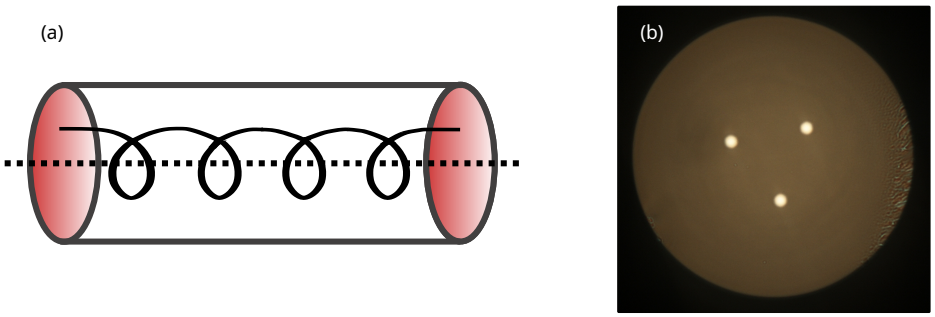

Figure 3.4: Twisted tri-core fiber. (a) Scheme of the cross section for one core. (b) Microscope image at x50 of the input plane showing the three cores, separated of 30 µm.

The experiment described in 3.1.2 was dedicated to demonstrating the advantages of spatial multiplexing in a multi-core fiber compared to using three independent fibers. The goal is to minimize the accumulated phase noise during propagation in the nonlinear fiber across all channels. One approach to enhance mutual coherence is to introduce a twist in the fiber during the fabrication process, aiming to achieve nearly identical average perturbations for the individual beams. This method's effectiveness has been previously demonstrated by our research group in the context of coherent beam combining, as shown in Ref. [170], leading to significant improvements in beam stability. Therefore, this was a strategy we aimed to implement by developing a twisted tri-core fiber (presented in Figure 3.4) possessing properties similar to those of the straight fiber used in the experiment. The cores all come from the same glass preform. The fiber was pulled at a speed of 800 rpm with a pitch of 33 mm. Its total length is 1.3km, with 20 m of untwisted fiber at the end to optimized the coupling with the fan-out. Similar parameters of the input EO combs lead to the generation of comparable output spectra, as depicted in Figure 3.5. This confirms that the two fibers possess similar properties. To integrate the new tri-core fiber after the existing EO-comb setup, fans were made at FiberTech. These fans exhibit higher losses (-5.54 dB, -7.55 dB, and -10 dB) compared to the commercial fans used for the straight fiber, resulting in limited broadening at the output of the three cores. Nonetheless, it is entirely feasible to measure the coherence linewidth between the first two modes of the frequency combs, as described in 3.1.2, and compare the obtained results for the two nonlinear fibers. This comparison will allow to draw conclusions regarding the effect of the twist on the mutual coherence.

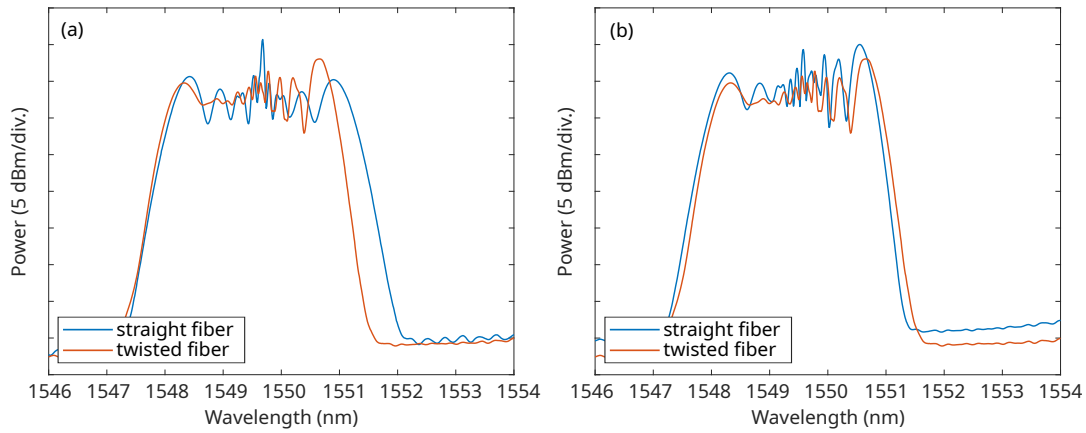

Figure 3.5: Comparison of the OSA spectra at the output of the two non-linear fibers for (a) comb1 and (b) comb2.

3.2.2 Coherence linewidth measurement

The set-up is identical to the one described in section 3.1.2. In this previous case, the RF beatnote was recorded at the ESA. The device's resolution (1 Hz) was sufficient to compare the performance of the straight multi-core fiber with that of independent fibers. Figure 3.6 (a) presents the results of this measurement at the ESA under exactly the same conditions as the output of the AOM, the output of the EO-comb stage, and the output of the straight nonlinear fiber. The widths of these three peaks are indistinguishable; the measurement resolution does not allow highlighting the likely degradation of coherence as the combs propagate along the set-up. To enhance this resolution, it is possible to record the RF beatnote's temporal trace on an oscilloscope and calculate its Fourier transform. The resolution of this measurement is defined by the total time span T that can be recorded. This value T depends on the number of points Npts and the sampling frequency $F_{sampling}$: $T = Npts/F_{sampling}$. In our case, Npts is limited to 50 Mpts. The RF beatnote results from the recombination between the first modes of the two frequency combs, frequency-shifted by $\delta f_{AOM} = 100$ MHz. The RF beatnote is thus centered at 100 MHz, and the Shannon criteria dictates $F_{sampling} \geq 200$ MHz. The oscilloscope-recorded measurement resolution is therefore limited to 4 Hz, which is still higher than the measurement recorded at the ESA. To overcome this issue, I combined the relevant RF beatnote with an external oscillator at 101 MHz. This translated the beatnote to 1 MHz, enabling the temporal trace to be sampled at a much lower frequency and thereby improving the resolution.

Figure 3.6 (b) illustrates this improved set-up. To ensure that this measurement works properly, I tested the improved set-up to measure a 100 MHz RF signal. This is shown in Figure 3.6 (c). There is a clear improvement in the measurement resolution, with the RF oscillator noise not degrading the signal of interest. I therefore applied this measurement protocol to the combs at the output of the straight tri-core fiber and at the output of the twisted tri-core fiber. The RF beat is recorded on the oscilloscope and the TF is directly calculated by the device with a

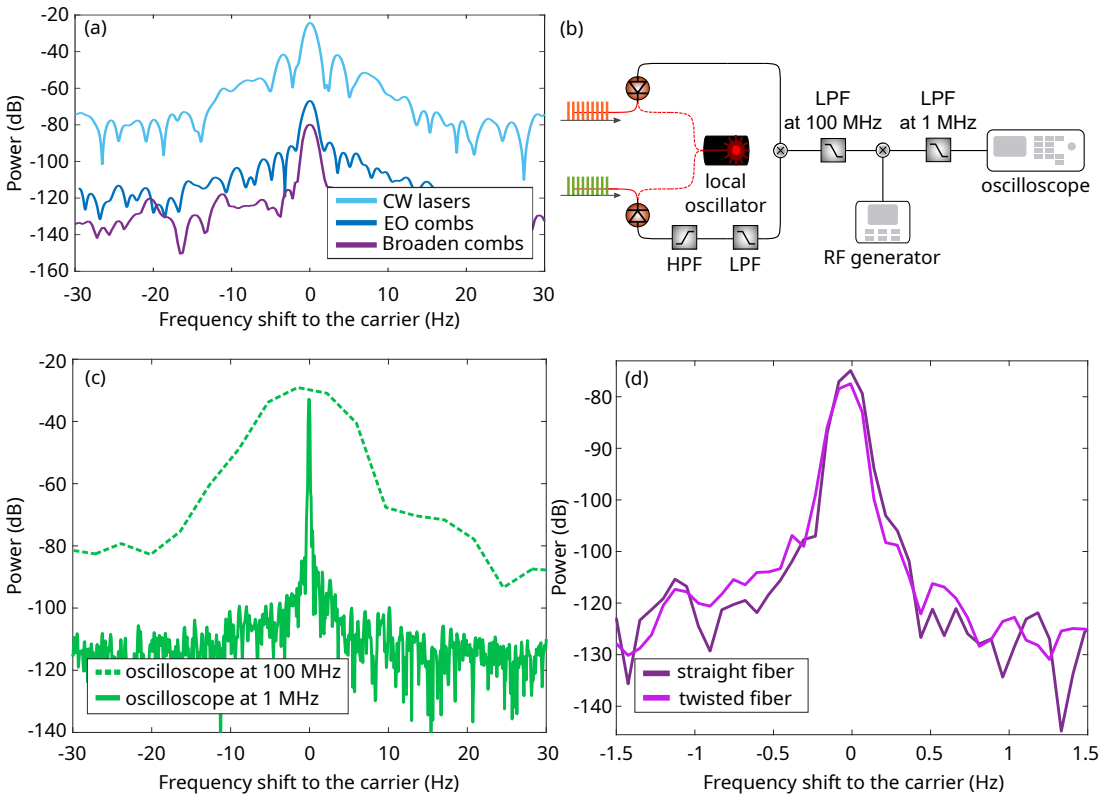

Figure 3.6: Coherence between the dual-comb pairs: straight vs twisted fiber. (a) ESA mesurement of the RF beating at 100 MHz at different stages of the set-up. One can notice that the resolution isn't good enough to highlight the degradation of the coherence. (b) Scheme of the improved set-up with a RF LO at 100.1 MHz beating with the RF beatnote. (c) Test of this set-up on a RF oscillator at 100 MHz. The measurement shows a greater resolution (75 mHz) compared the one without RF oscillator (4 Hz). (d) Coherent linewidth of the beating between the first modes of the combs at the output of the straight fiber (purple) and at the output of the twisted fiber (pink).

resolution of 75 mHz. The corresponding beatnotes are displayed in Figure 3.6 (d). They both exhibit a linewidth of 0.5 Hz at -10 dB. The very good resolution of this measure still does not allow us to distinguish the difference in width between the two peaks. This means that what limits mutual coherence is not a priori the widening in the tri-core fiber, but rather the upstream chain of eo-combs. It is this part of the set-up that needs to be improved as first step, which will be addressed in the perspectives section of this manuscript. Therefore, we cannot draw conclusions regarding the improvement of coherence using a twisted fiber rather than a straight one. In the remainder of this manuscript, all the results presented are taken from measurements using the multi-comb system broadened in the straight non-linear fiber.

3.3 Dual-comb configuration

Once the coherence of each pair of the tri-comb system was measured, I set up a dual-comb interferometer to demonstrate the mutual coherence in practice.

3.3.1 Dual-comb interferogram

To begin with, the interferograms are recorded "unloaded", meaning that no absorbing or dispersive element is introduced in the arms of the interferometer. The parameters of the two combs are chosen to meet the conditions stated in 1.3.2. Firstly, the repetition rate is fixed according to the desired spectral resolution, and the optical sources are adjusted to have a spectrum as symmetrical as possible, with a good SNR and an overall flat envelope. Once the spectral width $\Delta\nu$ and the repetition rate f_{rep} are set, the difference of repetition δf_{rep} is chosen such that the RF spectrum, with a width of $\frac{\delta f_{\text{rep}}}{f_{\text{rep}}} \times \Delta\nu$ and centered at $\Delta f_p = \Delta f_{\text{AOM}}$, fits in the 0 - $\frac{f_{\text{rep}}}{2}$ range. The two combs are then combined using an optical coupler and a polarization controller. The beating is detected using a photodetector (Thorlabs PDB480C - 1.6 GHz passband). The RF output is low-pass filtered around $\frac{f_{\text{rep}}}{2}$ and then recorded on a 10-bit oscilloscope (Keysight DSOS4805A). The sampling frequency is chosen to be a multiple of f_{rep} and δ f_{rep}. It determines the number of points per interferogram period and, therefore, the number of interferograms in the total vector of 50 Mpts recorded.

Figure 3.7 presents an example of dual-comb interferometry between combs 1 and 2. The repetition frequency is set at 500 MHz. Figure 3.7 (a) shows their optical spectra with a width of $\Delta\nu$ = 0.6 THz. Figure 3.7 (b) represents three periods of the total vector of N_{tot} = 50,000 interferograms recorded at a sampling frequency F_{sampling} = 5 GHz. Figure 3.7 (c) is a zoom on a single interferogram burst, which corresponds to the temporal superposition of the two trains of pulses. The total vector of N_{tot} interferograms is divided into N packets of n interferograms. The N packets are averaged to obtain an average vector of n interferograms with a better SNR. The RF spectrum is then calculated from the FT of this average vector. The number of interferograms n thus quantifies the resolution of the RF spectrum and corresponds to the number of points between the peaks spaced by δf_{rep}. Figure 3.7 (d) shows the RF spectrum from n = 5 interferograms averaged N = 2.10^4 times. It contains about 1500 RF modes with an SNR of typically 15 dB. Figure 3.7 (e) shows the RF spectrum from n = 50 interferograms averaged N = 2.10^3 times. It reveals a clear comb structure with a 50 kHz spacing between the teeth corresponding to the value of $\delta \mathbf{f}_{\text{rep}}$. That proves the good mutual coherence of the pair of frequency combs.

As mentioned in the precedent paragraph, the SNR of the dual-comb measurement can be improved by performing coherent averaging (N times) [7, 20, 23]. The evolution as a function of the number of averages is shown in Figure 3.8 (circles) at the input (blue circles) and output (orange circles) of the fiber. We find the characteristic $\sqrt{N}$ evolution of the SNR (solid lines)

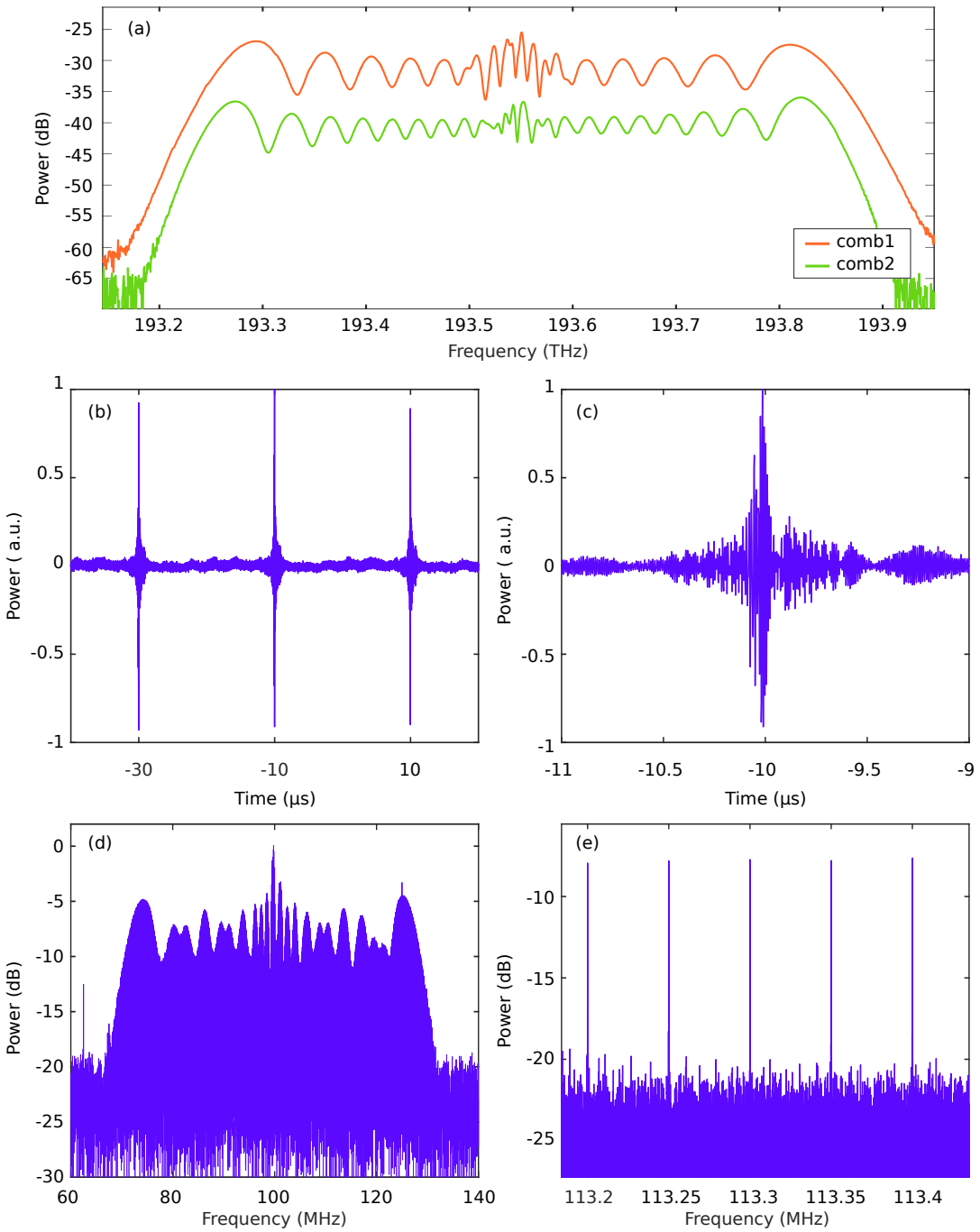

Figure 3.7: Dual-comb interferometry. (a) OSA spectra of two combs at f_{rep} = 500 MHz. (b) Multi-period interferogram with δf_{rep} = 50 kHz. (c) Zoom in on a single interferogram trace. (d) Dual-comb spectrum calculated over n = 5 interferograms averaged N = 20000 times. (e) Zoom in on the comb structure with n = 50 and N = 2000.

[113]. The degradation of the SNR between the input EOM combs and the output combs comes mainly from the difference in the number of spectral lines: it goes from $M_{eocomb} = 100$ at the input to $M_{comb} = 1500$, which leads to a decrease of 12 dB [45], close to the 15 dB experimentally recorded. We attribute the additional degradation to the noise from the optical amplification and from the propagation in the tri-core fiber.

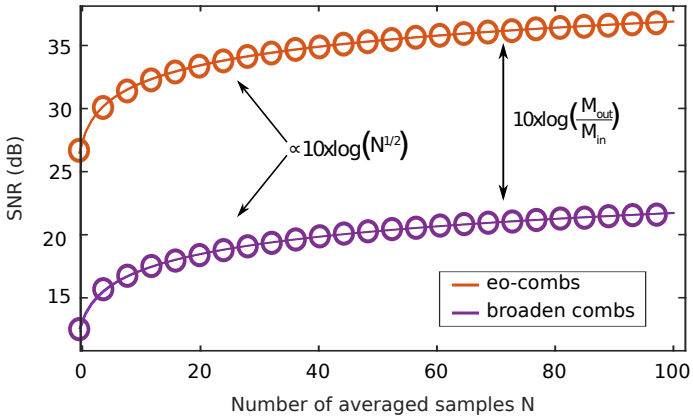

Figure 3.8: Evolution of the SNR of the RF spectrum as a function of the number of averaged sets N at the tri-core fiber input (orange trace) and at the output (blue trace). The circles are the measured data, and the solid lines are the computed fits corresponding to an evolution as $10\log(\sqrt{N})$.

This characteristic evolution confirms the smooth operation of the set-up in a dual-comb configuration.

3.3.2 Dual-comb measurements

As presented in section 1.3, dual-comb interferometry is a common method for measuring the absorption of a sample to be characterised. In order to evaluate the performance of the setup in this domain, I tested this method with each pair of the tri-comb system on two types of fiber components.

FBG - absorbing sample

A Bragg grating is a reflector device inscribed on a fiber, which to some extent imitates the behaviour of absorption lines in spectroscopy. I carried out a dual-comb measurement to obtain the transmission of this component. Figure 3.9 (a) illustrates the set-up. The two combs are divided in two so that there is a measurement channel and a reference channel. The Bragg grating is inserted in the measurement channel, along with a circulator to eliminate the reflection generated. As the frequency combs are widened by SPM, their spectral envelopes are sensitive to power variations due to the optical amplifier at the non-linear fiber input. Real-time measurement using a reference channel prevents these effects of fluctuations in the dual-comb

source. Since the PDs on the two channels are different (Thorlabs PDB480C and Menlosystems FPD610), an initial 'no-load' measurement is carried out to calibrate the two channels.

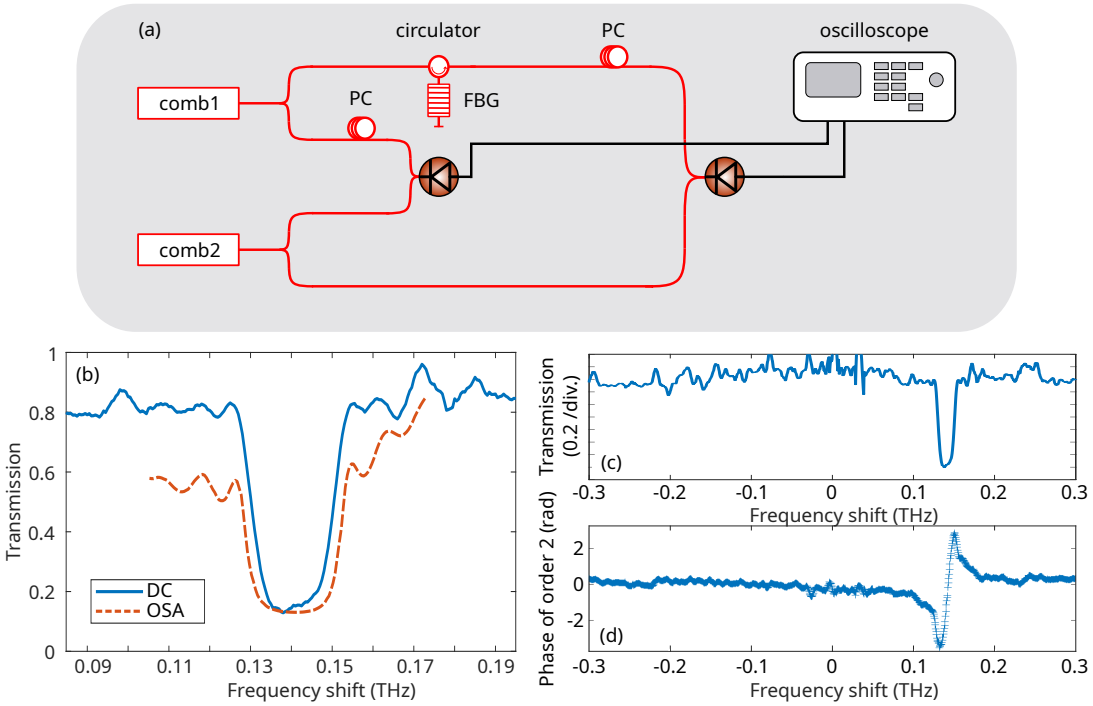

Figure 3.9: Dual-comb measurement. (a) Schema of the meaurement set-up (b) Zoomed-in transmission spectrum of the FGB. (c) Transmission and (d) Phase of the FBG on all the dual-comb spectral range. FBG = fiber bragg grating; PC = polarization controller; DC = dual-comb; OSA = optical spectrum analyzer.

The repetition rate is set at 500 MHz, enabling to get 40 points over the absorption gap (20 GHz) of the FBG. The difference of carrier frequency is set by the respective AOMs at 100 MHz and the repetition rate difference is set at 50 kHz to ensure a good sampling in the RF domain. For each measurement, I recorded 1000 interferograms on the oscilloscope at a sampling frequency F_S = 2 GHz and performed an averaging to increase the signal to noise ratio [20] at N = 100. From the recorded RF spectra, I reconstructed the optical spectra. This means subtracting the center frequency of the dual-comb signal δf_{AOM} = 100 MHz and stretching the spectrum by the magnification factor $M = \frac{1}{a} = \frac{f_{\mathrm{rep}}}{\delta f_{\mathrm{rep}}} = 10^4$ [7, 20]. Transmission is obtained by taking the ratio of the spectra as the following: $\frac{\text{Measurement}}{\text{Reference}} \times \frac{\text{"No-load" reference}}{\text{"No-load" measurement}}$. Figure 3.9 (b) presents a zoom in the range of interest. In addition with the overall losses of 20 %, there is a gap of the transmission of 65% around the frequency shift of 0.14 THz from the carrier at 193.35 THz. That corresponds to a reflection peak of -19 dB at 1549.4 nm when the datasheet indicates a reflection of -20 dB at 1549.8 nm. Ageing of the component may explain these slight shifts [171]. An OSA measurement of the transmission is carried out using a fs-source (Pritel) for comparison (orange

dotted line). Due to the significant fluctuations of its spectral envelop (see appendix B), this measurement only provides an indication of the FBG reflection's position. The transmission gaps of the two measurements (DC and OSA) coincide. Figure 3.9 (b) depicts the transmission across the entire spectral range of the measurement. Figure 3.9 (c) is the corresponding added phase, entitled "phase of order 2" since the linear contribution has been subtracted. The reflection peak at a frequency shift of 0.14 THz is associated with a phase jump. Beyond this spectral peak of 0.02 THz width, the Bragg grating does not influence the transmission (besides the overall losses of 20%). Thus, this first measurement confirms the potential of the set-up as dual-comb interferometer.

SMF - dispersive sample

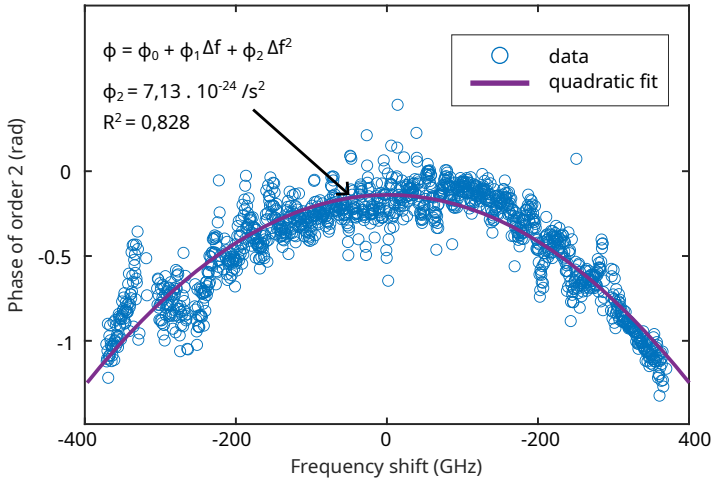

Figure 3.10: Phase profile at the dual-comb at the output of a standard SMF-28 fiber of 20 cm (blue dots) and its quadratic fit (purple line).

The stability of the dual-comb sources is further illustrated by measuring the group velocity dispersion of a 20 m long piece of SMF28 fiber. I inserted the fiber under test in place of the measured system {Bragg grating + circulator} in the same set-up shown in Figure 3.9. I calculated the spectral phase added by this element. After removing the linear part, the second-order phase is displayed in Figure 3.10. A quadratic fit is performed to obtain the value of ϕ_2 (purple trace). From the Taylor expansion of the phase with respect to angular frequency [88], we can deduce the dispersion formula: $\beta_2 = \frac{\phi_2}{2\pi^2 L}$. In our case, the length of the fiber is $L = 18.8,\mathrm{m}$. The coefficient of determination, denoted as R^2, is 0.828, which is not satisfactory. That corresponds to the variations around the bell-shaped mean. These variations coincide with the characteristic form of the remaining non-linear phase induced by SPM [88]. To assess the reliability of the measurement, I repeated it 50 times. The mean value of this sample of 50 measurements is $\beta_2 = -19.2\,\mathrm{ps}^2/\mathrm{km}$, with a standard deviation of 3.3 $\mathrm{ps}^2/\mathrm{km}$. The fiber used is a G652D CableCOM fiber, with a chromatic dispersion at 1550 nm indicated to be less

than $18,0\text{ps/nm}\cdot\text{km}$. The dual-comb measurement of the dispersion ($\beta_2 = -19.2,\text{ps}^2/\text{km}$) is, therefore, in good agreement with the manufacturer's threshold value of $\beta_2^{\text{G652D}} \leq 22\text{ps}^2/\text{km}$. This tricky measurement of the spectral phase added by a dispersive element illustrates the very good mutual coherence of the dual-comb pairs of the tri-comb system.

3.4 Conclusion

In this chapter, I have presented the evaluation of the mutual coherence of the pairs of the tri-comb system. Firstly, I carried out a study of the long-term stability of the difference in repetition frequency, compared with the commercial dual-comb system. This showed that the home-made system performed well, even though it was in a free-running configuration. I then assessed the mutual coherence of the pairs of combs by direct measurement of the line thickness of the beat between the first optical modes of the two combs. Comparison with a broadening in two independent fibers led to the conclusion that spatial multiplexing within a single non-linear fiber was important in maintaining coherence. I then sought to demonstrate the potential improvement in this stability in a twisted multi-core fiber. The current measurement does not allow any conclusions to be drawn, and a further study will have to be carried out. I then carried out dual-comb measurements in a vacuum, then by inserting fiber components to simulate absorption and dispersion. The good quality of the RF spectra (flat envelope, good SNR, good stability over time) and the experimental results, which correspond to the datasheets, provide information about the effectiveness of the system used in a dual-frequency comb arrangement. However, the novelty of this work lies in the fact that it is a tri-comb coherent system, which is the subject of the next chapter.

Chapter 4

Application of the multi-comb system to tri-comb interferometry

Outline of the current chapter

Tri-comb interferometry falls under the umbrella of FWM spectroscopy [134], since it involves the non-linear interaction of two propagating light waves within a medium, leading to the generation of a signal wave. This signal is probed by a third comb. The scheme is very similar to the photo echo excitation scheme [137, 172], inspired by nuclear magnetic resonance spectroscopy [139]. In our case, we study the dynamics in the spectral domain, rather than looking at the time signature of the photon echo. The interaction between the three combs relies on their good coherence, and so it is through an experimental demonstration of FWM spectroscopy that we assess the source's potential for non-linear spectroscopy applications. Firstly, a preliminary study is conducted both numerically and experimentally using the three electro-optic combs. The narrow spectral width of these intermediate sources provides a high degree of freedom for studying the phenomenon of intra-envelope pulsed FWM. To our knowledge, this is the first experimental demonstration of this specific FWM configuration, made possible here by the high

spectral resolution of the tri-comb measurement. The last part of this chapter is dedicated to the experimental results of FWM obtained with the three broadened combs, thus demonstrating the potential of the multi-comb source for 2D spectroscopy.

4.1 Tri-comb interferometry with the eo-combs: intra-envelop FWM

The non-linear interaction between two pulse trains operating at the same repetition rate, but with slightly different carrier frequencies, leads by FWM to the generation of new components within their spectral envelops. We call this phenomenon *intra-envelop FWM*. The frequency differences between the FWM components and the pump lines are in the RF domain. That makes the process almost impossible to observe using a standard optical spectrum analyzer, due to its limited spectral resolution. Using a third light source as a multi-line local oscillator makes the analysis of these new spectral components accessible. It enables to extract these FWM components from the spectra of the initial light sources by exploiting the down-conversion process of multi-comb interferometry [146].

4.1.1 Presentation of the phenomenon

Two combs as pumps

As theoretically presented in Section 1.2.3, FWM is a fundamental nonlinear effect when at least two waves interact to generate new spectral components [173]. In its simplest (degenerate) form, two CW lasers generate new side-bands that are symmetrical on either side of the pump spectral lines. That case is presented in Figure 4.1 (a), under the name CW-FWM. The phenomenon can quickly become more complex in long fiber spans, or with higher powers, giving rise to multiple FWM interactions (mFWM) [174]and it can lead to frequency comb generation [102, 103]. CW pumps can be replaced by pulsed pumps, degenerated or not, to get higher peak powers and thus more efficient non-linear interactions. A striking illustration is provided by EO combs that are broaden in nonlinear fibers [25, 175]. Other configurations based on FWM involving pulsed pump(s) and signals are related to fiber optical parametric amplifiers to amplify or convert signals [176–181]. The reference [182] provides a complete overview about this phenomenon. The output spectrum consists of well separated wave-packets, each composed of equally spaced laser lines, for the pump(s), signal and idler waves. This is illustrated in the sketch in Figure 4.1 (b), showing the general configuration of pulsed-FWM in the degenerate case. We will refer this situation as the pulsed extra-envelope configuration, because the new sidebands are generated outside the pump envelopes. In both CW-FWM and extra-envelop pulsed-FWM configurations, illustrated in Figures 4.1 (a) and (b), the new spectral components generated by FWM never overlap with the input pump envelops.

With the set-up developed in this thesis, we studied the case of *intra-envelope FWM* process, when the FWM components are generated within the spectral envelope of the input pumps. It occurs when the shift between the pump carrier frequencies is very small compared to their bandwidth and repetition rates, as illustrated in Figure 4.1 (c).

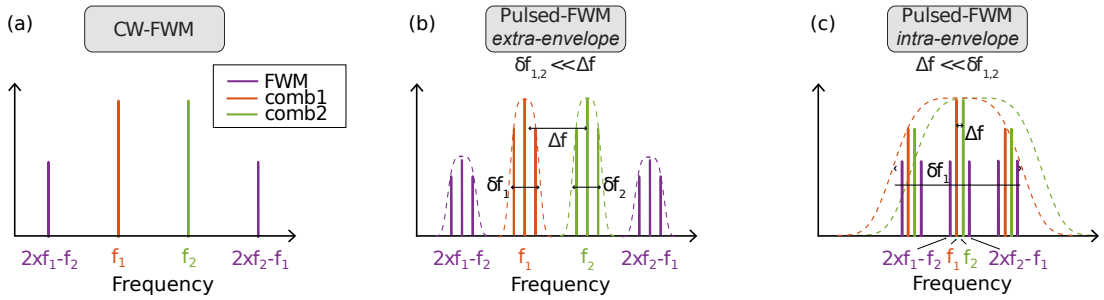

Figure 4.1: Scheme illustrating the different FWM configurations. (a) CW-FWM: two CW pumps generate 2 sidebands. (b) Extra-envelop pulsed-FWM: two pulsed pumps generate 2 sideband packets, well-separated of their spectral envelops. (c) Intra-envelop pulsed-FWM: two pulsed pumps generate 2 sideband packets within their spectral envelops.

Similarly to the case of extra-envelope FWM process [174, 183, 184], the dynamics of intra-envelope FWM can turn out to be complex to apprehend. In order to introduce the process, let's first describe the most simple configuration; which is two pulsed pumps, made of only two spectral lines each. They are separated by the repetition rate, which is the same for both pumps: $f_{rep1} = f_{rep2} = f_{rep}$. Let's assume that they also have the same amplitude A. In this simple case, the electric fields are respectively written $E_1 = A\left(e^{i2\pi f_1 t} + e^{i2\pi(f_1+f_{rep})t}\right)$ and $E_2 = A\left(e^{i2\pi f_2 t} + e^{i2\pi(f_2+f_{rep})t}\right)$ with $f_{1,2}$ the carrier frequencies of pump 1 and pump 2 respectively and $f_2 - f_1 = \delta f_p$ their difference. In our case, it is set by the AOMs used in the set-up: $\delta f_p = \delta f_{AOM1/2}$. We can calculate the nonlinear interactions between these waves during their propagation in a χ^3 media, as $E_{FWM} \propto |E_1 + E_2|^2 \cdot (E_1 + E_2)$:

$$
\begin{aligned}
E_{FWM} \propto\ & 4A^2(E_1+E_2) && \} c_1\\
& + 2E_1 \times A^2(e^{i2\pi f_{rep}t} + e^{-i2\pi f_{rep}t}) && \\
& + 2E_2 \times A^2(e^{i2\pi f_{rep}t} + e^{-i2\pi f_{rep}t}) && \} c_2\\
& + 2E_1 \times A^2(e^{i2\pi \delta f_{AOM1/2}t} + e^{-i2\pi \delta f_{AOM1/2}t}) && \\
& + 2E_2 \times A^2(e^{i2\pi \delta f_{AOM1/2}t} + e^{-i2\pi \delta f_{AOM1/2}t}) && \} c_3\\
& + E_1 \times A^2(e^{i2\pi (f_{rep}+\delta f_{AOM1/2})t} + e^{-i2\pi (f_{rep}+\delta f_{AOM1/2})t}) && \\
& + E_2 \times A^2(e^{i2\pi (f_{rep}+\delta f_{AOM1/2})t} + e^{-i2\pi (f_{rep}+\delta f_{AOM1/2})t}) && \} c_4\\
& + E_1 \times A^2(e^{i2\pi (f_{rep}-\delta f_{AOM1/2})t} + e^{-i2\pi (f_{rep}-\delta f_{AOM1/2})t}) && \\
& + E_2 \times A^2(e^{i2\pi (f_{rep}-\delta f_{AOM1/2})t} + e^{-i2\pi (f_{rep}-\delta f_{AOM1/2})t}) && \} c_5
\end{aligned}
\tag{4.1}
$$

Figure 4.2 (a) shows the modulus square of the spectrum of E_{FWM} calculated numerically by integrating the nonlinear Schrodinger equation (NLSE) [88] in a purely nonlinear fiber (see the caption for parameters). Red and green lines correspond to pumps 1 and 2 (100 MHz and 900 MHz and 200 MHz and 1000 MHz of respective optical frequency shifts to the pump carrier). Purple ones correspond to FWM lines. The two first teeth of pumps 1 and 2 (located at 100 and 200 MHz) are separated by $\delta f_{\mathrm{AOM1/2}}$ (100 MHz) as well as the second ones (located at 900 and 1000 MHz). The two first teeth of pumps 1 and 2 behave as two CW pumps and generate two side bands on both sides located at 0 and 300 MHz (purple lines), as in the basic CW-FWM configuration [88]. A similar mixing occurs between the two second teeth to generate sidebands at 800 and 1.1 GHz. Then two additional wave packets made of 4 new lines generated via mFWM interactions centered at -650 MHz and 1750 MHz are generated. All these lines correspond to frequency components that are predicted by Eq. (4.1), and shown by $c_{i\in[\![1\ ;\ 5]\!]}$ in Fig. 1 (a). Note that different combinations of the pump waves frequencies may give rise to the same frequency tooth. This is illustrated in Fig. 1 (a). For instance, the tooth located at 1.8 GHz has two contributions. It emerges from the two lines of pump 1 at respectively 0.2 GHz and 1 GHz interacting together, but also from the line 1 GHz of pump 2 interacting with the line at 0.1 GHz of pump 1. This simple example is a way to apprehend the overall dynamic.

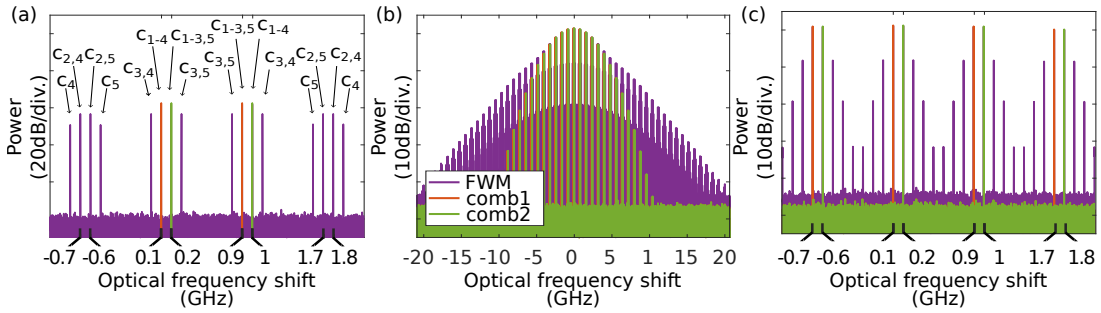

Figure 4.2: Numerics performed by integrating the NLSE. FWM between two frequency combs (a) made of 2 spectral lines, (b) made of 50 spectral lines corresponding to a pulse train of Gaussian with 50 ps pulse duration at FWHM. (c) Zoom on the mFWM packet structure of (b). Parameters : f_{rep}= 800 MHz, $\delta f_{\mathrm{AOM1/2}}$= 100 MHz, γ = 1/W/km, L= 100 m, and the peak power is 20 W.

A more realistic configuration involves two pumps composed of several lines, with a similar repetition rate but a slight offset frequency, as represented in Figure 4.2 (b) and (c). The pumps can be referred as frequency combs, depending on the number of spectral lines, their stability etc. It correspond to the simplified sketch of intra-envelop pulsed-FWM in Figure 4.1 (c). These are two pulse trains of Gaussian pulses of 50 ps at FWHM, whose spectra consist of about 50 lines separated of f_{rep} = 800 MHz. We computed the FWM between these two combs by integrating the NLSE [88] in the same fiber used for Figure 4.2 (a). As it can be seen in Figure 4.2 (c), each pair of closest comb lines of pumps 1 and 2 behaves as in the basic configuration illustrated in Figure 4.2 (a). They generate through FWM two new lines on each sides separated by the carrier

frequency difference between the combs ($\delta f_{AOM1/2}$= 100 MHz), as in the simple picture of CW-FWM. Harmonics are also generated from these four waves [184] to give birth to wavepackets made of 8 lines for each pair of closest lines of pumps 1 and 2. In addition, mFWM leads to the generation of new lines outside the initial spectra delimited by the envelops of pumps 1 and 2 as in the basic example illustrated in Figure 4.2 (a) (see purple packets at -650 and 1750 MHz). To summarize, FWM between two pulsed sources having the same repetition rate f_{rep} but slight different carrier frequencies δf_p leads to the generation of new spectral components mostly generated within the optical spectrum and located at $m \times f_{rep} \pm n \times \delta f_p$ around the carrier frequencies of the pumps with n,m integers.

However, the experimental evidence of this phenomenon is challenging because of the small frequency shift between all the generated lines lying in the MHz range, that is by several orders of magnitude smaller than the resolution of standard optical spectrum analysers. In the following, we demonstrate that the use of a third comb playing the role of a multi-lines local oscillator enables to isolate these new spectral components to highlight the intra-envelope FWM process.

Third comb as analysis tool

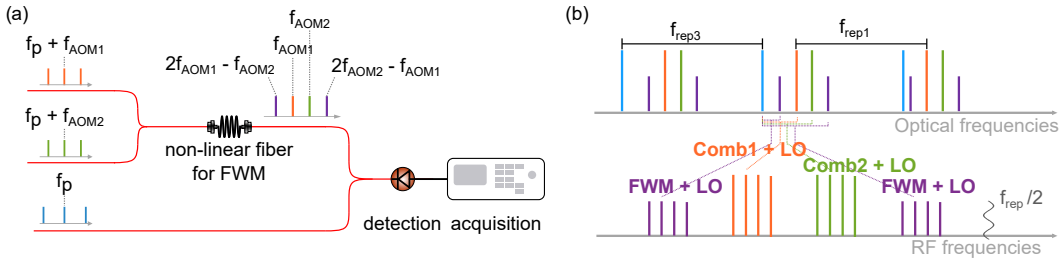

Figure 4.3: (a) and (b) Scheme of principle. Comb1 (orange) and Comb2 (green) at f_{rep1} generate FWM (purple) in a nonlinear fiber. Comb3 (blue) at $f_{rep3} = f_{rep1} + \delta f_{rep}$ down-converts the resulting spectrum in the RF domain.

Based on the idea of dual-comb spectroscopy, the mixing between the signal from the non-linear interaction between the two pump combs and another comb at repetition rate and carrier frequency leads to the down conversion of the optical spectrum into the RF domain [20].

In this work, there are two combs, operating at the same repetition rate, and with different carrier frequencies. These pumps will interact in a nonlinear fiber to generate new FWM components, within their input spectral envelops. We mix these combs with a third comb playing the role of the multi-lines local oscillator, as in dual-comb setups. This third comb source has a different repetition rate and carrier frequency compared to combs (pumps) 1 and 2. A simplified sketch illustrated the interactions between the three combs is represented in Figure 4.3 (a). We kept the same colors as in Figure 4.2 for comb 1 and 2 (orange and green respectively), and the FWM components (purple) and the third comb is represented in blue. As comb 1(2) and comb 3 have different carrier frequencies, the corresponding RF down converted

spectrum is centred at $f_1 - f_3 = \delta f_p = \delta f_{AOM1/3}$ ($f_2 - f_3 = \delta f'_p = \delta f_{AOM2/3}$), and reduced by the down-conversion factor a = $\frac{\delta f_{rep}}{f_{rep}}$, with $\delta f_{rep} = f_{rep} - f_{rep3}$. This is illustrated in Figure 4.3 (a), where the RF spectra corresponding to combs 1 and 2 (orange and green respectively) are well separated in the RF domain. About the FWM components, at first order they fulfill the basic FWM relation based on energy conservation which reads as $2f_1 - f_2$ and $2f_2 - f_1$ leading to down converted RF spectra centered at $2\delta f_{AOM2/3} - \delta f_{AOM1/3}$ and $2\delta f_{AOM1/3} - \delta f_{AOM2/3}$, and magnified by a $\frac{f_{rep}}{f_{rep} - f_{rep3}}$ factor. RF FWM components (purple) are thus isolated from pumps 1 and 2 RF spectra thanks to the down-conversion process. The use of a third comb therefore enables spectral resolution of the intra-envelop pulsed FWM phenomenon, which is experimentally implemented in the next section.

4.1.2 Experimental results

Experimental set-up

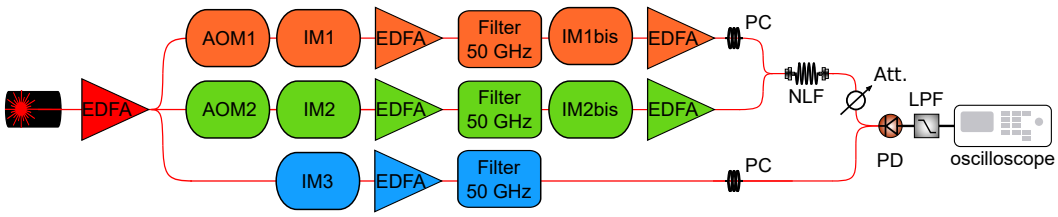

Figure 4.4: Scheme of the optical setup for the tri-comb generation. EDFA = erbium-doped fiber amplifier; AOM = acousto-optic modulator; IM = intensity modulator; PC = polarization controller; NLF = non-linear fiber, Att. = attenuator; PD = photo-diode; LPF = low-pass filter.

The set-up is detailed in Figure 4.4. It is the set-up described in Chapter 2, truncated before the expansion of the combs in the multi-core fiber. This initial stage serves as a preliminary step for the measurement with the expanded combs, described in Section 4.2. A second EDFA is used in channels 1 and 2 to increase the peak power up to 16 W (650 mW average power) to enhance the FWM efficiency in the non-linear $\chi^{(3)}$ medium. We used a fiber of L = 100 m length, with $\gamma = 1/\text{W/km}$, and $\beta_2 = 1\text{ps}^2/\text{km}$. The carrier of comb 1 and 2 are frequency shifted by using AOMs, of respectively 100 MHz and 200 MHz. The small bandwidth of the eo-comb sources provides a lot of freedom in the choice of parameters, since the constraints (similar to those stated in 1.3.2) are loose. The repetition rate is adjustable, and will be set at two different values to analyze the influence of the ratio between the repetition rate and the carrier frequency. The repetition rate difference between comb 3 and 1and 2 is $\delta f_{rep} = 1$ MHz, which is enough to avoid spectral aliasing in the RF domain. A first optical coupler combines comb1 and comb2 at the input of the non-linear fiber. A polarization controller is used to optimize the FWM signal from their superposition. A second optical coupler mixes the output signal with the LO (comb3). Another polarization controller enables to align their polarisations. We used a low pass-band

photo-detector (Thorlabs PDB480C, 5 GHz bandpass) to detect the resulting interference signal. The RF signal is low-pass filtered at $f_{rep}/2$ = 400 MHz using a low-band pass filter.

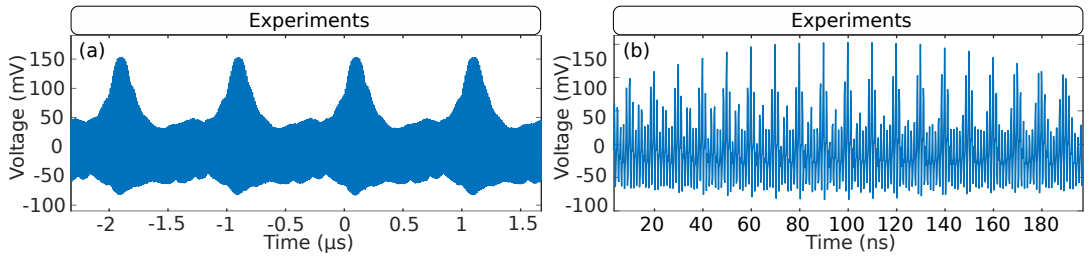

Figure 4.5: (a) Recorded interferogram over 4 periods at f_{rep} = 800 MHz and δf_{rep} = 1 MHz. (b) Zoom on the central burst.

Results at f_{rep} = 800 MHz

As demonstrated before, intra-envelop FWM from dual-pump leads the generation of spectral components located at m×f_{rep} ± n×δf_p around the carrier frequencies of the pumps with n,m integers. As first step, we choose f_{rep} so that it is a multiple of δf_p = 100 MHz, and such that the contributions around each packet at $n \times f_{rep}$ overlap. We set f_{rep} = 800 MHz in such a way as to have sufficient RF bandwidth [0 - $f_{rep}/2$] for the different RF packets. We recorded 800 interferograms on the oscilloscope at a sampling frequency F_S = 5 GHz and performed an averaging to increase the signal to noise ratio [20]. Figure 4.5 (a) shows few periods of the averaged interferogram. It shows a periodicity equals to the inverse of the frequency difference δf_{rep} = 1 MHz between comb 3 and combs 1 and 2. Figure 4.5 (b) is a zoom on the central burst, where one can notice the temporal scanning of the signal by the LO.

By calculating the Fourier transform of the interferogram, we obtained the down-converted spectrum depicted in Figure 4.6 (b). As expected, each packet is centered at its RF frequency offset with the LO: at 100 MHz, the linear beat between the LO and comb1; at 200 MHz, the linear beat between the LO and comb2; at 0 MHz, the beat between the LO and the low frequencies of the FWM; at 300 MHz, the beat between the LO and the high frequencies of the FWM. Thus, the use of a multi-lines local oscillator indeed enables to extract and isolate in the RF spectrum the FWM components hidden within the optical spectrum. Note that the wave packet located at 400 MHz emerges from the mFWM. These experimental results are in excellent agreement with numerical simulations depicted in Fig. 4.6 (a). From these RF spectra, it is possible to numerically reconstruct the optical spectra. The method is similar to the one of DCS, but applied to the several RF packets. It involves subtracting the center frequency of each packet and stretching the spectrum by the inverse of the magnification factor [7, 20]. This leads to the optical spectra centered at 193.4 THz in Figure 4.6 (c) and (d). They have a sinc-like shape. One can clearly see combs 1 and 2 (orange and green respectively), with the same repetition rate, and with a slightly different carrier frequency. The FWM bands are located on both sides of each closest

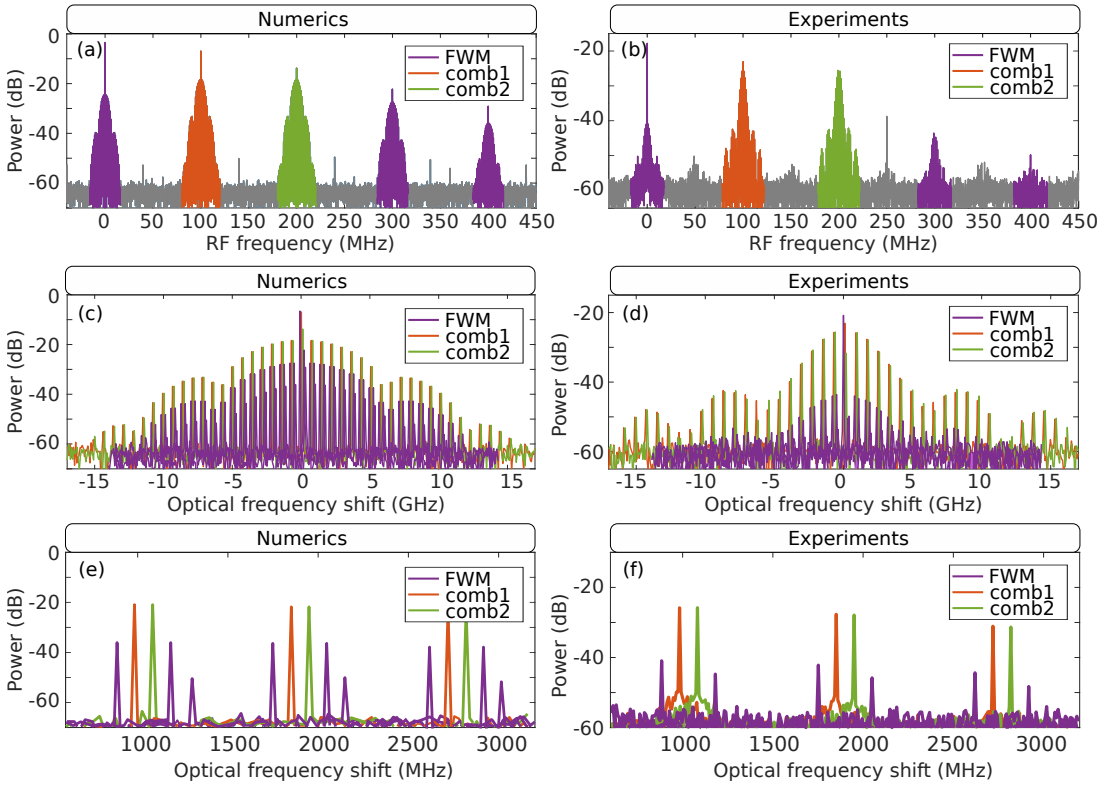

Figure 4.6: (a) Numerical and (b) experimental RF spectra of the interferogram. (c) Numerical and (d) experimental corresponding optical spectra. (e) Numerical and (f) experimental zoom on the mFWM packet structure of the optical spectrum.

lines pairs (purple), as expected in the simplified sketch of Figure 4.1 (c). The reconstructed optical spectra, showing the FWM component interleaved within the optical spectrum, are in excellent agreement with numerical simulations shown in Figure 4.6 (c) and (e). This agreement confirms the validity of our procedure to reconstruct the optical spectra and highlights the accuracy of the measurements.

Results at f_{rep} = 875 MHz

If f_{rep} is not a multiple of δf_{AOM}, the different FWM contributions located at $m \times f_{rep} \pm n \times \delta f_p$ (n,m integers, whose limit values depend on the degree of the nonlinear regime) do not overlap. In order to get into this configuration, we set f_{rep} = 875 MHz with δf_p = 100 MHz. We obtain an interferogram with a RF spectrum shown in Figure 4.7 (b). In addition to the contributions that were already there, there is a new RF spectral packet (dark blue) at 375 MHz which is seen experimentally and numerically. In the previous case, the spectral packets at 375 MHz and 400 MHz were superimposed. This separation is accompanied by a decrease in their respective SNR. Moreover, the experimental noise level of the RF spectrum increases, which could be due to the

fact that the sampling frequency of the oscilloscope Fs = 5GHz is not a multiple of the repetition frequency f_{rep} = 875 MHz. The relative amplitudes are less in agreement with the simulations, and one of the origins of that is potentially the inadequate sampling.

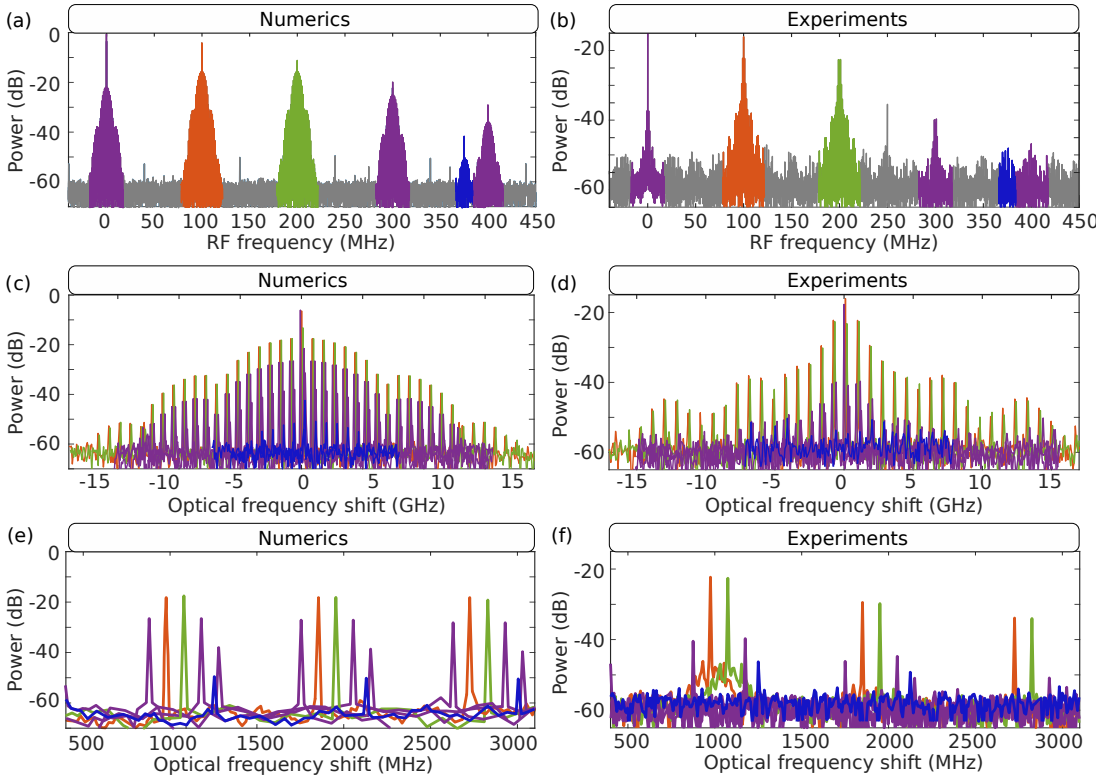

Figure 4.7: Experiment (left) and simulation (right) for intrapulse mFWM in the case of idlers not overlapping (f_{rep} not multiple of δf_{AOM}). (a) and (b) RF spectrum from multi-comb spectroscopy. (c) and (d) Optical spectrum. (e) and (f) Zoom on the mFWM packet structure.

By carefully adjusting the parameters of the two comb sources, and paying particular attention to the ratio between the comb spacing and the carrier offset, one can tailor the spectral structures from mFWM. The overall good agreement between experimental and numerical results demonstrate multi-comb interferometry to be a powerful tool for the characterization of non-linear effects.

Phase measurement

Multi-comb interferometry is a technique that also allows to measure the phase of the signals under study. Figure 4.8 displays experimental (left side) and numerical results for the 2 linear signals at 100 MHz and 200 MHz of optical frequency shift (upper part) and for the 2 first order FWM signals (lower part). In each case is plotted the second-order phase, i.e. the phase from which the linear component has been removed.

The phase of the signals at 100 MHz and 200 MHz is overall flat, in addition to the phase jumps around the optical frequency shifts of 5 and -5 GHz. These components mainly derive from the pump signals, which have a flat phase profile with phase jumps at the local minima of the spectral envelope (shown on the grey background). It corresponds to the modulation of pump intensity by 50 ps square wave signals.

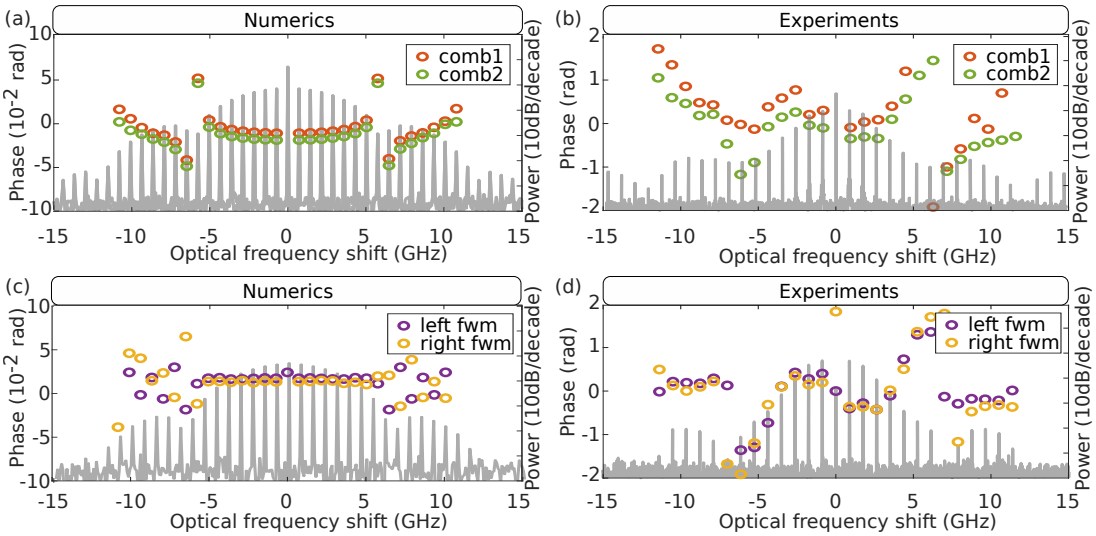

Figure 4.8: Experiment (left) and simulation (right) of the spectral phase for (a) and (b) pump waves, (c) and (d) idler waves.

The phase profile of the newly generated signals is a combination of the phases of the signals involved in their generation. In the case of the experimental results, the zones around -5 GHz and +5 GHz deviate from the simulations, explained by a decrease in SNR in these zones. However the left and right FWM contributions' phase profiles coincide. The big discrepancy of 10^{-2} radians between numerics and experiments could be attributed to too much instability in the experimental setup. The current state of results does not allow a conclusive answer to non-linear phase measurement by the tri-comb system, and requires further research after an improvement of the stability of the set-up (see Perspectives).

4.2 Tri-comb interferometry with the broaden combs: 2D FWM spectroscopy

As presented in Section 1.4, MDCS is an advanced spectroscopy technique that would tremendously benefit from multi-comb interferometry. Because it is a technology free from mechanical components, it enables rapid acquisition of complex multidimensional spectra in less than half a second. To appreciate the significant leap in spectral resolution achieved through frequency combs in MDCS, the reader is invited to consider the section 6.5 of reference [31], that com-

pares the acquisition time and spectral resolution of several techniques for MDCS. Traditional techniques, reliant on mechanical scanning delay stages, typically necessitate longer acquisition times as spectral resolution increases. This relationship results in a constant figure-of-merit, where lower values indicate proportionally shorter acquisition times. Most conventional methods [144, 145, 185–190] exhibit a figure-of-merit falling between 10^{13} and 10^{14}. In contrast, both comb-based MDCS [151] and tri-comb spectroscopy [28] offer a remarkable improvement in spectral resolution of over an order of magnitude without necessitating longer acquisition times. Specifically, comb-based MDCS enhances the figure-of-merit by nearly 100, while tri-comb spectroscopy raises it by roughly 20,000.

With the development of coherent tri-comb sources, TCS can become a device for field-deployable measurements beyond the laboratory. In the following section, we use the tri-comb setup in a 2D FWM spectroscopy experiment to demonstrate its potential as a real-time high-resolution imaging system.

4.2.1 Tri-comb interferogram

The intra-envelop FWM measurements with the electro-optical combs serve as a preliminary step to study the interaction between the three broadened combs. High mutual coherence is what preserves the teeth linewidth of the FWM signal, that can be directly related to the accuracy of the tri-comb measurement [151]. In order to demonstrate that the three-comb light source developed in this work could be implemented for non linear spectroscopy, we performed a proof of concept of FWM spectroscopy. The experimental set-up is similar to the one presented in Figure 4.4, with the exception of the comb sources being at the output of the tri-core fiber. First, we adjusted the set-up presented in Chapter 2 to obtain a flat spectrum, with a good optical SNR, on all three channels. The optical bandwidth is around 250 GHz. We took advantage of the flexibility of the system to set the repetition frequency at f_{rep} = 1.25 GHz in order to have enough RF bandwidth for both linear and non-linear contributions. The dynamics of the mFWM is not what is studied here, and only first-order sidebands are considered. The relationship between f_{rep} and δf_p is therefore of little importance. The difference of repetition rate δf_{rep} is set at 100 kHz to avoid any overlap between the spectral packets. Once again, in this proof of principle, we used a non-linear fiber as χ^3 nonlinear medium. We used the AWG interfaces to tune the timing of the RF pulses, in order for comb 1 and comb 2 to be synchronous at the entry of the non-linear (mono-core) fiber. The output signal is then attenuated and recombined with the third-comb. Two controllers are used to align the three waves' polarization. The signal is detected with a PD (Thorlabs PDB480C, 5 GHz bandpass) and then low-pass-filtered at 500 MHz.

Figure 4.9 shows the obtained RF spectra when (b) the pumps do and (a) do not overlap (with a separation of 100 ps, superior to the 50 ps pulse duration). As expected the pumps spectra are centered at 100 MHz and 200 MHz, the frequency shifts between Combs 1 and 2 and the LO, respectively. The generated FWM bands are centered at 0 MHz and 300 MHz, and appear depending on whether the pumps temporally overlap or not. In both cases, there

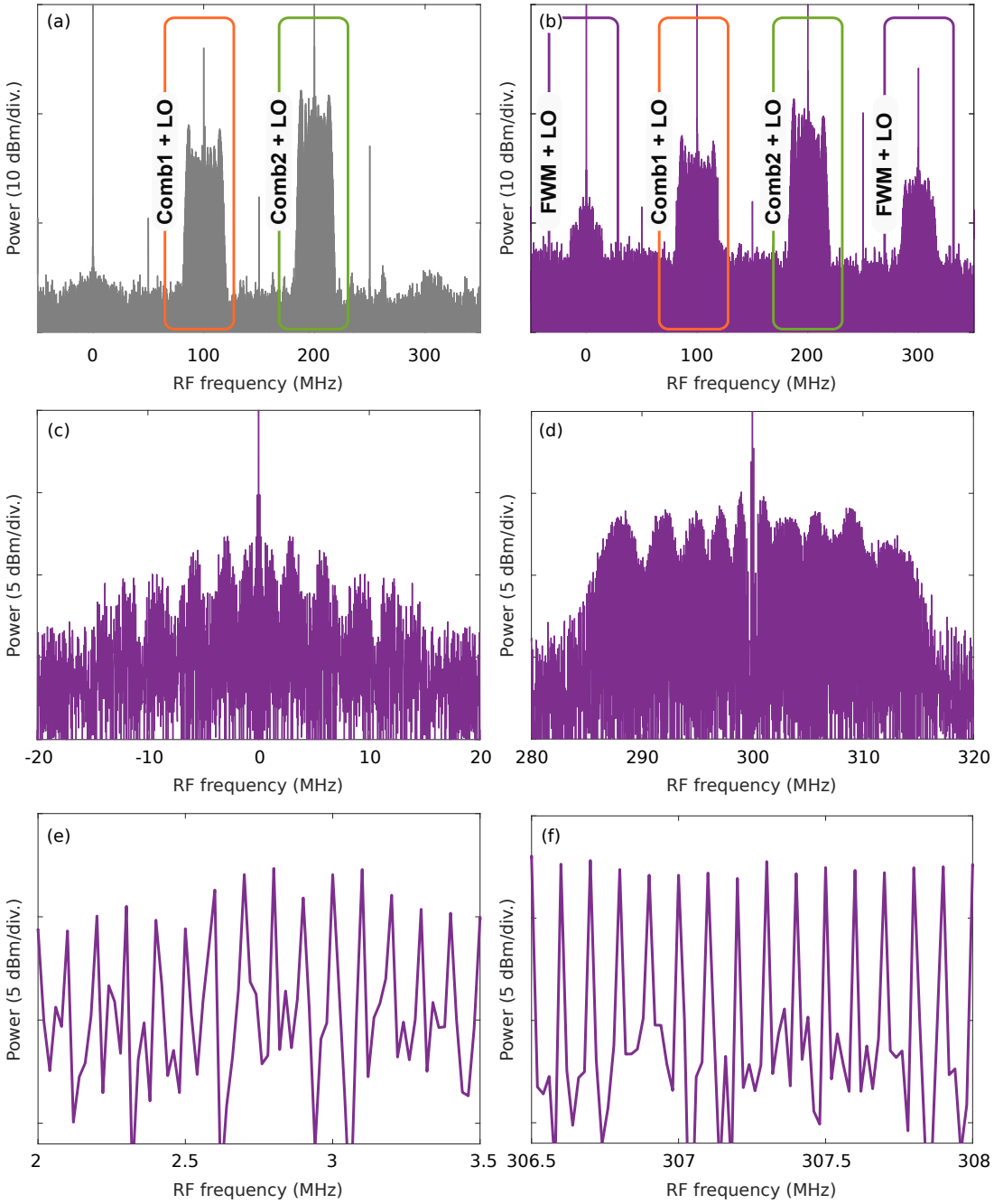

Figure 4.9: (a) RF spectrum of a set of n = 5 interferograms averaged over N = 800 times, when the pumps do not overlap. (b) when the pumps overlap (c) Zoom on the left FWM sideband at 0 MHz, with n = 10 and N = 80. (d) Zoom on the right FWM sideband at 300 MHz. (e) Zoom on the comb lines of the left FWM sideband. (f) Zoom on the comb lines of the right FWM sideband. Parameters: f_{AOM1} = 100 MHz and f_{AOM2} = 200 MHz, δf_{rep} = 100 kHz, f_{rep} = 1.25 GHz and $F_{sampling}$ = 5 GHz. FWM = Four-Wave Mixing.

is a strong DC component, due to the interference between two or more waves. The spectral width of the linear contributions is about 20 MHz which indeed corresponds to the 250 GHz width in the optical domain. The conversion is made by using the magnification factor $1/a = f_{rep}/\delta f_{rep} = 12500$. The width of FWM sidebands is similar as they result from the nonlinear mixing between Comb 1 and Comb 2, as presented on the zoom in Figure 4.9 (c) and (d). The down-shifted FWM signal presents a spectrum that is not representative of the multiplication of the 3 combs' envelops, and with a smaller SNR than its up-shifted equivalent. That is explained by the fact that the negative-frequencies components and the positive-frequency components overlap around 0 MHz. This problem can easily be overcome by adaptating the AOMs to higher frequency-shift values (at 200 MHz and 300 MHz, for example). A closer zoom in Figure 4.9 (e) and (f) shows a clear comb-like structure with a tooth-to-tooth separation equal to the repetition rate difference between the pumps and the LO ($\delta f_{rep} = 100$ kHz). This demonstrated the high coherence between the three combs.

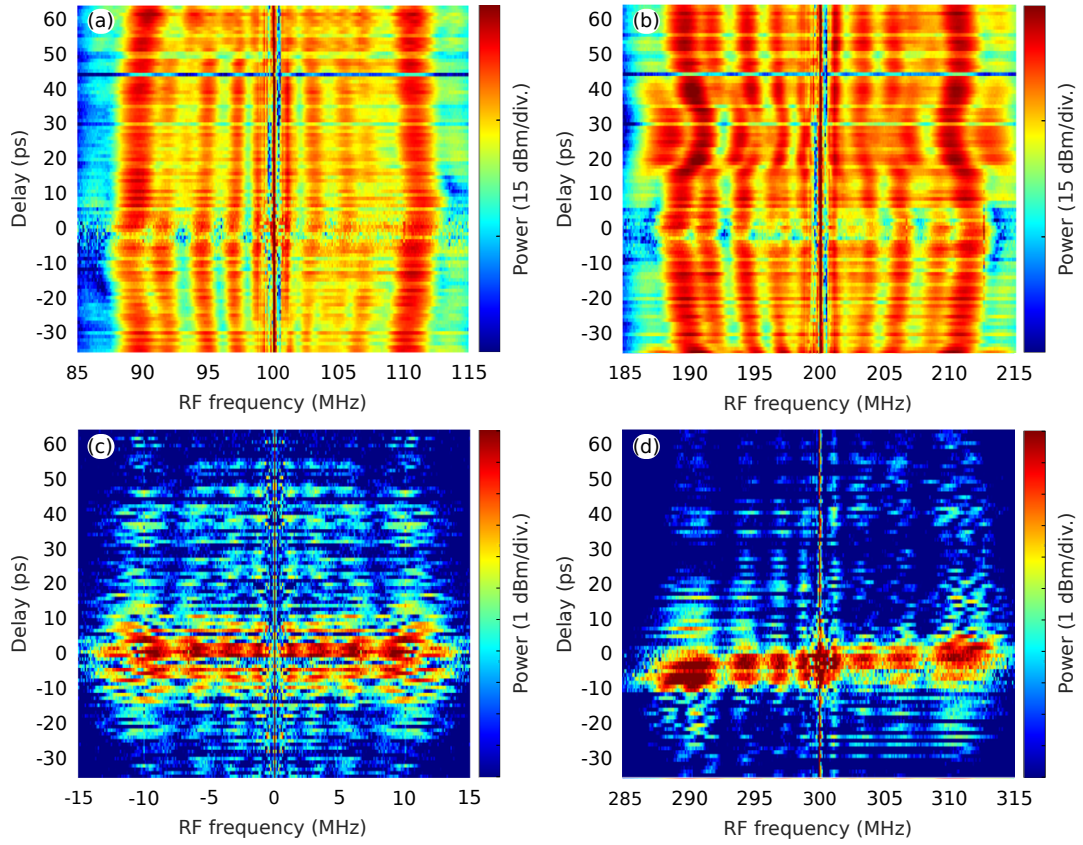

Figure 4.10: Spectrogram of the envelop of the FWM components. (a) Linear spectrum centered at 100 MHz. (b) Linear spectrum centered at 200 MHz. (c) FWM spectrum centered at 0 MHz. (d) FWM spectrum centered at 300 MHz.

Once converted into the optical domain, the tri-comb measurement allows the spectra of

each contribution (linear and non-linear) to be reconstructed with a high resolution set by δf_p.

4.2.2 Tri-comb spectrogram

As presented in the first chapter, the evolution of the FWM signal as a function of the pumps delay is of great interest in multidimensional spectroscopy [31, 151]. We have plotted the spectro-temporal evolution of the envelops of all four spectral packets in Figure 4.10. This was achieved by scanning the delay between the RF pulses, using the AWG interfaces. For each 1ps-step an interferogram was recorded. The use of eo-optical combs controlled by RF signals therefore ensures once again a great ease of use. The first row of Figure 4.10 depicts the two linear spectra, whose amplitude does not depend on the temporal overlap of the two pumps. We can observe the temporal evolution of the SPM spectrum of combs 1 and 2, whose envelope remains relatively stable. The second row of Figure 4.10 depicts the two FWM spectra, whose amplitude depends on the temporal superposition of the two pumps. For a large delay relative to the pulse duration (55 ps), no sideband component is generated. However, we observe a clear FWM signal when the two pumps temporally overlap. The four spectrograms show intensity modulations due to those of the pumps and LO originating from the SPM effect.

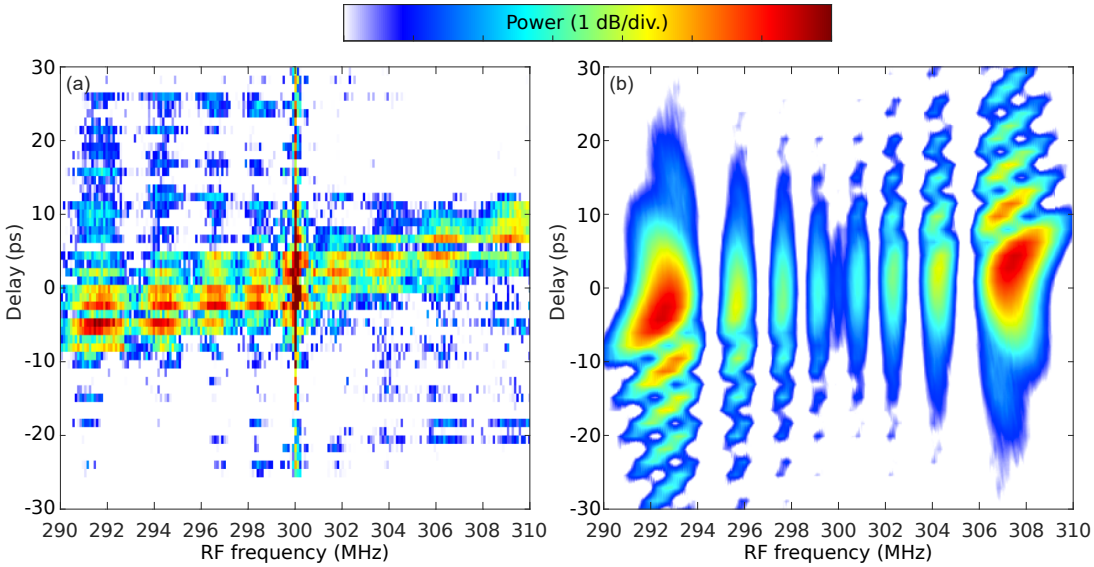

Figure 4.11: Envelop of the spectrogram of the FWM component centred at 300 MHz. (a) Experimental results. (b) Numerical simulations.

In the case of the up-shifted FWM component, centered at 300 MHz, there is a chirp of 0.5 ps/MHz in the RF domain, originating from the chirp of the combs (still due to the SPM effect). This observation is confirmed by zooming in on the signal at 300 MHz and comparing it to numerical simulations, as presented in Figure 4.11. The numerical simulations were made by Arnaud Mussot. To reduce computational time, we neglected the linear loss in the tri-core fiber

and fairly assumed that SPM is the dominant effect. In this way, we calculated the spectra at the tri-core fiber output by simply considering the nonlinear operator. The continuous residues of the pump were not taken into account in the numerical simulation of the combs, leading to spectra without the central peak that we experimentally observe. We then computed the FWM between the two pump combs by integrating the NLSE in a highly nonlinear fiber (peak power 5 W, L = 300 m, $\beta_2 = 1 \times 10^{-28}$ ps²/km, and $\gamma = 10$ /W/km), and then calculated the interferogram with the third comb. This comparison with numerical simulations confirms the origin of the chirp. We do not observe it for the down-shifted FWM spectrum because at 0 MHz, the components of positive and negative frequencies overlap. A simulation of the entire RF domain, with the same parameters as cited below, in Figure 4.12 validates this asymmetry and the experimental results presented in Figure 4.10.

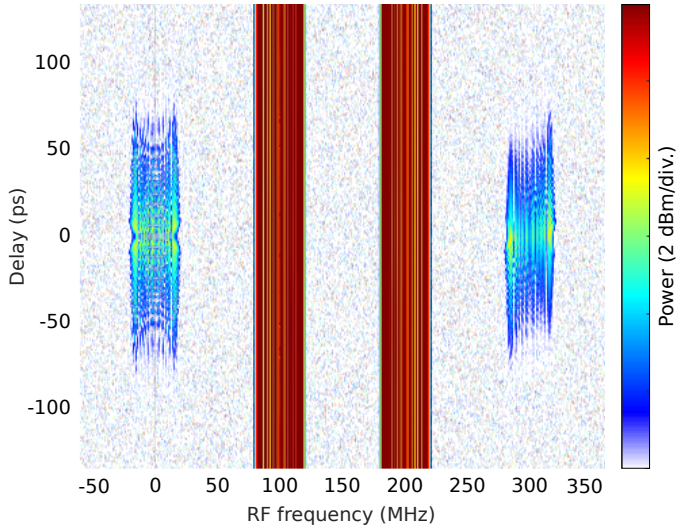

Figure 4.12: Numerical simulation of the envelop of the spectrogram over the whole RF bandwidth.

4.3 Conclusion

In this chapter, the developed set-up is used for tri-comb applications.

As first step, we used the eo-combs. We reported the first numerical and experimental observation of intra-envelope FWM in optical fibers. We showed that two wave packets with almost the same carrier frequency and similar repetition rates can interact non-linearly to generate new FWM components located within their spectra, and only shifted from RF frequency shifts from the spectral lines of the pumps. We demonstrated the use of a third comb acting as a multi-lines local oscillator to extract and isolate these FWM components in the RF domain. From these measurements, we showed that it is possible to reconstruct the optical spectra, and

analyzing the phenomenon with a very good spectral resolution. These observations would not be possible with standard optical spectrum analyzers due to their limited spectral resolution. The very good agreement between experimental and numerical results demonstrates that multi-comb interferometry can be a powerful tool for finely characterizing advanced nonlinear effects. In our case, the cores are not coupled and their non-linear interaction is ensured independently of the spectral broadening in the tri-core fiber. However, it is possible to exploit spatial multiplexing to study the FWM as a function of its distribution in different cores of the same fiber [191].

As a final step, the mutual coherence between the three broadened combs was illustrated within the same FWM spectroscopy configuration [151]. The FWM sibands are made of clearly defined spectral lines, separated by the repetition rate difference between the pumps and the multi-line local oscillator. The conversion efficiency in addition to the conservation of the frequency comb structure reveals the high mutual coherence between the combs. This all-fiber and frequency agile configuration offers an interesting alternative to cavity-based solutions where the parameters are fixed by the resonator and could open the way to new applications in ultrafast multidimensional frequency comb spectroscopy [192].

Conclusion

The field of multi-comb interferometry has seen significant advancements since the initial theoretical and experimental work carried out in 2002 [18] and 2008 [45]. Technological progress has led to increasingly efficient setups, paving the way to numerous applications. However, the feasibility of these experimental setups largely depends on their compactness and portability, as well as their flexibility. In this regard, the generation of frequency combs through electro-optic modulation of a continuous laser has proved to be highly advantageous. This approach relies on all-fiber optical components and electronics from the telecommunications industry, which are known for their robustness and reliability [25]. However, the counter-part is their small bandwidth. Depending on the intended application, a multi-comb measurement may require a wide spectral span. To achieve this, it is possible to harness non-linear effects to broaden the spectrum of electro-optical comb sources. To date, multi-comb architectures have been developed with the aim of equalizing the optical path of each comb to optimize their mutual coherence. While these systems have proven their effectiveness, they are still limited to dual-comb spectroscopy, which is a linear sampling technique. The advancement of FWM spectroscopy would greatly benefit from a coherent tri-comb fiber system, offering flexibility in spectral bandwidth, acquisition speed, and resolution. The ability to adjust the repetition rate is particularly advantageous, as it can be used to adapt sampling to the desired measurement. This is the idea behind compressive sensing signal processing, a technic that enables to take benefit of the sparcity of a signal, combined to a reconstruction algorithm, to reduce the data point still checking the Shannon limit [193–195]. The gains in speed, sensitivity reported for dual comb spectroscopy or ranging could be applied to tri-comb interferometry, thanks to a frequency-agile tri-comb system. It is the technology presented in this manuscript.

To achieve this, we exploited the transverse dimension of optical fibers, through spatial multiplexing of frequency combs. We fabricated a nonlinear tri-core fiber, in which three narrow EOM combs originating from a single ultra-stable CW laser are broadened by SPM [88]. We obtained a spectral width of 1 THz at the output of each core, which corresponds to over 1500 laser lines at a repetition rate of 0.5 GHz. The output pulse energy is 0.3 nJ and we demonstrated they can be efficiently compressed to about 1 ps pulse duration. We measured a high degree of mutual coherence between any comb pair up to 50 ms, which allowed us to record interferogram spectra with an SNR greater than 20 dB. That enabled us to measure the absorption of a FBG

and the dispersion of a 20-meter-long SMF, as a demonstration of the efficiency of the dual-comb interferometer.

The mutual coherence between the three combs was illustrated by an FWM spectroscopy experiment [151]. Two frequency combs, acting as pumps, have been mixed into a $\chi^{[3)}$ medium, to generate new sidebands by FWM. All the spectral components, intermingled in the optical domain, can be retrieved in the RF domain by using a third comb that plays the role of a multi-line local oscillator. Using that scheme of fine optical detection with the three eo-combs, we reported the first numerical and experimental observation of intra-envelope FWM in optical fibers. This would not be possible with standard optical spectrum analyzers due to their limited spectral resolution. The very good agreement between experimental and numerical results demonstrated that multi-comb interferometry can be a powerful tool for finely characterizing advanced nonlinear effects in the spectral domain. We then applied this tri-comb scheme with the three broadened combs. The FWM bands are made of clearly defined spectral lines, separated by the repetition rate difference between the pumps and the LO. The conversion efficiency, in addition to the conservation of the frequency comb structure, reveals the high mutual coherence between the three combs.

This all-fiber and frequency-agile configuration offers an interesting alternative to cavity-based solutions where the parameters are fixed by the resonator and could open the way to new applications in ultrafast multidimensional frequency comb spectroscopy [151]. The versatility of the frequency comb-based EOM technology allows to control the repetition rate of the sources easily. We have reported three combs, but there is no technical limitation to increasing their number, e.g., four combs or more. This could be helpful to 2DS experiments [134] where 3 variables are scanned at the same time thanks to 4 pulse trains (see Figure 1.15). In addition, the concept of spatial-division multiplexing to generate multiple coherent frequency combs can be extended to other wavelength ranges, where standard rare-earth fiber amplifiers are available (1 or 2 µm). It is also possible to use Bi-doped fiber lasers and optical amplifiers in the 1150 to 1550 nm spectral region [196]. Alternatively, mutual coherence preserving frequency conversion systems can be implemented to reach the mid-infrared or infrared or even visible regions based on nonlinear fiber [197] or PPLN systems [198].

Perspectives

Outline of the current chapter

The overall system analysis highlighted a number of areas for improvement for spectroscopic applications, which are relatively accessible in the short to medium term.

Shorter pulses

Performances in terms of spectral width can be improved by replacing the intensity modulators in our scheme by a cascade of intensity and phase modulators [25]. Using this architecture, broadband spectra spanning ten's of terahertz corresponding to ultrashort pulses of a few tens of femtoseconds can be generated in single core fibers [165, 199] and could be transposed in tri-core architectures.

To further illustrate this statement, Alice Houard, Master student of ULB, carried out a similar experiment using the equipment available in the laboratory during her Master internship. We drove 2 PMs and an IM at 10 GHz to generate 8 ps pulses, amplified them and injected them into a normal low-dispersion fiber. The output spectrum is shown in Figure 4.13, with an average output power of 36 dBm (4 W). It spans 20 nm (2.5 THz) with excellent SNR. These results could be improved to reach the state of the art [165], which demonstrates a frequency comb extending over 100 nm (12.5 THz) with a repetition rate of 25 GHz. It could be done notably by using phase modulators with a lower V_π (here 9V and the best equipment is 3 V at 10 GHz), more powerful RF amplifiers, and higher non-linear fibers (here we used a standard DSF, a gain of a factor of 5 could be achieved by using an HNLF). With one or more of these improvements, it would be possible to obtain spectra larger than 10 THz.

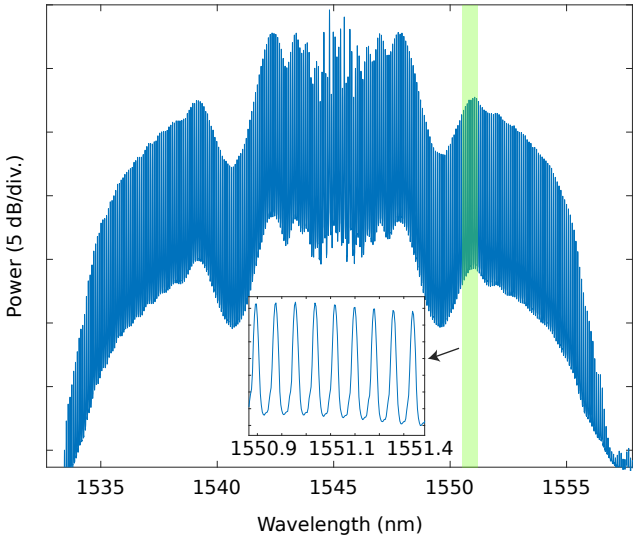

Figure P.1: Spectrum of a frequency comb at 10 GHz repetition rate, from cascaded EOMs and broadened in a DSF. EOM = eletro-optic modulators; DSF = dispersion shifted fiber.

Flatter spectra

SPM is a non-linear phenomenon leading to spectral broadening, which has the particularity of operating in the normal dispersion regime. This enables to avoid disturbances such as soliton fission and thus ensures a greater stability of frequency combs. However, SPM induces strong oscillations at the high end of the spectrum, which can be detrimental because the signal then exhibits high contrast. This high contrast may not be suitable for certain applications, if a high constant SNR is required across the entire spectrum for instance. In the normal dispersion regime, it is possible to overcome this contrast limitation by leveraging the phenomenon of shock waves. In this regime, the material's dispersion and non-linearity combine to create an extreme steepening of the pulse envelope slopes [88], which then regularizes itself by oscillating at its edges. The spectrum becomes flatter, resulting in much lower contrast compared to when broadening is achieved through pure SPM [200, 201].

Figure 4.14 illustrates the temporal profiles (a) and spectral profiles (b) obtained under conditions similar to spectral broadening by Self-Phase Modulation (SPM) in a three-core fiber, but for different values of β_2 (the actual value $\beta_2 = 2.10^{-27}$ ps^2/km, the value of a dispersion-compensating fiber $\beta_2 = 1.10^{-25}$ ps^2/km, and an intermediate value $\beta_2 = 5.10^{-26}$ ps^2/km). In the case of low dispersion (blue curve), the temporal profile remains almost unchanged. As dispersion increases (orange curve), the slope of the pulse's edges tends to diverge. To avoid a discontinuity, the pulse self-regulates by creating oscillations on its edges (purple curve). In the spectral domain, this results in a flattening of the spectrum. This flattening effect could be used to improve the tri-comb set-up by designing a tri-core fiber with higher dispersion.

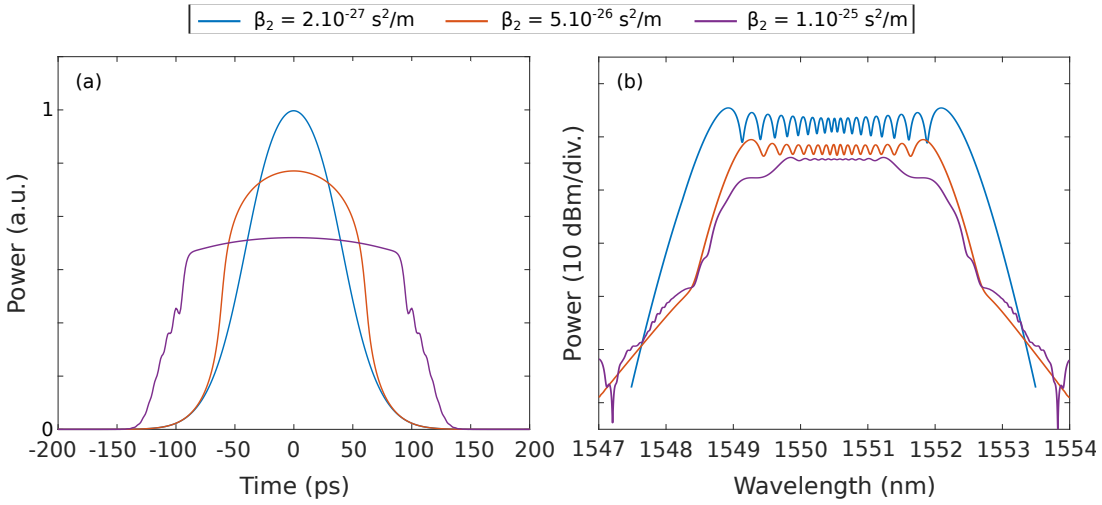

Figure P.2: Numerical results of NLSE integration at the output of a fiber with parameters similar to the ones of the tri-core fiber, while varying the dispersion value (under normal dispersion regime and neglecting losses). (a) Temporal profiles at the output. (b) Optical spectra of the output. Parameters: Input pulses with a Gaussian profile of 50 ps duration, having an average power of 350 mW at f_{rep} = 500 MHz, propagating in a 1 km fiber with γ = 5 W/km.

Higher stability

The study of the coherence of pairs in the tri-comb system has revealed a limitation in stability across the three electro-optical paths preceding spectral broadening. Before seeking to enhance the performance of the tri-core fiber, it is necessary to enhance the coherence of the three electro-optical chains. One potential avenue in this direction is the synchronization scheme of the three AWGs driving the EOMs. As a reminder, in the work presented in this manuscript, the same method is always employed to generate the difference in repetition frequency between two combs. Both output ports (adjustable clock and reference at 10 MHz) of the same RF frequency generator are used. The AWG in the first channel generates its internal clock at 12.5 GHz based on the reference, while the AWG in the second channel directly uses the clock signal at 12.5 GHz + δf_{clock} from the generator. The way it works is detailed in section 2.1.1. This technique allows for generating a difference in repetition frequency as small as desired without modifying the bit vectors of the AWGs. However, it imparts a lower relative stability level among the AWGs compared to a configuration where all three devices directly share the same clock.

This is demonstrated by a measurement of the phase noise of the RF beat between the outputs of the 2 AWGs, made by Debanuj Chatterjeee, the post-doc who takes over the set-up. The results are shown in Figure 4.15. Configurations using the generation of the internal clock of one (dark blue curve) or both (light blue curve) from the 10 MHz reference exhibit very similar phase noise. The curve where both AWGs directly share the same clock shows an improvement in stability in the 1 Hz - 1 kHz domain. Therefore, this would be a readily implementable

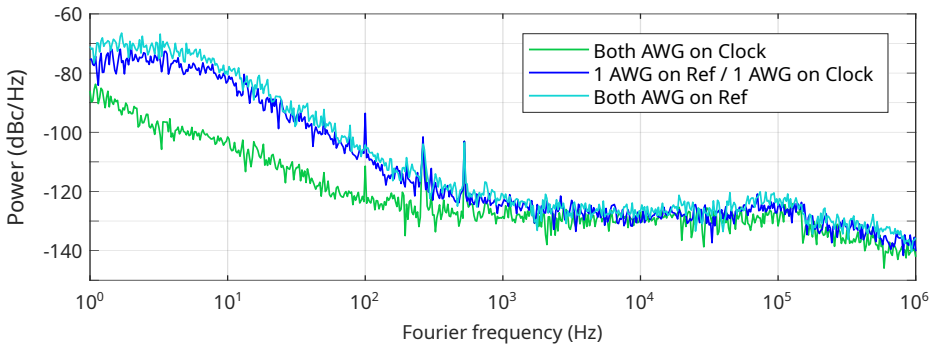

Figure P.3: Comparison of the AWG configurations: phase noise of the beating between the RF outputs.

enhancement for the mutual coherence of comb pairs. Another possibility would be to use three adjustable, phase-locked clocks [199], which is commercially available with a sub-picosecond channel-channel stability (see Holzworth synthetizers' catalog for example). To confirm this improvement path, we repeated the coherent linewidth measurements presented in section 3.1.2, comparing the configurations "combs on ref/clock" and "both on clock." Figure 4.16 presents the results obtained at the output of the EO chain (a), after the broadening in two cores of the tri-core fiber (b), and after the broadening in two independent NZDSF on the same spool (c). In all three cases, the configuration with a common clock results in a narrower beat peak and thus better mutual coherence of the comb pair. It is therefore sufficient to adjust the generation of the RF signals to improve the relative stability of the three electro-optical paths and, consequently, the overall system.

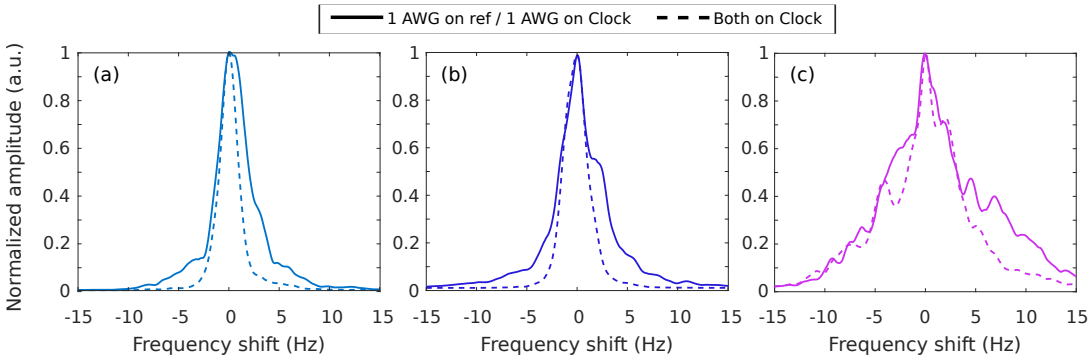

Figure P.4: Comparaison of the AWG configurations: coherent linewidth of the pairs of combs at (a) the output of the eo chain, (b) the output of the tricore fiber and (c) the output of two independent NZDSF on the same spool. NZDSF = non-zero-dispersion-shifted fiber.

Once the limitation of the mutual coherence by the EO stage is overcome, it is conceivable to improve it by optimizing the design of the multi-core fiber. The primary adjustable parameter is the core separation. In this work, it was set at 30 µm to ensure there is no cross-talk between the

cores and to facilitate the fabrication of the FANs. However, as the core separation decreases, the phase noise degradation caused by external perturbations of the light beams propagating in each core would become increasingly symmetrical, resulting in an enhancement of mutual coherence. The practical limitation would be determined by the cross-talk that might occur if the cores are positioned too closely together and/or by the technical constraints of fan fabrication. Another option is to twist the fiber during the fabrication process to achieve nearly identical average perturbations for the beams, which is something that was explored in Section 3.2.

2D scanning

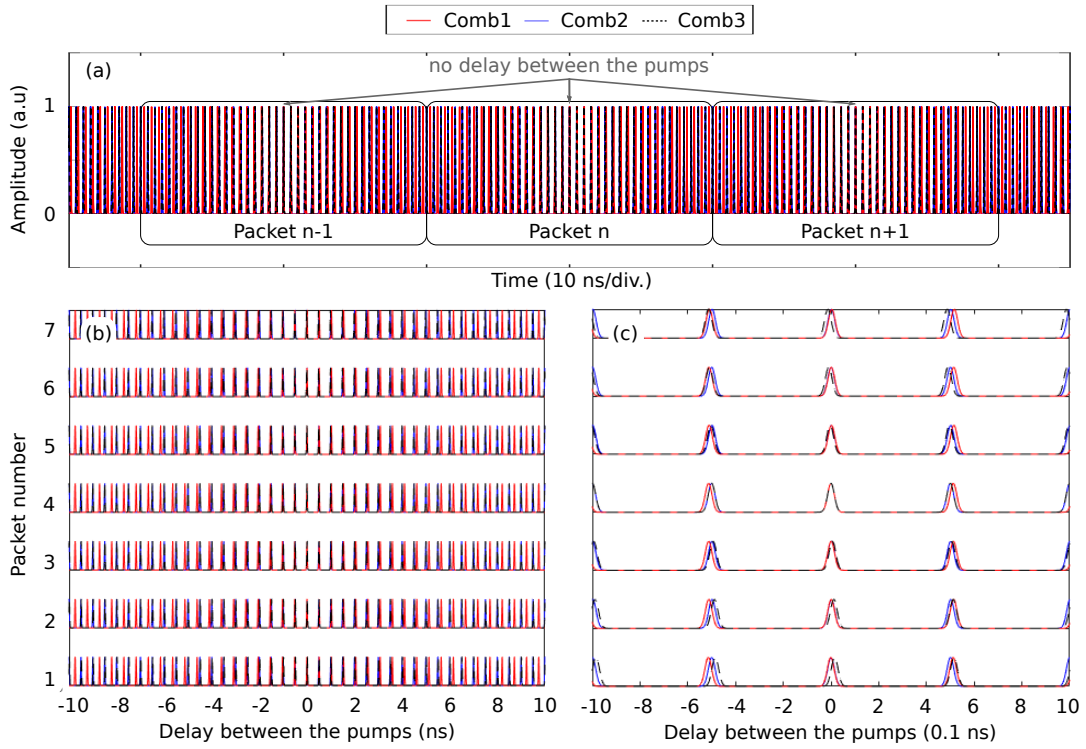

Figure P.5: Temporal evolution of the beating between three combs at three different repetition rates (a) globally, (b) sorted by packets of $f_{rep1}/\delta f_{rep3} = 100$ and (c) zoomed to show the sampling by the LO at each value of the delay between the pumps.

The objective of this thesis work is the generation of a coherent tri-comb system, entirely fiber-based and frequency-agile. By using the setup for a proof-of-concept demonstration of tri-comb interferometry (see Section 4.2), we demonstrated the potential of such an architecture for 2D spectroscopy and the detailed study of nonlinear phenomena. However, the full power of the setup is not exploited, as the temporal scanning is performed "by hand" using a module in the AWGs interface. This scanning involves recording an interferogram and calculating its Fourier

transform for each value of the delay between the two pumps. It is possible to replace this with a purely optical method by also shifting the repetition frequencies of the two pumps [146]. Similarly to the Vernier effect of DCS, the slight asynchrony of the combs causes a temporal shift at each pulse iteration. The significant difference from DCS is that this pump-to-pump shift occurs simultaneously with the sampling by the LO, as all three combs have different repetition frequencies in this configuration. Therefore, detecting the signal resulting from tri-comb interferometry using a photodiode enables the recording of an interferogram where two variables vary simultaneously. Thus, additional post-processing (compared to DCS) is required.

To illustrate this phenomenon of simultaneous shifts, we simulated the temporal evolution of the overlap of three combs, where f_{rep1} = 2 GHz, $f_{\text{rep2}} = f_{\text{rep1}} + \delta f_{\text{rep1-2}}$ = 1.999950 GHz, and f_{rep3} = 0.01 x f_{rep1} = 20 MHz. Every $1/f_{\text{rep1}}$, the two pumps shift by $\Delta T = \delta f_{\text{rep1-2}}/f_{\text{rep1}}^2$. Every $1/f_{\text{rep3}}$, the LO samples the overlap of the two pumps at a fixed delay value between them. This can be observed by segmenting the temporal vector into packets of $f_{\text{rep1}}/f_{\text{rep3}}$, as shown in Figure 4.17. Therefore, the task is to reorganize the interferogram resulting from the tri-comb overlap into a matrix where the x-axis corresponds to a delay scan between the two pumps, and the y-axis corresponds to sampling of the overlap by the LO. Implementing this post-processing step would provide a significant time-saving advantage, leading to improved stability and precision compared to the current "by hand" delay-shifting approach.

The upper sections list the short-term and medium-term modifications we think would upgrade the tri-comb set-up for non-linear spectroscopic applications. To conclude, the performances presented in this manuscript are a demonstration of its functionality, for which there are still so many areas for improvement.

Bibliography

[1] T. H. Maiman. "Optical and Microwave-Optical Experiments in Ruby". In: *Phys. Rev. Lett.* 4 (11 June 1960), pp. 564–566. DOI: 10.1103/PhysRevLett.4.564. URL: https://link.aps.org/doi/10.1103/PhysRevLett.4.564.

[2] A. L. Schawlow and C. H. Townes. "Infrared and Optical Masers". In: *Phys. Rev.* 112 (6 Dec. 1958), pp. 1940–1949. DOI: 10.1103/PhysRev.112.1940. URL: https://link.aps.org/doi/10.1103/PhysRev.112.1940.

[3] P. A. Franken et al. "Generation of Optical Harmonics". In: *Phys. Rev. Lett.* 7 (4 Aug. 1961), pp. 118–119. DOI: 10.1103/PhysRevLett.7.118. URL: https://link.aps.org/doi/10.1103/PhysRevLett.7.118.

[4] R.W. Boyd. *Nonlinear Optics*. Elsevier Science, 2020.

[5] R. W. Hellwarth. "Theory of the Pulsation of Fluorescent Light From Ruby". In: *Phys. Rev. Lett.* 6 (1 Jan. 1961), pp. 9–12. DOI: 10.1103/PhysRevLett.6.9. URL: https://link.aps.org/doi/10.1103/PhysRevLett.6.9.

[6] L. E. Hargrove, R. L. Fork, and M. A. Pollack. "Locking of He-Ne laser modes induced by synchronous intracavity modulation". In: *Applied Physics Letters* 5.1 (Nov. 2004), pp. 4–5. ISSN: 0003-6951. DOI: 10.1063/1.1754025. eprint: https://pubs.aip.org/aip/apl/article-pdf/5/1/4/7760678/4_1_online.pdf. URL: https://doi.org/10.1063/1.1754025.

[7] Nathalie Picqué and Theodor W. Hänsch. "Frequency comb spectroscopy". In: *Nature Photonics* 13 (3 2019). [theory]
Bases de la dual comb spectro, pp. 146–157. ISSN: 17494893. DOI: 10.1038/s41566-018-0347-5. URL: http://dx.doi.org/10.1038/s41566-018-0347-5.

[8] John L. Hall. "Why it took so long for the laser and the optical comb to be invented: the unmarked trail from concept to experimental reality". In: *J. Opt. Soc. Am. B* 34.2 (Feb. 2017), pp. 338–346. DOI: 10.1364/JOSAB.34.000338. URL: https://opg.optica.org/josab/abstract.cfm?URI=josab-34-2-338.

[9] Th Udem, R. Holzwarth, and T. W. Hänsch. "Optical frequency metrology". In: *Nature* 416 (6877 2002), pp. 233–237. ISSN: 00280836. DOI: 10.1038/416233a.

[10] H. Schnatz et al. "First Phase-Coherent Frequency Measurement of Visible Radiation". In: *Phys. Rev. Lett.* 76 (1 Jan. 1996), pp. 18–21. DOI: 10.1103/PhysRevLett.76.18. URL: https://link.aps.org/doi/10.1103/PhysRevLett.76.18.

[11] Marcus Zimmermann et al. "Optical clockwork with an offset-free difference-frequency comb: accuracy of sum- and difference-frequency generation". In: *Opt. Lett.* 29.3 (Feb. 2004), pp. 310–312. DOI: 10.1364/OL.29.000310. URL: https://opg.optica.org/ol/abstract.cfm?URI=ol-29-3-310.

[12] Th. Udem et al. “Absolute Optical Frequency Measurement of the Cesium D_1 Line with a Mode-Locked Laser”. In: *Phys. Rev. Lett.* 82 (18 May 1999), pp. 3568–3571. DOI: 10.1103/PhysRevLett.82.3568. URL: https://link.aps.org/doi/10.1103/PhysRevLett.82.3568.

[13] Tobias Wilken et al. “A spectrograph for exoplanet observations calibrated at the centimetre-per-second level”. In: *Nature* 485 (7400 2012), pp. 611–614. ISSN: 00280836. DOI: 10.1038/nature11092.

[14] B. P. Abbott and al. “Observation of Gravitational Waves from a Binary Black Hole Merger”. In: *Phys. Rev. Lett.* 116 (6 Feb. 2016), p. 061102. DOI: 10.1103/PhysRevLett.116.061102. URL: https://link.aps.org/doi/10.1103/PhysRevLett.116.061102.

[15] Markus Brehm, Albert Schliesser, and Fritz Keilmann. “Spectroscopic near-field microscopy using frequency combs in the mid-infrared”. In: *Opt. Express* 14.23 (Nov. 2006), pp. 11222–11233. DOI: 10.1364/OE.14.011222. URL: https://opg.optica.org/oe/abstract.cfm?URI=oe-14-23-11222.

[16] John L. Hall. “Nobel Lecture: Defining and measuring optical frequencies”. In: *Rev. Mod. Phys.* 78 (4 Nov. 2006), pp. 1279–1295. DOI: 10.1103/RevModPhys.78.1279. URL: https://link.aps.org/doi/10.1103/RevModPhys.78.1279.

[17] Theodor W. Hänsch. “Nobel Lecture: Passion for precision”. In: *Rev. Mod. Phys.* 78 (4 Nov. 2006), pp. 1297–1309. DOI: 10.1103/RevModPhys.78.1297. URL: https://link.aps.org/doi/10.1103/RevModPhys.78.1297.

[18] S. Schiller. “Spectrometry with frequency combs”. In: *Optics Letters* 27 (9 2002), p. 766. ISSN: 0146-9592. DOI: 10.1364/ol.27.000766.

[19] Fritz Keilmann, Christoph Gohle, and Ronald Holzwarth. “Time-domain mid-infrared frequency-comb spectrometer”. In: *Optics Letters* 29 (13 2004). première démonstration de DCS, p. 1542. ISSN: 0146-9592. DOI: 10.1364/ol.29.001542.

[20] Ian Coddington, Nathan Newbury, and William Swann. “Dual-comb spectroscopy”. In: *Optica* 3 (4 Apr. 2016), p. 414. ISSN: 2334-2536. DOI: 10.1364/optica.3.000414.

[21] Nathan R. Newbury, Ian Coddington, and William Swann. “Sensitivity of coherent dual-comb spectroscopy”. In: *Optics Express* 18.8 (2010), p. 7929. ISSN: 1094-4087. DOI: 10.1364/oe.18.007929.

[22] Bowen Li et al. “Bidirectional mode-locked all-normal dispersion fiber laser”. In: *Optica* 7.8 (Aug. 2020), pp. 961–964. DOI: 10.1364/OPTICA.396304. URL: https://opg.optica.org/optica/abstract.cfm?URI=optica-7-8-961.

[23] Takuro Ideguchi et al. “Kerr-lens mode-locked bidirectional dual-comb ring laser for broadband dual-comb spectroscopy”. In: *Optica* 3.7 (July 2016), pp. 748–753. DOI: 10.1364/OPTICA.3.000748. URL: https://opg.optica.org/optica/abstract.cfm?URI=optica-3-7-748.

[24] Avik Dutt et al. “On-chip dual-comb source for spectroscopy”. In: *Science Advances* 4.3 (2018), pp. 1–10. ISSN: 23752548. DOI: 10.1126/sciadv.1701858.

[25] Alexandre Parriaux, Kamal Hammani, and Guy Millot. “Electro-optic frequency combs”. In: *Adv. Opt. Photon.* 12.1 (Mar. 2020), pp. 223–287. DOI: 10.1364/AOP.382052. URL: https://opg.optica.org/aop/abstract.cfm?URI=aop-12-1-223.

[26] Guy Millot et al. “Frequency-agile dual-comb spectroscopy”. In: *Nature Photonics* 10 (1 Jan. 2016), pp. 27–30. ISSN: 17494893. DOI: 10.1038/nphoton.2015.250.

[27] Vicente Durán, Peter A. Andrekson, and Víctor Torres-Company. "Electro-optic dual-comb interferometry over 40 nm bandwidth". In: *Opt. Lett.* 41.18 (Sept. 2016), pp. 4190–4193. DOI: 10.1364/OL.41.004190. URL: https://opg.optica.org/ol/abstract.cfm?URI=ol-41-18-4190.

[28] Bachana Lomsadze, Brad C. Smith, and Steven T. Cundiff. "Tri-comb spectroscopy". In: *Nature Photonics* 12 (11 2018), pp. 676–680. ISSN: 17494893. DOI: 10.1038/s41566-018-0267-4. URL: http://dx.doi.org/10.1038/s41566-018-0267-4.

[29] Junwoo Kim, Tai Hyun Yoon, and Minhaeng Cho. "Time-Resolved Impulsive Stimulated Raman Spectroscopy with Synchronized Triple Mode-Locked Lasers". In: *Journal of Physical Chemistry Letters* 11.8 (Apr. 2020), pp. 2864–2869. ISSN: 19487185. DOI: 10.1021/acs.jpclett.0c00596.

[30] Steven T Cundiff and Shaul Mukamel. *Optical multidimensional coherent spectroscopy*. 2013, p. 44. URL: www.physicstoday.org.

[31] Hebin Li et al. *Optical Multidimensional Coherent Spectroscopy*. Oxford University Press, Feb. 2023. ISBN: 978-0-19-284386-9. DOI: 10.1093/oso/9780192843869.001.0001. URL: https://doi.org/10.1093/oso/9780192843869.001.0001 (visited on 05/04/2023).

[32] Kochise Bennett, Jeremy R. Rouxel, and Shaul Mukamel. "Linear and nonlinear frequency- and time-domain spectroscopy with multiple frequency combs". In: *Journal of Chemical Physics* 147.9 (2017). ISSN: 00219606. DOI: 10.1063/1.5000375.

[33] Ting Li et al. "Absolute Distance Measurement with a Long Ambiguity Range Using a Tri-Comb Mode-Locked Fiber Laser". In: *2019 Conference on Lasers and Electro-Optics, CLEO 2019 - Proceedings* (2019), pp. 23–24. DOI: 10.23919/CLEO.2019.8749862.

[34] E. Lucas et al. "Spatial multiplexing of soliton microcombs". In: *Nature Photonics* 12.11 (Nov. 2018), pp. 699–705. ISSN: 17494893. DOI: 10.1038/s41566-018-0256-7.

[35] Tara Fortier and Esther Baumann. "20 Years of Developments in Optical Frequency Comb Technology and Applications". In: *Communications Physics* 2.1 (2019), pp. 1–16. ISSN: 23993650. URL: http://dx.doi.org/10.1038/s42005-019-0249-y.

[36] Tobias J. Kippenberg et al. "Dissipative Kerr solitons in optical microresonators". EN. In: *Science* 361.6402 (Aug. 2018), eaan8083. ISSN: 0036-8075, 1095-9203. DOI: 10.1126/science.aan8083. URL: http://science.sciencemag.org/content/361/6402/eaan8083 (visited on 12/03/2018).

[37] N. Poli et al. "Optical atomic clocks". In: *Rivista del Nuovo Cimento* 36.12 (2013), pp. 555–624. ISSN: 0393697X. DOI: 10.1393/ncr/i2013-10095-x. arXiv: 1407.3493.

[38] Steven T. Cundiff and Jun Ye. "Colloquium: Femtosecond optical frequency combs". In: *Rev. Mod. Phys.* 75 (1 Mar. 2003), pp. 325–342. DOI: 10.1103/RevModPhys.75.325. URL: https://link.aps.org/doi/10.1103/RevModPhys.75.325.

[39] Wanpeng Yang et al. "Detecting Topological Defect Dark Matter Using Coherent Laser Ranging System". In: *Nature* 6.July (2016), pp. 8–13. ISSN: 20452322. DOI: 10.1038/srep29519.

[40] Myoung Gyun Suh et al. "Searching for exoplanets using a microresonator astrocomb". In: *Nature Photonics* 13.1 (2019), pp. 25–30. ISSN: 17494893. DOI: 10.1038/s41566-018-0312-3. arXiv: 1801.05174.

[41] P. Masika P. Balling, P. Kren and S.A van den Berg. "Femtosecond frequecy comb based distance measurement in air". In: *Optics Express* 17.11 (2009), pp. 9300–9313. ISSN: 21622701.

[42] P Trocha et al. “Ultrafast optical ranging using microresonator soliton frequency combs”. In: *Science* 359.6378 (2018), pp. 887–891. ISSN: 10959203. DOI: 10.1126/science.aao3924. arXiv: 1707.05969. URL: https://www.science.org.

[43] M. Imrul Kayes and Martin Rochette. “Precise Distance Measurement by a Single Electro-Optic Frequency Comb”. In: *IEEE Photonics Technology Letters* 31.10 (2019), pp. 775–778. ISSN: 19410174. DOI: 10.1109/LPT.2019.2907576.

[44] Theodor W. Hänsch. “Nobel Lecture: Passion for precision”. In: *Reviews of Modern Physics* 78.4 (Nov. 2006). Publisher: American Physical Society, pp. 1297–1309. DOI: 10.1103/RevModPhys.78.1297. URL: https://link.aps.org/doi/10.1103/RevModPhys.78.1297 (visited on 12/22/2022).

[45] Ian Coddington, William C. Swann, and Nathan R. Newbury. “Coherent Multiheterodyne Spectroscopy Using Stabilized Optical Frequency Combs”. In: *Physical Review Letters* 100.1 (Jan. 2008), p. 013902. DOI: 10.1103/PhysRevLett.100.013902. URL: https://link.aps.org/doi/10.1103/PhysRevLett.100.013902 (visited on 12/08/2018).

[46] Enrico Rubiola and Francois Vernotte. “The Companion of Enrico’s Chart for Phase Noise and Two-Sample Variances”. In: (2022), pp. 1–30. ISSN: 15579670. DOI: 10.1109/TMTT.2023.3238267. eprint: 2201.07109. URL: http://arxiv.org/abs/2201.07109.

[47] J. Rutman and F.L. Walls. “Characterization of frequency stability in precision frequency sources”. In: *Proceedings of the IEEE* 79.7 (1991), pp. 952–960. DOI: 10.1109/5.84972.

[48] D.W. Allan. “Statistics of atomic frequency standards”. In: *Proceedings of the IEEE* 54.2 (1966), pp. 221–230. DOI: 10.1109/PROC.1966.4634.

[49] J. Reichert et al. “Measuring the frequency of light with mode-locked lasers”. In: *Optics Communications* 172.1 (1999), pp. 59–68. ISSN: 0030-4018. DOI: https://doi.org/10.1016/S0030-4018(99)00491-5. URL: https://www.sciencedirect.com/science/article/pii/S0030401899004915.

[50] H R Telle et al. “Carrier-envelope offset phase control : A novel concept for absolute optical frequency measurement and ultrashort pulse generation”. In: *Apl. Phy. B* 332 (1999), pp. 327–332.

[51] David J. Jones et al. “Frequency comb generation using femtosecond pulses and cross-phase modulation in optical fiber at arbitrary center frequencies”. In: *Optics Letters* 25.5 (2000), p. 308. ISSN: 0146-9592. DOI: 10.1364/ol.25.000308.

[52] Jinendra K. Ranka, Robert S. Windeler, and Andrew J. Stentz. “Visible continuum generation in air–silica microstructure optical fibers with anomalous dispersion at 800 nm”. In: *Opt. Lett.* 25.1 (Jan. 2000), pp. 25–27. DOI: 10.1364/OL.25.000025. URL: https://opg.optica.org/ol/abstract.cfm?URI=ol-25-1-25.

[53] R. R. Alfano and S. L. Shapiro. “Emission in the Region 4000 to 7000 Å Via Four-Photon Coupling in Glass”. In: *Phys. Rev. Lett.* 24 (11 Mar. 1970), pp. 584–587. DOI: 10.1103/PhysRevLett.24.584. URL: https://link.aps.org/doi/10.1103/PhysRevLett.24.584.

[54] Chinlon Lin and R. H. Stolen. “New nanosecond continuum for excited-state spectroscopy”. In: *Applied Physics Letters* 28.4 (Aug. 1976), pp. 216–218. ISSN: 0003-6951. DOI: 10.1063/1.88702. eprint: https://pubs.aip.org/aip/apl/article-pdf/28/4/216/7736589/216_1_online.pdf. URL: https://doi.org/10.1063/1.88702.

[55] J. C. Knight et al. “All-silica single-mode optical fiber with photonic crystal cladding”. In: *Opt. Lett.* 21.19 (Oct. 1996), pp. 1547–1549. DOI: 10.1364/OL.21.001547. URL: https://opg.optica.org/ol/abstract.cfm?URI=ol-21-19-1547.

[56] P. Russell. "Photonic crystal fiber". In: *Science* 299.358 (2003). ISSN: 13483447. DOI: 10.1126/science.1079280.

[57] T. A. Birks, W. J. Wadsworth, and P. St. J. Russell. "Supercontinuum generation in tapered fibers". In: *Opt. Lett.* 25.19 (Oct. 2000), pp. 1415–1417. DOI: 10.1364/OL.25.001415. URL: https://opg.optica.org/ol/abstract.cfm?URI=ol-25-19-1415.

[58] Sho Okubo et al. "Offset-free optical frequency comb self-referencing with an f-2f interferometer". In: *Optica* 5 (2 Feb. 2018), p. 188. ISSN: 23342536. DOI: 10.1364/optica.5.000188.

[59] Vaughn Chu. *The Usage of MgO:PPLN Crystal in f-to-2f Interferometry*. 2023. URL: https://covesion.com/en/products/mgoppln-crystals-and-chips/.

[60] J. Oudin. "Utilisation de lasers femtoseconde peigne de fréquences pour des applications de détection simultanée multi-espèces de gaz à distance Thèse". PhD thesis. 2020.

[61] K. Hitomi et al. "Simple Method to Lock an Optical Frequency Comb to an Ultra-Stable Laser Without an RF Signal Generator". In: *2018 Conference on Lasers and Electro-Optics Pacific Rim, CLEO-PR 2018* 2.5 (2018). DOI: 10.1364/cleopr.2018.w2f.5.

[62] Yann Le Coq et al. "Peignes de fréquences femtosecondes pour la mesure des fréquences optiques Femtosecond frequency combs for optical frequencies metrology". In: *Revue Française de Métrologie* 2012-4.32 (2012), pp. 35–47. DOI: 10.1051/rfm/2012013.

[63] François Salin, Jeff Squier, and Michel Piché. "Mode locking of Ti:Al2O3 lasers and self-focusing: a Gaussian approximation". In: *Opt. Lett.* 16.21 (Nov. 1991), pp. 1674–1676. DOI: 10.1364/OL.16.001674. URL: https://opg.optica.org/ol/abstract.cfm?URI=ol-16-21-1674.

[64] D. E. Spence, P. N. Kean, and W. Sibbett. "60-fsec pulse generation from a self-mode-locked Ti:sapphire laser". In: *Opt. Lett.* 16.1 (Jan. 1991), pp. 42–44. DOI: 10.1364/OL.16.000042. URL: https://opg.optica.org/ol/abstract.cfm?URI=ol-16-1-42.

[65] Sergey Kobtsev, Sergey Kukarin, and Yurii Fedotov. "Ultra-low repetition rate mode-locked fiber laser with high-energy pulses". In: *Optics Express* 16.26 (2008), p. 21936. ISSN: 1094-4087. DOI: 10.1364/oe.16.021936.

[66] Xiaolong Tian et al. "High-energy laser pulse with a submegahertz repetition rate from a passively mode-locked fiber laser". In: *Optics Letters* 34.9 (2009), p. 1432. ISSN: 0146-9592. DOI: 10.1364/ol.34.001432.

[67] S.A Diddams et al. "An optical clock based on a single trapped 199Hg+ ion". In: *Science* 293.August (2001), pp. 825–828. DOI: 10.1142/9789812838223_0027.

[68] A. Stingl et al. "Sub-10-fs mirror-dispersion-controlled Ti:sapphire laser". In: *Opt. Lett.* 20.6 (Mar. 1995), pp. 602–604. DOI: 10.1364/OL.20.000602. URL: https://opg.optica.org/ol/abstract.cfm?URI=ol-20-6-602.

[69] Nathan R. Newbury and Brian R. Washburn. "Theory of the frequency comb output from a femstosecond fiber laser". In: *IEEE Journal of Quantum Electronics* 41 (11 Nov. 2005), pp. 1388–1402. ISSN: 00189197. DOI: 10.1109/JQE.2005.857657.

[70] M. E. Fermann et al. "Nonlinear amplifying loop mirror". In: *Optics Letters* 15.13 (1990), p. 752. ISSN: 0146-9592. DOI: 10.1364/ol.15.000752.

[71] Wolfgang Hänsel et al. "All polarization-maintaining fiber laser architecture for robust femtosecond pulse generation". In: *Applied Physics B: Lasers and Optics* 123.1 (2017), pp. 1–6. ISSN: 09462171. DOI: 10.1007/s00340-016-6598-2.

[72] P. Del'Haye et al. "Optical frequency comb generation from a monolithic microresonator". In: *Nature* 450 (7173 2007), pp. 1214–1217. ISSN: 14764687. DOI: 10.1038/nature06401.

[73] T. Herr et al. "Mode spectrum and temporal soliton formation in optical microresonators". In: *Physical Review Letters* 113.12 (2014), pp. 1–6. ISSN: 10797114. DOI: 10.1103/PhysRevLett.113.123901. arXiv: 1311.1716.

[74] Tobias J. Kippenberg et al. "Dissipative Kerr solitons in optical microresonators". In: *Science* 361.6402 (2018), eaan8083. DOI: 10.1126/science.aan8083. eprint: https://www.science.org/doi/pdf/10.1126/science.aan8083. URL: https://www.science.org/doi/abs/10.1126/science.aan8083.

[75] Alessia Pasquazi et al. "Micro-combs: A novel generation of optical sources". In: *Physics Reports* 729 (2018), pp. 1–81. ISSN: 03701573. DOI: 10.1016/j.physrep.2017.08.004. URL: https://doi.org/10.1016/j.physrep.2017.08.004.

[76] Yang Sun et al. "Applications of optical microcombs". In: *Adv. Opt. Photon.* 15.1 (Mar. 2023), pp. 86–175. DOI: 10.1364/AOP.470264. URL: https://opg.optica.org/aop/abstract.cfm?URI=aop-15-1-86.

[77] K. J. Vahala. "Optical microcavities". In: *2005 European Quantum Electronics Conference, EQEC '05* 2005.August (2005), p. 352. DOI: 10.1109/EQEC.2005.1567517.

[78] P. Del'Haye et al. "Full stabilization of a microresonator-based optical frequency comb". In: *Physical Review Letters* 101.5 (2008), pp. 1–4. ISSN: 00319007. DOI: 10.1103/PhysRevLett.101.053903. arXiv: 0803.1771.

[79] T. J. Kippenberg, R. Holzwarth, and S. A. Diddams. "Microresonator-based optical frequency combs". In: *Science* 332.6029 (2011), pp. 555–559. ISSN: 10959203. DOI: 10.1126/science.1193968.

[80] Myoung-Gyun Suh et al. "Microresonator soliton dual-comb spectroscopy". In: *Science* 354.6312 (2016), pp. 600–603.

[81] Florent Bessin et al. "Gain-through-filtering enables tuneable frequency comb generation in passive optical resonators". In: *Nature Communications* 10.1 (2019), pp. 1–6. ISSN: 20411723. DOI: 10.1038/s41467-019-12375-3. URL: http://dx.doi.org/10.1038/s41467-019-12375-3.

[82] Weiqiang Wang et al. "Dual-pump Kerr Micro-cavity Optical Frequency Comb with varying FSR spacing". In: *Scientific Reports* 6 (2016), pp. 4–10. ISSN: 20452322. DOI: 10.1038/srep28501.

[83] P. Del'Haye et al. "Octave spanning tunable frequency comb from a microresonator". In: *Physical Review Letters* 107.6 (2011), pp. 1–4. ISSN: 00319007. DOI: 10.1103/PhysRevLett.107.063901.

[84] Steven Miller et al. "Tunable frequency combs based on dual microring resonators". In: *Conference on Lasers and Electro-Optics Europe - Technical Digest* 2015-August.16 (2015), pp. 3398–3400. ISSN: 10944087. DOI: 10.1364/oe.23.021527. arXiv: 1505.07138.

[85] W. Steier. "A push-pull optical amplitude modulator". In: *IEEE Journal of Quantum Electronics* 3.12 (1967), pp. 664–667. DOI: 10.1109/JQE.1967.1074434.

[86] Lin Chang, Songtao Liu, and John E. Bowers. "Integrated optical frequency comb technologies". In: *Nature Photonics* 16.2 (2022), pp. 95–108. ISSN: 17494893. DOI: 10.1038/s41566-021-00945-1.

[87] T. Sylvestre et al. “Recent advances in supercontinuum generation in specialty optical fibers”. In: *J. Opt. Soc. Am. B* 38.12 (Dec. 2021), F90–F103. DOI: 10.1364/JOSAB.439330. URL: https://opg.optica.org/josab/abstract.cfm?URI=josab-38-12-F90.

[88] Govind P. Agrawal. In: *Nonlinear Fiber Optics*. Elsevier, 2013. DOI: 10.1016/B978-0-12-397023-7.00018-8.

[89] Keith J. Blow and David P. Wood. “Theoretical description of transient stimulated Raman scattering in optical fibers”. In: *IEEE Journal of Quantum Electronics* 25 (1989), pp. 2665–2673. URL: https://api.semanticscholar.org/CorpusID:122938992.

[90] Jonathan C. Knight. “Photonic crystal fibres”. In: *Nature* 424.6950 (2003), pp. 847–851. ISSN: 00280836. DOI: 10.1038/nature01940.

[91] Li Shen et al. “A review of nonlinear applications in silicon optical fibers from telecom wavelengths into the mid-infrared spectral region”. In: *Optics Communications* 463.February (2020), p. 125437. ISSN: 00304018. DOI: 10.1016/j.optcom.2020.125437. URL: https://doi.org/10.1016/j.optcom.2020.125437.

[92] R.H Stolen. *Optical fiber telecommunication - Nonlinear properties of optical fibers*. Academic Press, 1975.

[93] K. Imai, M. Kourogi, and M. Ohtsu. “30-THz span optical frequency comb generation by self-phase modulation in an optical fiber”. In: *IEEE Journal of Quantum Electronics* 34.1 (1998), pp. 54–60. DOI: 10.1109/3.655007.

[94] Th Udem, R. Holzwarth, and Th Hänsch. “Femtosecond optical frequency combs”. In: *European Physical Journal: Special Topics* 172 (1 2009), pp. 69–79. ISSN: 19516355. DOI: 10.1140/epjst/e2009-01042-6.

[95] Fujio Shimizu. “Frequency Broadening in Liquids by a Short Light Pulse”. In: *Phys. Rev. Lett.* 19 (19 Nov. 1967), pp. 1097–1100. DOI: 10.1103/PhysRevLett.19.1097. URL: https://link.aps.org/doi/10.1103/PhysRevLett.19.1097.

[96] R. H. Stolen and Chinlon Lin. “Self-phase-modulation in silica optical fibers”. In: *Phys. Rev. A* 17 (4 Apr. 1978), pp. 1448–1453. DOI: 10.1103/PhysRevA.17.1448. URL: https://link.aps.org/doi/10.1103/PhysRevA.17.1448.

[97] R. H. Stolen, J. E. Bjorkholm, and A. Ashkin. “Phase-matched three-wave mixing in silica fiber optical waveguides”. In: *Applied Physics Letters* 24 (7 1974), pp. 308–310. ISSN: 00036951. DOI: 10.1063/1.1655195.

[98] Aku Antikainen and Govind P. Agrawal. “Dual-pump frequency comb generation in normally dispersive optical fibers”. In: *Journal of the Optical Society of America B* 32.8 (2015), p. 1705. ISSN: 0740-3224. DOI: 10.1364/josab.32.001705.

[99] Ting Wang et al. “Octave-spanning frequency comb generation based on a dual-mode microcavity laser”. In: *Photonics Research* 10.9 (2022), p. 2107. ISSN: 23279125. DOI: 10.1364/prj.462644.

[100] Flavio C. Cruz. “Optical frequency combs generated by four-wave mixing in optical fibers for astrophysical spectrometer calibration and metrology”. In: *AIP Conference Proceedings* 1055.17 (2008), pp. 83–86. ISSN: 0094243X. DOI: 10.1063/1.3002551.

[101] J. Fatome et al. “Multiple four-wave mixing in optical fibers: 1.5-3.4-THz femtosecond pulse sources and real-time monitoring of a 20-GHz picosecond source”. In: *Optics Communications* 283.11 (2010), pp. 2425–2429. ISSN: 00304018. DOI: 10.1016/j.optcom.2010.01.057. URL: http://dx.doi.org/10.1016/j.optcom.2010.01.057.

[102] Y. H. Li, Y. Y. Zhao, and L. J. Wang. "Demonstration of almost octave-spanning cascaded four-wave mixing in optical microfibers". In: *Opt. Lett.* 37.16 (Aug. 2012), pp. 3441–3443. DOI: 10.1364/OL.37.003441. URL: https://opg.optica.org/ol/abstract.cfm?URI=ol-37-16-3441.

[103] Zhi Tong et al. "Spectral linewidth preservation in parametric frequency combs seeded by dual pumps". In: *Optics Express* 20.16 (2012), p. 17610. ISSN: 1094-4087. DOI: 10.1364/oe.20.017610.

[104] Hiroshi Fukuda et al. "Four-wave mixing in silicon wire waveguides". In: *Optics Express* 13.12 (2005), p. 4629. ISSN: 1094-4087. DOI: 10.1364/opex.13.004629.

[105] Yang Liu et al. "Bandwidth scaling of phase-modulated CW comb through four-wave mixing on silicon nano-waveguide". In: *2013 Conference on Lasers and Electro-Optics, CLEO 2013* 39.22 (2013), pp. 6478–6481. DOI: 10.1364/cleo_si.2013.cf1g.3.

[106] T. Hansson and S. Wabnitz. "Bichromatically pumped microresonator frequency combs". In: *Physical Review A - Atomic, Molecular, and Optical Physics* 90.1 (2014), pp. 1–7. ISSN: 10941622. DOI: 10.1103/PhysRevA.90.013811.

[107] D. Ceoldo et al. "Kerr frequency combs in a bichromatically pumped nonlinear fiber ring cavity". In: *European Conference on Optical Communication, ECOC* 41.23 (2016), pp. 538–540.

[108] J. D. Kafka, J. W. Pieterse, and M. L. Watts. "Two-color subpicosecond optical sampling technique". In: *Opt. Lett.* 17.18 (Sept. 1992), pp. 1286–1288. DOI: 10.1364/OL.17.001286. URL: https://opg.optica.org/ol/abstract.cfm?URI=ol-17-18-1286.

[109] Albert Schliesser et al. "Frequency-comb infrared spectrometer for rapid, remote chemical sensing". In: *Opt. Express* 13.22 (Oct. 2005), pp. 9029–9038. DOI: 10.1364/OPEX.13.009029. URL: https://opg.optica.org/oe/abstract.cfm?URI=oe-13-22-9029.

[110] Takuro Ideguchi. "Dual-Comb Spectroscopy". In: *Opt. Photon. News* 28.1 (Jan. 2017), pp. 32–39. DOI: 10.1364/OPN.28.1.000032. URL: https://www.optica-opn.org/abstract.cfm?URI=opn-28-1-32.

[111] David Middleton, Institute of Electrical, and Electronics Engineers. *An introduction to statistical communication theory*. Vol. 960. McGraw-Hill New York, 1960.

[112] D. S. Elliott, Rajarshi Roy, and S. J. Smith. "Extracavity laser band-shape and bandwidth modification". In: *Phys. Rev. A* 26 (1 July 1982), pp. 12–18. DOI: 10.1103/PhysRevA.26.12. URL: https://link.aps.org/doi/10.1103/PhysRevA.26.12.

[113] Vicente Durán, Santiago Tainta, and Victor Torres-Company. "Ultrafast electrooptic dual-comb interferometry". In: *Optics Express* 23 (23 2015), p. 30557. ISSN: 1094-4087. DOI: 10.1364/oe.23.030557.

[114] Elena L Teleanu, Vicente Durán, and Víctor Torres-Company. "Chalmers Publication Library Electro-optic dual-comb interferometer for high-speed vibrometry Electro-00adoptic dual-00adcomb interferometer for high-speed vibrometry". In: *Optics Express* 25 (14 2017), pp. 16427–16436. URL: http://publications.lib.chalmers.se/publication/250388.

[115] Zebin Zhu and Guanhao Wu. "Dual-Comb Ranging". In: *Engineering* 4 (6 Dec. 2018), pp. 772–778. ISSN: 20958099. DOI: 10.1016/j.eng.2018.10.002.

[116] Xuling Shen et al. "Adaptive Dual-Comb Spectroscopy with 1200-h Continuous Operation Stability". In: *IEEE Photonics Journal* 10.5 (2018), pp. 1–9. ISSN: 19430655. DOI: 10.1109/JPHOT.2018.2864986.

[117] Takuro Ideguchi et al. "Adaptive real-time dual-comb spectroscopy". In: *Nature Communications* 5 (1 2014), p. 3375. ISSN: 2041-1723. DOI: 10.1038/ncomms4375. URL: https://doi.org/10.1038/ncomms4375.

[118] Gustavo Villares et al. "Dual-comb spectroscopy based on quantum-cascade-laser frequency combs". In: *Nature Communications* 5 (2014), pp. 1–3. ISSN: 20411723. DOI: 10.1038/ncomms6192.

[119] Mengjie Yu et al. "Silicon-chip-based mid-infrared dual-comb spectroscopy". In: *Nature Communications* 9.1 (2018), pp. 6–11. ISSN: 20411723. DOI: 10.1038/s41467-018-04350-1. arXiv: 1610.01121.

[120] Xin Zhao et al. "Picometer-resolution dual-comb spectroscopy with a free-running fiber laser". In: *Optics Express* 24.19 (2016), p. 21833. ISSN: 10944087. DOI: 10.1364/oe.24.021833. arXiv: 1602.07788.

[121] S. Mehravar et al. "Real-time dual-comb spectroscopy with a free-running bidirectionally mode-locked fiber laser". In: *Applied Physics Letters* 108.23 (2016). ISSN: 00036951. DOI: 10.1063/1.4953400. URL: http://dx.doi.org/10.1063/1.4953400.

[122] Ruoyu Liao et al. "Dual-comb spectroscopy with a single free-running thulium-doped fiber laser". In: *Optics Express* 26.8 (2018), p. 11046. ISSN: 10944087. DOI: 10.1364/oe.26.011046.

[123] M. Imrul Kayes et al. "Free-running mode-locked laser based dual-comb spectroscopy". In: *Optics Letters* 43.23 (Dec. 2018), pp. 5809–5812. ISSN: 1539-4794. DOI: 10.1364/OL.43.005809. URL: https://www.osapublishing.org/ol/abstract.cfm?uri=ol-43-23-5809 (visited on 12/03/2018).

[124] Justinas Pupeikis et al. "Picosecond ultrasonics with a free-running dual-comb laser". In: *Optics Express* 29.22 (2021), p. 35735. ISSN: 10944087. DOI: 10.1364/oe.440856.

[125] C. R. Phillips et al. "Coherently averaged dual-comb spectroscopy with a low-noise and high-power free-running gigahertz dual-comb laser". In: *Optics Express* 31.5 (2023), p. 7103. ISSN: 10944087. DOI: 10.1364/oe.479356. arXiv: 2211.01368.

[126] Julien Roy et al. "Continuous real-time correction and averaging for frequency comb interferometry". In: *Opt. Express* 20.20 (Sept. 2012), pp. 21932–21939. DOI: 10.1364/OE.20.021932. URL: https://opg.optica.org/oe/abstract.cfm?URI=oe-20-20-21932.

[127] Lukasz A. Sterczewski, Jonas Westberg, and Gerard Wysocki. "Computational coherent averaging for free-running dual-comb spectroscopy". In: *Optics Express* 27.17 (2019), p. 23875. ISSN: 10944087. DOI: 10.1364/oe.27.023875. arXiv: 1805.11146.

[128] Annelise R. Beck, Daniel M. Neumark, and Stephen R. Leone. "Probing ultrafast dynamics with attosecond transient absorption". In: *Chemical Physics Letters* 624 (2015), pp. 119–130. ISSN: 0009-2614. DOI: https://doi.org/10.1016/j.cplett.2014.12.048. URL: https://www.sciencedirect.com/science/article/pii/S0009261414010781.

[129] Marcos Dantus. "Coherent nonlinear spectroscopy: From Femtosecond Dynamics to Control". In: *Annual Review of Physical Chemistry* 52.1 (2001). PMID: 11326077, pp. 639–679. DOI: 10.1146/annurev.physchem.52.1.639. eprint: https://doi.org/10.1146/annurev.physchem.52.1.639. URL: https://doi.org/10.1146/annurev.physchem.52.1.639.

[130] Villy Sundström. "Femtobiology". In: *Annual Review of Physical Chemistry* 59.1 (2008). PMID: 17892434, pp. 53–77. DOI: 10.1146/annurev.physchem.59.032607.093615. eprint: https://doi.org/10.1146/annurev.physchem.59.032607.093615. URL: https://doi.org/10.1146/annurev.physchem.59.032607.093615.

[131] Michael R. Wasielewski. "Energy, Charge, and Spin Transport in Molecules and Self-Assembled Nanostructures Inspired by Photosynthesis". In: *The Journal of Organic Chemistry* 71.14 (2006). PMID: 16808492, pp. 5051–5066. DOI: 10.1021/jo060225d. eprint: https://doi.org/10.1021/jo060225d. URL: https://doi.org/10.1021/jo060225d.

[132] Luca Bolzonello, Francesca Fassioli, and Elisabetta Collini. "Correlated Fluctuations and Intraband Dynamics of J-Aggregates Revealed by Combination of 2DES Schemes". In: *The Journal of Physical Chemistry Letters* 7.24 (2016). PMID: 27973862, pp. 4996–5001. DOI: 10.1021/acs.jpclett.6b02433. eprint: https://doi.org/10.1021/acs.jpclett.6b02433. URL: https://doi.org/10.1021/acs.jpclett.6b02433.

[133] Luca Bolzonello et al. "Two-Dimensional Electronic Spectroscopy Reveals Dynamics and Mechanisms of Solvent-Driven Inertial Relaxation in Polar BODIPY Dyes". In: *The Journal of Physical Chemistry Letters* 9.5 (2018). PMID: 29446639, pp. 1079–1085. DOI: 10.1021/acs.jpclett.7b03393. eprint: https://doi.org/10.1021/acs.jpclett.7b03393. URL: https://doi.org/10.1021/acs.jpclett.7b03393.

[134] Elisabetta Collini. *Ultrafast Laser Technologies and Applications Femto-UP 2020 - Coherent Multidimensional spectroscopie: Advanced spectroscopic techniques to unveil complex dynamics*. edp sciences, 2022. ISBN: 978-2-7598-2720-6. DOI: 10.1051/978-2-7598-2719-0.

[135] S. Mukamel. *Principles of Nonlinear Optical Spectroscopy*. Oxford series in optical and imaging sciences. Oxford University Press, 1995. ISBN: 9780195092783. URL: https://books.google.fr/books?id=k_7uAAAAMAAJ.

[136] Jaeyoung Sung and Robert J. Silbey. "Four wave mixing spectroscopy for a multilevel system". In: *The Journal of Chemical Physics* 115.20 (Nov. 2001), pp. 9266–9287. ISSN: 0021-9606. DOI: 10.1063/1.1413979. eprint: https://pubs.aip.org/aip/jcp/article-pdf/115/20/9266/10836401/9266_1_online.pdf. URL: https://doi.org/10.1063/1.1413979.

[137] N. A. Kurnit, I. D. Abella, and S. R. Hartmann. "Observation of a Photon Echo". In: *Phys. Rev. Lett.* 13 (19 Nov. 1964), pp. 567–568. DOI: 10.1103/PhysRevLett.13.567. URL: https://link.aps.org/doi/10.1103/PhysRevLett.13.567.

[138] Galina Khitrova, Paul R. Berman, and Murray Sargent. "Theory of pump–probe spectroscopy". In: *J. Opt. Soc. Am. B* 5.1 (Jan. 1988), pp. 160–170. DOI: 10.1364/JOSAB.5.000160. URL: https://opg.optica.org/josab/abstract.cfm?URI=josab-5-1-160.

[139] Richard R. Ernst. *Principles of nuclear magnetic resonance in one and two dimensions*. The international series of monographs on chemistry. Oxford: Clarendon Press, 1991. ISBN: 0-19-855629-2.

[140] Andrius Gelzinis et al. "Two-dimensional spectroscopy for non-specialists". In: *Biochimica et Biophysica Acta (BBA) - Bioenergetics* 1860.4 (2019), pp. 271–285. ISSN: 0005-2728. DOI: https://doi.org/10.1016/j.bbabio.2018.12.006. URL: https://www.sciencedirect.com/science/article/pii/S0005272818302457.

[141] Shaul Mukamel and Roger F. Loring. "Nonlinear response function for time-domain and frequency-domain four-wave mixing". In: *Journal of the Optical Society of America B* 3.4 (1986), p. 595. ISSN: 0740-3224. DOI: 10.1364/josab.3.000595.

[142] L. Lepetit, G. Chériaux, and M. Joffre. "Linear techniques of phase measurement by femtosecond spectral interferometry for applications in spectroscopy". In: *J. Opt. Soc. Am. B* 12.12 (Dec. 1995), pp. 2467–2474. DOI: 10.1364/JOSAB.12.002467. URL: https://opg.optica.org/josab/abstract.cfm?URI=josab-12-12-2467.

[143] Elad Harel, Andrew F. Fidler, and Gregory S. Engel. "Real-time mapping of electronic structure with single-shot two-dimensional electronic spectroscopy". In: *Proceedings of the National Academy of Sciences* 107.38 (2010), pp. 16444–16447. DOI: 10.1073/pnas.1007579107. eprint: https://www.pnas.org/doi/pdf/10.1073/pnas.1007579107. URL: https://www.pnas.org/doi/abs/10.1073/pnas.1007579107.

[144] Franklin D. Fuller, Daniel E. Wilcox, and Jennifer P. Ogilvie. "Pulse shaping based two-dimensional electronic spectroscopy in a background free geometry". In: *Opt. Express* 22.1 (Jan. 2014), pp. 1018–1027. DOI: 10.1364/OE.22.001018. URL: https://opg.optica.org/oe/abstract.cfm?URI=oe-22-1-1018.

[145] Simon Draeger, Sebastian Roeding, and Tobias Brixner. "Rapid-scan coherent 2D fluorescence spectroscopy". In: *Opt. Express* 25.4 (Feb. 2017), pp. 3259–3267. DOI: 10.1364/OE.25.003259. URL: https://opg.optica.org/oe/abstract.cfm?URI=oe-25-4-3259.

[146] Bachana Lomsadze and Steven T. Cundiff. "Frequency combs enable rapid and high-resolution multidimensional coherent spectroscopy". In: *Science* 357.6358 (2017), pp. 1389–1391. DOI: 10.1126/science.aao1090. eprint: https://www.science.org/doi/pdf/10.1126/science.aao1090. URL: https://www.science.org/doi/abs/10.1126/science.aao1090.

[147] Akifumi Asahara and Kaoru Minoshima. "Development of ultrafast time-resolved dual-comb spectroscopy". In: *APL Photonics* 2.4 (Feb. 2017), p. 041301. ISSN: 2378-0967. DOI: 10.1063/1.4976730. eprint: https://pubs.aip.org/aip/app/article-pdf/doi/10.1063/1.4976730/14111146/041301_1_online.pdf. URL: https://doi.org/10.1063/1.4976730.

[148] Xin Zhao et al. "Dead-Band-Free, High-Resolution Microwave Frequency Measurement Using a Free-Running Triple-Comb Fiber Laser". In: *IEEE Journal of Selected Topics in Quantum Electronics* 24 (3 May 2018). ISSN: 21910359. DOI: 10.1109/JSTQE.2017.2770098.

[149] Hebert Philippe; Lemaitre Francois; Cezard Nicolas. *Lidar with heterodyne detection by local oscillator and double probe beam, with one or more simultaneous frequencies, and lidar detection method by double heterodyne detection*. FR3082623 (A1) 2015 2019-12-20. 2019.

[150] Jianjun Yang et al. "Dual asynchronous undersampling of fast spectral variations with triple optical frequency combs". In: *Conference on Lasers and Electro-Optics*. Optica Publishing Group, 2022, JW3B.95. DOI: 10.1364/CLEO_AT.2022.JW3B.95. URL: https://opg.optica.org/abstract.cfm?URI=CLEO_AT-2022-JW3B.95.

[151] Bachana Lomsadze and Steven T. Cundiff. "Four-wave-mixing comb spectroscopy". In: vol. 2017-January. Institute of Electrical and Electronics Engineers Inc., Oct. 2017, pp. 1–2. ISBN: 9781943580279. DOI: 10.1364/OL.42.002346.

[152] Xin Zhang et al. "Sub-100 fs all-fiber broadband electro-optic optical frequency comb at 1.5 00b5m". In: *Optics Express* 28 (23 Nov. 2020), p. 34761. ISSN: 10944087. DOI: 10.1364/oe.409838.

[153] Ruitao Yang et al. "A multidimensional multiplexing mode-locked laser based on a dual-ring integrative structure for tri-comb generation". In: *Applied Sciences (Switzerland)* 10 (22 Nov. 2020), pp. 1–10. ISSN: 20763417. DOI: 10.3390/app10228260.

[154] Alexander M. Heidt et al. "Limits of coherent supercontinuum generation in normal dispersion fibers". In: *J. Opt. Soc. Am. B* 34.4 (2017), pp. 764–775. DOI: 10.1364/JOSAB.34.000764. URL: https://opg.optica.org/josab/abstract.cfm?URI=josab-34-4-764.

[155] R. H. Stolen and Chinlon Lin. "Self-phase-modulation in silica optical fibers". In: *Phys. Rev. A* 17 (4 Apr. 1978), pp. 1448–1453. DOI: 10.1103/PhysRevA.17.1448. URL: https://link.aps.org/doi/10.1103/PhysRevA.17.1448.

[156] D. J. Richardson, J. M. Fini, and L. E. Nelson. "Space-division multiplexing in optical fibres". In: *Nature Photonics* 7 (5 May 2013), pp. 354–362. ISSN: 17494885. DOI: 10.1038/nphoton.2013.94.

[157] Wei Xia and Xuzong Chen. "Recent developments in fiber-based optical frequency comb and its applications". In: *Measurement Science and Technology* 27.4 (Feb. 2016), p. 041001. DOI: 10.1088/0957-0233/27/4/041001. URL: https://dx.doi.org/10.1088/0957-0233/27/4/041001.

[158] Tamas Nagy, Peter Simon, and Laszlo Veisz. "High-energy few-cycle pulses: post-compression techniques". In: *Advances in Physics: X* 6.1 (2021), p. 1845795. DOI: 10.1080/23746149.2020.1845795.

[159] Esmerando Escoto et al. "Temporal quality of post-compressed pulses at large compression factors". In: *J. Opt. Soc. Am. B* 39.7 (July 2022), pp. 1694–1702. DOI: 10.1364/JOSAB.453901. URL: https://opg.optica.org/josab/abstract.cfm?URI=josab-39-7-1694.

[160] Tamas Nagy, Vladimir Pervak, and Peter Simon. "Optimal pulse compression in long hollow fibers". In: *Opt. Lett.* 36.22 (Nov. 2011), pp. 4422–4424. DOI: 10.1364/OL.36.004422. URL: https://opg.optica.org/ol/abstract.cfm?URI=ol-36-22-4422.

[161] Ji In Kim et al. "Sub-10 fs pulse generation by post-compression for peak-power enhancement of a 100-TW Ti:Sapphire laser". In: *Opt. Express* 30.6 (Mar. 2022), pp. 8734–8741. DOI: 10.1364/OE.452224. URL: https://opg.optica.org/oe/abstract.cfm?URI=oe-30-6-8734.

[162] R. L. Fork et al. "Compression of optical pulses to six femtoseconds by using cubic phase compensation". In: *Opt. Lett.* 12.7 (July 1987), pp. 483–485. DOI: 10.1364/OL.12.000483. URL: https://opg.optica.org/ol/abstract.cfm?URI=ol-12-7-483.

[163] Naoya Kuse, Thomas R. Schibli, and Martin E. Fermann. "Low noise electro-optic comb generation by fully stabilizing to a mode-locked fiber comb". In: *Opt. Express* 24.15 (July 2016), pp. 16884–16893. DOI: 10.1364/OE.24.016884. URL: https://opg.optica.org/oe/abstract.cfm?URI=oe-24-15-16884.

[164] Zhi Jiang et al. "Optical arbitrary waveform processing of more than 100 spectral comb lines". In: *Nature Photonics* 1 (8 Aug. 2007), pp. 463–467. ISSN: 17494885. DOI: 10.1038/nphoton.2007.139.

[165] Yijia Cai et al. "Low-noise, Flat-spectrum, Polarization-Maintaining All-Fiber Frequency Comb for Wideband Communications". In: *Optical Fiber Communication Conference (OFC) 2023*. Optica Publishing Group, 2023, Th1B.5. DOI: 10.1364/OFC.2023.Th1B.5. URL: https://opg.optica.org/abstract.cfm?URI=OFC-2023-Th1B.5.

[166] Peter Horak and Wei H. Loh. "On the delayed self-heterodyne interferometric technique for determining the linewidth of fiber lasers". In: *Opt. Express* 14.9 (May 2006), pp. 3923–3928. DOI: 10.1364/OE.14.003923. URL: https://opg.optica.org/oe/abstract.cfm?URI=oe-14-9-3923.

[167] Zhongan Zhao et al. "Narrow laser-linewidth measurement using short delay self-heterodyne interferometry". In: *Opt. Express* 30.17 (Aug. 2022), pp. 30600–30610. DOI: 10.1364/OE.455028. URL: https://opg.optica.org/oe/abstract.cfm?URI=oe-30-17-30600.

[168] Philippe Guay, Jérôme Genest, and Adam J. Fleisher. "Precision spectroscopy of H13CN using a free-running, all-fiber dual electro-optic frequency comb system". In: *Opt. Lett.* 43.6 (Mar. 2018), pp. 1407–1410. DOI: 10.1364/OL.43.001407. URL: https://opg.optica.org/ol/abstract.cfm?URI=ol-43-6-1407.

[169] Haochen Tian, Youjian Song, and Minglie Hu. "Noise Measurement and Reduction in Mode-Locked Lasers: Fundamentals for Low-Noise Optical Frequency Combs". In: *Applied Sciences* 11.16 (2021). ISSN: 2076-3417. DOI: 10.3390/app11167650. URL: https://www.mdpi.com/2076-3417/11/16/7650.

[170] Victor Tsvirkun et al. "Flexible lensless endoscope with a conformationally invariant multi-core fiber". EN. In: *Optica* 6.9 (Sept. 2019). Publisher: Optica Publishing Group, pp. 1185–1189. ISSN: 2334-2536. DOI: 10.1364/OPTICA.6.001185. URL: https://opg.optica.org/optica/abstract.cfm?uri=optica-6-9-1185 (visited on 12/21/2022).

[171] T. Osuch et al. "Thermal and aging tests of fiber Bragg gratings as wavelength standards". In: *Optical Fibers: Technology*. Ed. by Jan Rayss, Brian Culshaw, and Anna Grazia Mignani. Vol. 5951. International Society for Optics and Photonics. SPIE, 2005, 59510H. DOI: 10.1117/12.622811. URL: https://doi.org/10.1117/12.622811.

[172] Jonggu Jeon et al. "Dual frequency comb photon echo spectroscopy". In: *Journal of the Optical Society of America B* 36.2 (2019), p. 223. ISSN: 0740-3224. DOI: 10.1364/josab.36.000223.

[173] K. O. Hill et al. "cw three-wave mixing in single-mode optical fibers". In: *Journal of Applied Physics* 49.10 (Aug. 1978), pp. 5098–5106. ISSN: 0021-8979. DOI: 10.1063/1.324456. URL: https://doi.org/10.1063/1.324456 (visited on 07/06/2023).

[174] John R. Thompson and Rajarshi Roy. "Multiple four-wave mixing process in an optical fiber". In: *Optics Letters* 16.8 (1991), p. 557. ISSN: 0146-9592. DOI: 10.1364/ol.16.000557.

[175] David Carlson et al. "An Ultrafast Electro-Optic Dual Comb for Linear and Nonlinear Spectroscopy". EN. In: *Light, Energy and the Environment 2018 (E2, FTS, HISE, SOLAR, SSL) (2018), paper FT4B.2*. Optical Society of America, Nov. 2018, FT4B.2. DOI: 10.1364/FTS.2018.FT4B.2. URL: https://www.osapublishing.org/abstract.cfm?uri=FTS-2018-FT4B.2 (visited on 04/26/2019).

[176] T. Yamamoto and M. Nakazawa. "Active optical pulse compression with a gain of 29.0 dB by using four-wave mixing in an optical fiber". In: *IEEE Photonics Technology Letters* 9.12 (Dec. 1997). Conference Name: IEEE Photonics Technology Letters, pp. 1595–1597. ISSN: 1941-0174. DOI: 10.1109/68.643279.

[177] G. Kalogerakis, M.E. Marhic, and L.G. Kazovsky. "Multiple-wavelength conversion with gain by a high-repetition-rate pulsed-pump fiber OPA". In: *Journal of Lightwave Technology* 23.10 (Oct. 2005). Conference Name: Journal of Lightwave Technology, pp. 2954–2960. ISSN: 1558-2213. DOI: 10.1109/JLT.2005.855698.

[178] Reza Salem, Mark A. Foster, and Alexander L. Gaeta. "Application of space–time duality to ultrahigh-speed optical signal processing". EN. In: *Advances in Optics and Photonics* 5.3 (Sept. 2013). Publisher: Optica Publishing Group, pp. 274–317. ISSN: 1943-8206. DOI: 10.1364/AOP.5.000274. URL: https://opg.optica.org/aop/abstract.cfm?uri=aop-5-3-274 (visited on 06/27/2023).

[179] F. S. Yang et al. "Demonstration of two-pump fibre optical parametric amplification". en. In: *Electronics Letters* 33.21 (Oct. 1997). Publisher: IET Digital Library, pp. 1812–1813. ISSN: 1350-911X. URL: https://digital-library.theiet.org/content/journals/10.1049/el_19971206 (visited on 07/07/2023).

[180] M. Lillieholm et al. “Detailed characterization of CW- and pulsed-pump four-wave mixing in highly nonlinear fibers”. EN. In: *Optics Letters* 41.21 (Nov. 2016). Publisher: Optica Publishing Group, pp. 4887–4890. ISSN: 1539-4794. DOI: 10.1364/OL.41.004887. URL: https://opg.optica.org/ol/abstract.cfm?uri=ol-41-21-4887 (visited on 07/07/2023).

[181] Arnaud Mussot et al. “Amplification of ultra-short optical pulses in a two-pump fiber optical parametric chirped pulse amplifier”. In: *Optics Express* 21.10 (May 2013), pp. 12197–12203. DOI: 10.1364/OE.21.012197. URL: http://www.opticsexpress.org/abstract.cfm?URI=oe-21-10-12197 (visited on 09/04/2013).

[182] Michel E. Marhic. *Fiber Optical Parametric Amplifiers, Oscillators and Related Devices*. 1st ed. Cambridge University Press, Dec. 2007. ISBN: 0-521-86102-0.

[183] Andrea Armaroli and Stefano Trillo. “Modulational instability due to cross-phase modulation versus multiple four-wave mixing: the normal dispersion regime”. In: *J. Opt. Soc. Am. B* 31.3 (Mar. 2014), pp. 551–558. DOI: 10.1364/JOSAB.31.000551. URL: https://opg.optica.org/josab/abstract.cfm?URI=josab-31-3-551.

[184] Maxime Baillot, Thierry Chartier, and Michel Joindot. “Multiple four-wave mixing in optical fibres”. In: *European Conference on Optical Communication, ECOC* 1 (2014), pp. 1–3. DOI: 10.1109/ECOC.2014.6963922.

[185] A. D. Bristow et al. “A versatile ultrastable platform for optical multidimensional Fourier-transform spectroscopy”. In: *Review of Scientific Instruments* 80.7 (July 2009), p. 073108. ISSN: 0034-6748. DOI: 10.1063/1.3184103. eprint: https://pubs.aip.org/aip/rsi/article-pdf/doi/10.1063/1.3184103/9927374/073108_1_online.pdf. URL: https://doi.org/10.1063/1.3184103.

[186] Gaël Nardin et al. “Multidimensional coherent photocurrent spectroscopy of a semiconductor nanostructure”. In: *Opt. Express* 21.23 (Nov. 2013), pp. 28617–28627. DOI: 10.1364/OE.21.028617. URL: https://opg.optica.org/oe/abstract.cfm?URI=oe-21-23-28617.

[187] Patrick F. Tekavec, Geoffrey A. Lott, and Andrew H. Marcus. “Fluorescence-detected two-dimensional electronic coherence spectroscopy by acousto-optic phase modulation”. In: *The Journal of Chemical Physics* 127.21 (Dec. 2007), p. 214307. ISSN: 0021-9606. DOI: 10.1063/1.2800560. eprint: https://pubs.aip.org/aip/jcp/article-pdf/doi/10.1063/1.2800560/15407120/214307_1_online.pdf. URL: https://doi.org/10.1063/1.2800560.

[188] Martin Thämer et al. “Ultrafast 2D IR spectroscopy of the excess proton in liquid water”. In: *Science* 350.6256 (2015), pp. 78–82. DOI: 10.1126/science.aab3908. eprint: https://www.science.org/doi/pdf/10.1126/science.aab3908. URL: https://www.science.org/doi/abs/10.1126/science.aab3908.

[189] Daniel B. Turner et al. “Invited Article: The coherent optical laser beam recombination technique (COLBERT) spectrometer: Coherent multidimensional spectroscopy made easier”. In: *Review of Scientific Instruments* 82.8 (Aug. 2011), p. 081301. ISSN: 0034-6748. DOI: 10.1063/1.3624752. eprint: https://pubs.aip.org/aip/rsi/article-pdf/doi/10.1063/1.3624752/15896159/081301_1_online.pdf. URL: https://doi.org/10.1063/1.3624752.

[190] Yin Song et al. “Multispectral multidimensional spectrometer spanning the ultraviolet to the mid-infrared”. In: *Review of Scientific Instruments* 90.1 (Jan. 2019), p. 013108. ISSN: 0034-6748. DOI: 10.1063/1.5055244. eprint: https://pubs.aip.org/aip/rsi/article-pdf/doi/10.1063/1.5055244/14754880/013108_1_online.pdf. URL: https://doi.org/10.1063/1.5055244.

[191] D. Sapkota and J. E. Sharping. “Four-wave mixing in a triple-core microstructure fiber”. In: *Opt. Express* 29.9 (Apr. 2021), pp. 13715–13721. DOI: 10.1364/OE.421966. URL: https://opg.optica.org/oe/abstract.cfm?URI=oe-29-9-13715.

[192] Bachana Lomsadze. “Frequency comb-based multidimensional coherent spectroscopy bridges the gap between fundamental science and cutting-edge technology”. In: *The Journal of Chemical Physics* 154.16 (Apr. 2021). Publisher: American Institute of Physics, p. 160901. ISSN: 0021-9606. DOI: 10.1063/5.0047164. URL: http://aip.scitation.org/doi/full/10.1063/5.0047164 (visited on 12/20/2022).

[193] Akira Kawai et al. “Compressive dual-comb spectroscopy”. In: *Scientific Reports* 11.1 (Dec. 2021). ISSN: 20452322. DOI: 10.1038/s41598-021-93005-1. arXiv: 2007.03761.

[194] Yu Zhang et al. “Burst-mode dual-comb spectroscopy”. EN. In: *Optics Letters* 46.4 (Feb. 2021). Publisher: Optical Society of America, pp. 860–863. ISSN: 1539-4794. DOI: 10.1364/OL.416668. URL: https://www.osapublishing.org/ol/abstract.cfm?uri=ol-46-4-860 (visited on 03/22/2021).

[195] Emily D. Caldwell et al. “The time-programmable frequency comb and its use in quantum-limited ranging”. In: *Nature* 610.7933 (2022), pp. 667–673. ISSN: 14764687. DOI: 10.1038/s41586-022-05225-8.

[196] Evgeny M. Dianov. “Bismuth-doped optical fibers: A challenging active medium for near-IR lasers and optical amplifiers”. In: *Light: Science and Applications* 1.MAY (2012), pp. 1–7. ISSN: 20477538. DOI: 10.1038/lsa.2012.12.

[197] Alexandre Parriaux, Kamal Hammani, and Guy Millot. “Two-micron all-fibered dual-comb spectrometer based on electro-optic modulators and wavelength conversion”. EN. In: *Communications Physics* 1.1 (May 2018), p. 17. ISSN: 2399-3650. DOI: 10.1038/s42005-018-0017-4. URL: https://www-nature-com.ressources-electroniques.univ-lille.fr/articles/s42005-018-0017-4 (visited on 03/20/2019).

[198] Alexandre Parriaux et al. “Isotope ratio dual-comb spectrometer”. In: *Physical Review Research* 4.2 (May 2022). Publisher: American Physical Society, p. 023098. DOI: 10.1103/PhysRevResearch.4.023098. URL: https://link.aps.org/doi/10.1103/PhysRevResearch.4.023098 (visited on 12/22/2022).

[199] David R. Carlson et al. “Broadband, electro-optic, dual-comb spectrometer for linear and nonlinear measurements”. EN. In: *Optics Express* 28.20 (Sept. 2020). Publisher: Optical Society of America, pp. 29148–29154. ISSN: 1094-4087. DOI: 10.1364/OE.400433. URL: https://www.osapublishing.org/oe/abstract.cfm?uri=oe-28-20-29148 (visited on 11/29/2020).

[200] W. J. Tomlinson, R. H. Stolen, and A. M. Johnson. “Optical wave breaking of pulses in nonlinear optical fibers”. In: *Opt. Lett.* 10.9 (Sept. 1985), pp. 457–459. DOI: 10.1364/OL.10.000457. URL: https://opg.optica.org/ol/abstract.cfm?URI=ol-10-9-457.

[201] D. Anderson et al. “Wave breaking in nonlinear-optical fibers”. In: *J. Opt. Soc. Am. B* 9.8 (Aug. 1992), pp. 1358–1361. DOI: 10.1364/JOSAB.9.001358. URL: https://opg.optica.org/josab/abstract.cfm?URI=josab-9-8-1358.

[202] Janne Hyyti, Nils Raabe, and Guenter Steinmeyer. “Characterization of ultrashort laser pulses and carrier-envelope phase stabilization”. In: 2016. DOI: 10.3254/978-1-61499-647-7-207.

[203] Christophe Finot. “Similaritons dans les amplificateurs Raman à fibre optique”. Theses. Université de Bourgogne, 2005. URL: https://tel.archives-ouvertes.fr/tel-00011124.

[204] Donald Lupo. “Molecular Nonlinear Optics: Materials, Physics, and Devices.” In: *Advanced Materials* 7.2 (1995), pp. 248–249. DOI: https://doi.org/10.1002/adma.19950070232. eprint: https://onlinelibrary.wiley.com/doi/pdf/10.1002/adma.19950070232. URL: https://onlinelibrary.wiley.com/doi/abs/10.1002/adma.19950070232.

Appendix A

Menlosystem C-combs

Outline of the current chapter

The two commercial frequency combs I used at ONERA are Menlosystems C-combs. Their central emission wavelength is 1.5 µm. The set-up is divided into two parts: the optical part, with the two fiber mode-locked lasers as described in section 1.1.4 of Chapter 1, mounted on an optical table; and the electronic part, with the modules to monitor the lasers. That gives access to the tunability and stabilization of the two repetition rates. It is also possible to adjust the lasers offset frequencies by the current of the diodes that pump the two MLLs.

A.1 General description

A.1.1 Optical system

General description

The Figure A.1 presents a photograph of the optical part of the setup. Each comb source has two free-space optical outputs: a frequency comb output G, and an output H resulting from the spectral broadening of signal G, called "supercontinuum". The different electronic modules allow controlling the optical parameters, with typical values presented in Table A.1.

Focus on the super-continuum

The signal resulting from the mode locking is spectrally broadened, for example, in a microstructured fiber [202]. The process involves nonlinear effects such as phase self-modulation that

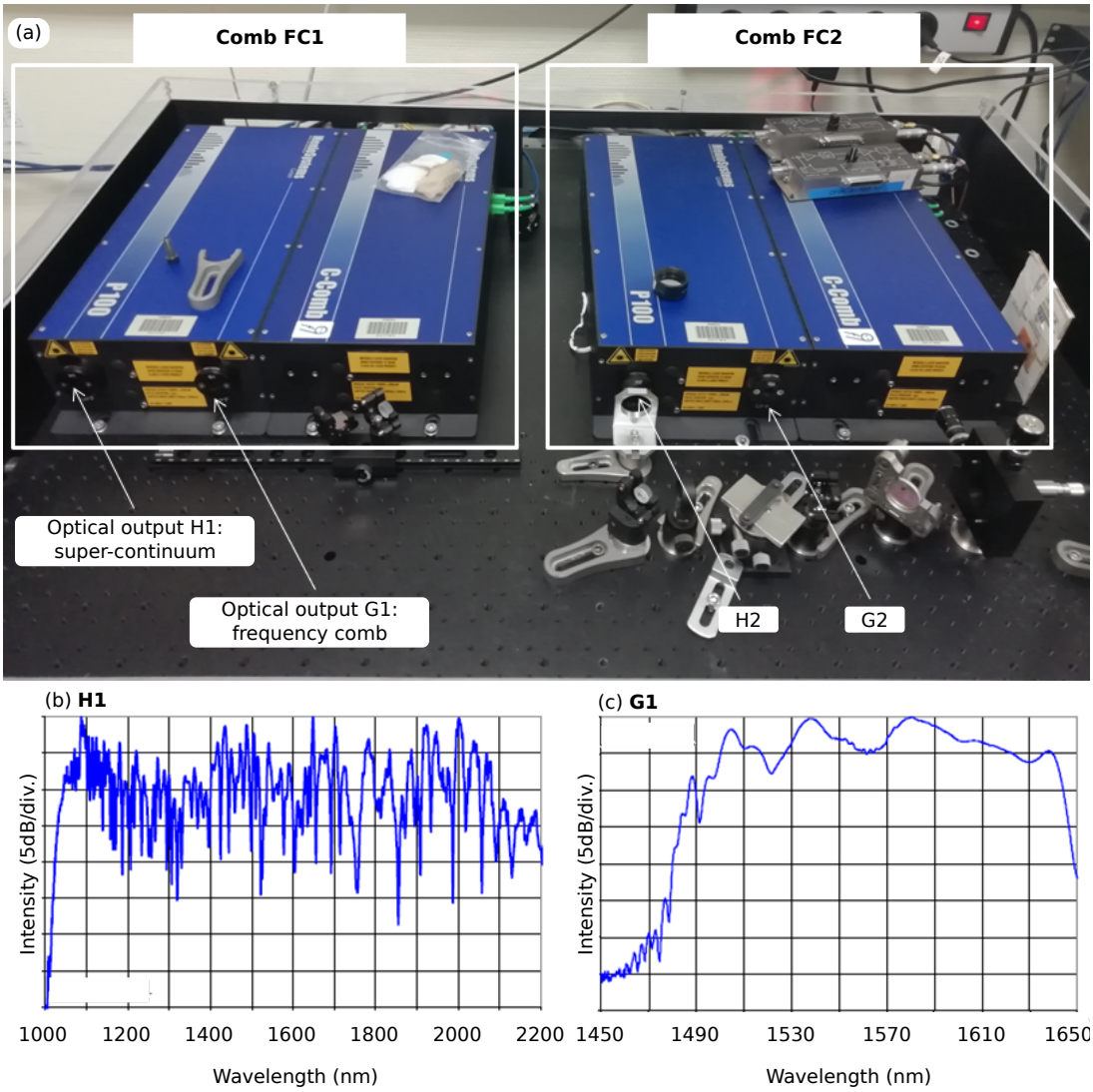

Figure A.1: Optical part of the setup.(a) Photograph of the optical table consisting of two commercial comb sources from MenloSystems, each with two free-space optical outputs: a frequency comb output G and an output H resulting from the spectral broadening of signal G, called "supercontinuum". (b) Optical spectra of the supercontinuum, H1, and of (c) the frequency comb, G1. Outputs for laser 1, from Menlosystems Technical Report, 2014.

compensates for chromatic dispersion; this corresponds to a "anomalous" dispersion regime [203]. The amplification leads to pulse compression, with the pulse shape approaching that of a soliton. Once a certain threshold power is reached, the situation becomes unstable, and the soliton undergoes a fission into higher-order solitons (waves whose shape evolves over time but in a periodic manner). This fission results in the appearance of numerous peaks that enrich the spectrum of the initial electromagnetic wave, known as a supercontinuum.

Parameter	Value
Carrier wavelength	1550 nm
Spectral width	$\sim$ 100 nm
Pulse duration	100 fs
Repetition frequency	100 MHz
Number of modes	$\sim 10^5$
Average power	qq 100 mW

Table A.1: Parameters and typical values of the two C-comb model sources from Menlosystems.

A.1.2 Electronic Part

Figure A.2 presents a photograph of the electronic part of the setup. The operation of the different modules will be detailed in Section IV.1 dedicated to the stabilization of δf_{rep}.

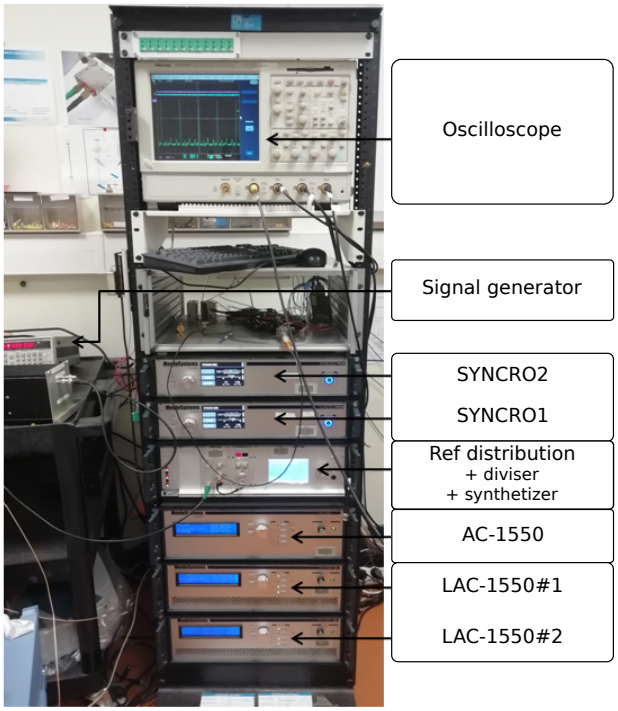

Figure A.2: Photograph of the electronic part of the setup. The role of the different parts is explained in the body of the text.

Control

The two LAC-1550 (MenloSystems) are the control units of the lasers, which allow adjusting the cavity lengths by acting on piezoelectric elements. The AC-1550 (MenloSystems) is a controller for the amplification of G1 and G2, which are the comb outputs of the two lasers. The two SYNCRO (MenloSystems), which work with a frequency generator serving as a reference, a divider, and a frequency synthesizer, allow locking the phase of the modes in each laser.

Monitoring

The oscilloscope allows monitoring this mode locking by displaying an error signal indicating the difference between the reference and the f_{rep}. It also displays the RF comb created by superimposing the two optical combs.

A.2 Locking of the repetition rates

Both repetition rates are locked on one common external reference. This is ensured by the commercial module SYNCRO, whose operation is described in the following.

A.2.1 Comb FC1 (variable repetition frequency)

Starting from the 10 MHz reference, SYNCRO1 generates a 980 MHz signal. The repetition frequency of Comb1 is multiplied by 10 to make the signal 10 times more sensitive to noise, thereby improving stabilization. This multiplied signal, known as the 10th harmonic, is mixed with the 980 MHz signal to generate an intermediate signal at 20 MHz (referred to as "down-mixed repetition rate"). In parallel, a frequency generator provides a reference signal at approximately 20 MHz. The phase difference between this signal and the down-mixed repetition rate generates an error signal, which is then minimized by the PID (proportional, derivative, integral) electronics. A piezoelectric element varies the length of the cavity, directly changing the repetition frequency of the laser. Changing the output of the frequency generator enables to change the repetition frequency of comb 1.

A.2.2 Comb FC2 (fixed repetition frequency)

From the 10 MHz reference, SYNCRO2 generates a signal at 1000 MHz. This reference signal is directly mixed with the 10th harmonic of the repetition frequency. The locking electronics adjust the length of the laser cavity to minimize the error signal. In this case, there is no separate frequency generator, and the repetition frequency of Comb 2 can only be stabilized at the value of 100 MHz.

Appendix B

Electro-optic modulation

Outline of the current chapter

The electro-optic effect is a non-linear phenomenon resulting from the interaction between a static electric field and an electromagnetic (EM) wave. The electric field modifies the refractive index of a material, and this is used to modulate the propagating EM wave.

B.1 Generalities on the electro-optic effet

In anisotropic media, the relationship between the electric field $\vec{E}$ and the electric displacement field $\vec{D}$ is no longer collinear but depends on the orientation of $\vec{E}$. That property means that the refractive index depends on the polarisation of the wave. In these birefringent media, there is at least one preferred direction for which the index is independent of the polarization. Such a direction is called *optical axis* of the medium. When the birefringent crystal is subjected to an electric field, the refractive index along its optical axes is modified. If the change in index is proportional to the amplitude of the electric field, it is a second-order non-linear effect known as *the Pockels effect*. This effect can only occur in non-centrosymmetric materials (and therefore not in optical fibers). It is the most commonly used effect for manufacturing electro-optic modulators.

B.2 Phase modulation

In a non-centrosymmetric anisotropic medium of length L, which is subjected to an electric field of amplitude V, the Pockels effect is responsible for a change Δn in the refractive indices of the

optical axes of the medium proportionally to V. Therefore, for a polarization along one of the optical axes, the induced phase $\Delta\varphi$ on a wave of carrier wavelength λ propagating orthogonally to that axis is [204]:

$$\Delta\varphi = \frac{2\pi L}{\lambda}\Delta n = K^{\text{phase}} \times V \tag{B.1}$$

The proportionality of the effect is represented by the *modulation depth* K, which is the modulator constant and depends on its parameters. This equation can be re-written as:

$$\Delta\varphi = \frac{\pi V}{V_\pi^{\text{phase}}} \tag{B.2}$$

where $V_\pi^{\text{phase}} = \frac{\pi}{K^{\text{phase}}}$ is the required tension for the modulator to induce a phase of π. This direct use of the Pockels effect in an anisotropic crystal for the phase modulation of an EM wave is the main building block for other modulators' architectures.

B.3 Polarisation modulation

In the case of a phase modulator, the wave is polarized along one of the principal axes of the crystal, so its polarization state is maintained during propagation, and the quantity $\Delta\varphi$ is the accumulated phase difference between the output and the input of the crystal. In the case of a polarization modulator, the wave is polarized at 45° from the principal axes, and the quantity $\Delta\varphi$ represents the phase shift between the two polarization components. Its expression remains similar to Eq. (1.11):

$$\Delta\varphi = K^{\text{pola}} \times V = \frac{\pi V}{V_\pi^{\text{pola}}} \tag{B.3}$$

but this time it leads to a rotation of the polarization. V_π^{pola} is the voltage at which the polarisation has turned of $\frac{\pi}{2}$, meaning that the modulator is equivalent to a half-wave plate. An important point to note is that $V_\pi^{\text{pola}} = V_\pi^{\text{phase}}/2$, which means that the applied voltage does not need to be as high [204].

B.4 Intensity modulation

Polarization modulation can be combined with a pair of crossed polarizers to modulate an electromagnetic wave in intensity. Indeed, a first polarizer makes the linear polarization to be at 45° to the crystal axes, as described earlier. The two polarization components acquire a phase shift between them of $\Delta\varphi = \frac{\pi V}{V_\pi^{\text{pola}}}$. A quarter-wave plate is then placed to achieve a total phase shift of $\Delta\varphi^{\text{int}}$:

$$\Delta\varphi^{\text{int}} = \Delta\varphi + \frac{\pi}{2} = \frac{\pi V}{2V_\pi^{\text{int}}} + \frac{\pi}{2} \tag{B.4}$$

with $V_\pi^{\text{int}} = V_\pi^{\text{pola}}/2$. Therefore, the purpose of the half-wave plate is to lower the required voltage. After the final analyzer, the global transmission T of the set up is:

$$T = \frac{\left|\mathbf{E}_{\text{output}}\right|^2}{\left|\mathbf{E}_{\text{input}}\right|^2} = \sin^2\left(\frac{1}{2}\Delta\varphi^{\text{int}}\right) = \sin^2\left(\frac{\pi V}{4V_\pi^{\text{int}}} + \frac{\pi}{4}\right) \tag{B.5}$$

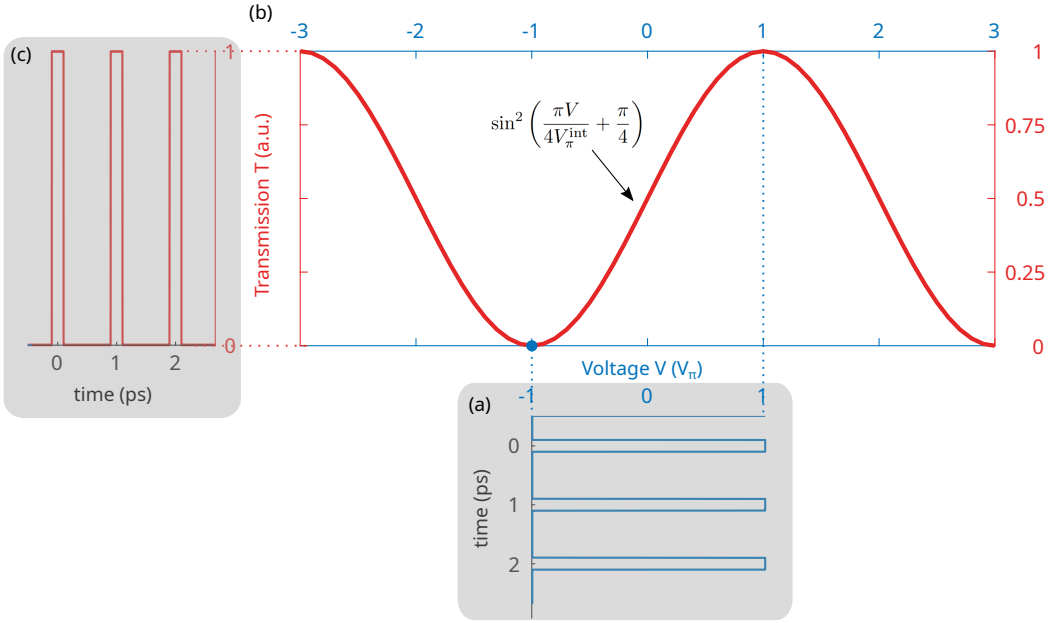

Figure B.1: Comb generation by intensity modulation. (a) Squared RF pulses driving the intensity modulator as a function of time. (b) Transmission of the intensity modulator as a function of the applied voltage. (c) Transmission of the intensity modulator as a function of time.

This transfer function is plotted in Figure B.1 (b). The transmission of this type of set-ups is completely monitorable through RF control of the voltage V.

B.5 Electro-optic combs from intensity modulation

The previous paragraphs explored the various phenomena that modify an EM wave through an electric field. Thus, proper control of the voltage feeding a modulator can generate a frequency comb. Unlike phase modulators (PMs), intensity modulators (IMs) can directly generate pulses at the Fourier limit, which is a considerable advantage [25]. Additionally, it is possible to use a single IM to generate a frequency comb, simplifying the experimental setup. This is the choice that has been made for this thesis, which is why comb generation from intensity modulation will be detailed. Let's take the example of square pulses feeding the intensity modulator at the operating point 0 (Figure B.1 (a)). The resulting transmission from this RF control is a train of square pulses, with the same duration and repetition frequency. Because the amplitude of the RF pulses is V_π, the maximum transmission is achieved. From a continuous EM wave, electro-optic modulation enables the generation of a train of optical pulses by RF driving.

Generation of triple frequency combs in multi-core fibres for multidimensional spectroscopy

Abstract

This thesis work explores the development, characterization, and practical application of a novel, fully fibered, and freely-tunable tri-frequency-comb laser source for advanced multidimensional spectroscopy. Tricomb spectroscopy unveils a new dimension to standard linear and non-linear spectroscopic analysis, offering the possibility to reveal the almost real-time evolution of complex systems with unprecedented accuracy. Current tri-comb configurations are based on the use of mode-locked lasers, which impose constraints on the comb parameters, and require complex electronic synchronization, thus limiting potential applications. In this thesis, we present the experimental demonstration of the spatial multiplexing in a multi-core non-linear fiber of three electro-optic combs from a common laser source. This architecture aims to ensure intrinsic mutual coherence between the three combs. The manuscript provides a comprehensive study of the development and characterization of the three combs. We validated their pairwise coherence through dual-comb experiments. We exploited the tri-comb coherence to experimentally investigate intra-envelope four-wave mixing phenomenon in optical fibers. Using the third comb as a multi-line local oscillator enabled us to extract and analyze the intermingled components resulting from the non-linear interaction between the two first combs. We then revealed the high mutual coherence between the three broadened combs by applying this approach through the demonstration of a 2-D FWM spectroscopy experiment.

Keywords: non-linear fiber optics, multi-core fiber, spatial multiplexing, frequency comb, multi-dimensional coherent spectroscopy, four wave mixing, electro-optic modulation, self phase modulation

---

Génération de triple peignes de fréquences dans les fibres multi-coeurs pour la spectroscopie multidimensionnelle

Résumé

Ces travaux de thèse explorent le développement, la caractérisation et l'application pratique d'une nouvelle source de tri-peigne de fréquences entièrement fibrée, et accordable, pour la spectroscopie multidimensionnelle. La spectroscopie à trois peignes apporte une nouvelle dimension à l'analyse spectroscopique linéaire et non linéaire classique, offrant la possibilité de mesurer l'évolution presque en temps réel de systèmes complexes avec une précision inégalée. Les configurations actuelles de tri-peignes sont fondées sur l'utilisation de lasers à verrouillage de modes, ce qui impose des contraintes sur les paramètres du système et nécessite une synchronisation électronique complexe, limitant ainsi les applications potentielles. Dans cette thèse, nous présentons la démonstration expérimentale du multiplexage spatial de trois peignes électro-optiques provenant d'une source laser commune, dans une fibre non linéaire à plusieurs cœurs. Ce choix d'architecture vise à assurer une cohérence mutuelle intrinsèque entre les trois peignes. Ce manuscrit fournit une étude du développement et de la caractérisation des trois peignes. Nous avons validé leur cohérence par paire grâce à des expériences à double peigne. Nous avons exploité la cohérence à trois peignes pour étudier expérimentalement le phénomène de mélange à quatre ondes intra-enveloppe dans les fibres optiques. L'utilisation du troisième peigne comme oscillateur local multi-lignes nous a permis d'extraire et d'analyser les composantes entremêlées résultant de l'interaction non linéaire entre les deux premiers peignes. Nous avons ensuite révélé la haute cohérence mutuelle entre les trois peignes élargis en appliquant cette approche à la démonstration d'une expérience de spectroscopie tri-peigne en 2D.

Mots clés : optique non linéaire fibrée, fibre multi-coeur, multiplexage spatial, peigne de fréquences, spectroscopie cohérente multidimensionnelle, mélange à quatre ondes, modulation électro-optique, auto-modulation de phase

---

Laboratoire de Physique des Lasers, Atomes et Molécules (PhLAM) – Campus Cité Scientifique – 2 Avenue Jean Perrin – 59655 Villeneuve d'Asq Cedex – France
Institut de Recherche en Composants logiciels et matériels pour l'Information et la Communication Avancée (IRCICA) – Parc Scientifique de la Haute Borne – 50 avenue Halley – 59658 Villeneuve d'Asq Cedex – France
Office national d'études et de recherches aérospatiales (ONERA) – 6 Chemin de la Vauve aux Granges – 91120 Palaiseau – France